Investigation of Ion Trapping in High-Power Electron Beams for Electron Coolers

Dissertation
submitted for the award of the title
"Doctor of Natural Sciences"
to the Faculty of Physics, Mathematics, and Computer Science
of the Johannes Gutenberg-University
in Mainz

Thomas Beiser

born in Mainz

Mainz, 06 June 2023

Date of doctoral viva: 16.11.2023

Contents

Abstract

Electron coolers utilize high-current electron beams to counteract emittance blow up of hadron beams circling in storage rings with equal velocity, by enveloping the hadrons and transferring their momentum to the electrons in a dedicated cooling section of the accelerator. To achieve effective cooling, electron beams with currents in the Ampere regime are required. Diagnostics of such high-current electron beams is crucial for effective operation. In this thesis, the possibility of using beam induced fluorescence (BIF) of residual gas as a means of beam diagnostics was investigated. At the electron cooler test bench located at Helmholtz-Institute Mainz the BIF signal, which is caused by ionized residual gas particles trapped in the electromagnetic potential of the electron beam, indicated the center of charge and the boundary of said electron beam. A simple model, describing the intensity distribution of the BIF, could be established. Brief beam interruptions were used to significantly suppress the BIF, while preserving a large duty cycle. It also became evident, that the residual gas in the ultra-high vacuum vessel of the test bench is infused with barium, evaporating from the dispenser cathode, which in turn influences the BIF. This type of cathode is commonly used in most applications that rely on high DC beam currents. In addition, the electron source was improved to be more robust against Penning discharges for certain electromagnetic field configurations, allowing for an electron beam current of $1\,A$.

Zusammenfassung

Elektronenkühler verwenden Hochstrom-Elektronenstrahlen, um einer Emittanzvergrößerung von Hadronenstrahlen, welche mit entsprechend gleicher Geschwindigkeit in Speicherringen zirkulieren, entgegenzuwirken, indem sie die Hadronen einhüllen und ihren Impuls in der Kühlsektion des Beschleunigers auf die Elektronen übertragen. Um effektive Kühlung zu erreichen wird ein Elektronenstrom in der Größenordnung von Ampere benötigt. Die Diagnose solcher Hochstrom-Elektronenstrahlen ist entscheidend für einen effektiven Kühlerbetrieb. In dieser Arbeit wurde die Möglichkeit untersucht, die strahlinduzierte Fluoreszenz (beam induced fluorescence oder BIF) des Restgases zur Strahldiagnose zu nutzen. Am Elektronenkühler-Teststand (am Helmholtz-Institut Mainz) veranschaulichte das BIF-Signal, das durch ionisierte Restgasteilchen, die im elektromagnetischen Potential des Elektronenstrahls gefangen sind, erzeugt wird, das Zentrum der Ladung und den Rand des Elektronenstrahls. Ein einfaches Modell zur Beschreibung der Intensitätsverteilung der BIF konnte aufgezeigt werden. Kurze Strahlunterbrechungen wurden verwendet, um die BIF bei hohem duty cycle zu minimieren. Es wurde auch deutlich, dass das Restgas in der Ultrahochvakuumkammer des Teststandes mit Barium, welches aus der Dispenserkathode verdampft, angereichert ist und somit die BIF beeinflusst. Diese Art von Kathode wird in den meisten Anwendungen, die auf hohen Gleichströmen basieren, verwendet. Darüber hinaus wurde die Elektronenquelle optimiert, um gegenüber Penning-Entladungen bei bestimmten elektromagnetischen Feldkonfigurationen robuster zu sein, was einen Elektronenstrom von 1 A ermöglicht.

Abbreviations

General	
a.u.	Arbitrary Units
BIF	Beam Induced Fluorescence [64]
CAD	Computer Aided Design
CF	Conversion Factor
COSY	Cooler Synchrotron at Forschungszentrum (FZ) Jülich
CST	Computer Simulation Technology® - Studio Suite [61]
DC	Direct Current
EM	Electromagnetic
emCCD	Electron Multiplying Charge-Coupled Device
FWHM	Full Width at Half Maximum
FZ	Forschungszentrum (Research Center)
GSI	GSI Helmholtzzentrum für Schwerionenforschung in Darmstadt, Germany
HIM	Helmholtz-Institute Mainz, Germany
KPH	Institute for Nuclear Physics at Johannes Gutenberg-University in Mainz, Germany
NIST	National Institute of Standards and Technology, U.S.A.
PMT	Photomultiplier Tube
QE	Quantum Efficiency
sCMOS	Scientific Complementary Metal-Oxide-Semiconductor
TSL	The Svedberg Laboratory in Uppsala, Sweden
UHV	Ultra-High Vacuum
Physical Constants [40], [44]	
c	Speed of Light in Vacuum: $299\,792\,452\,\mathrm{m\,s^{-1}}$
h	Planck's Constant: $6{,}626\,070\,15 \cdot 10^{-34}\,\mathrm{J\,s}$
k_B	Boltzmann Constant: $1{,}380\,649 \cdot 10^{-23}\,\mathrm{J\,K^{-1}}$
e	Elementary Charge: $1{,}602\,176\,46 \cdot 10^{-19}\,\mathrm{A\,s}$
m_e	Rest Mass of the Electron: $0{,}510\,998\,90\,\mathrm{MeV\,c^{-2}}$

1. Introduction

Fast Particles - Why?

Particle accelerators have been instrumental in the advancement of scientific knowledge. They uncovered the existence of various elementary particles, such as quarks, neutrinos, and the Higgs boson, among others. By colliding particles at extremely high energies, accelerators enable an investigation of interactions between these subatomic entities and validate theoretical predictions. These are vital components for discovering and refining the Standard Model of particle physics, which governs our scientific understanding of the world. This fundamental research ultimately led to a lot of different applications in everyday life, such as cancer treatments, medical imaging, material science, semiconductor manufacturing and more, without ever planning for it. Particle accelerators have revolutionized our understanding of the universe and will most likely continue to do so.

Electron Cooling

Hadron accelerators are able to probe deep into the structure of matter using collider rings to reach high energies and are less prone to energy loss through synchrotron radiation compared to electron accelerators. Hadron beams stored in accelerator rings are influenced by space charge effects and interact with the residual gas in the beam pipe. In the presence of an internal target the scattering effects are even more prevalent. This leads to an increase in the beam's *emittance*, a measure for the deviation from the design (or ideal) orbit of the accelerator in phase space. The electromagnetic fields that guide and focus the hadron beam in the form of mostly electromagnets exert only conservative forces. According to Liouville's theorem these can not compress phase space. At this point electron accelerators come into play again. If a hadron beam is overlaid with an electron beam of equal velocity along a short section of the accelerator ring (cooling section), momentum transfer occurs from the hadrons to the electrons via elastic scattering. Beam temperature is defined as movement in relation to the rest frame of a hypothetical particle on the design (or reference) orbit and originates in the kinetic theory of gases. This temperature is low (or *it is cool*) compared to the hadron beam because of the electron beam's smaller momentum distribution, and it stays that way because it is constantly renewed. Over time, the electron-hadron interactions lead to a decrease and finally a stabilization of the beam emittance.

Beam Diagnostics

As the effectiveness of electron cooling is directly correlated with the number of electrons the hadrons can interact with, an electron current as high as possible is preferred. This direct current (DC) (meaning uninterrupted current in this case) in the Ampere range is provided by a thermionic cathode. To counteract space charge effects the electron beam travels in a solenoid field, which also envelops the cooling section of a hadron accelerator. Beam diagnostics are needed to properly control such an electron cooler beam. Invasive forms of position measurement tools like they are commonly used in accelerator environments, for example luminescent screens or wire scanners can not withstand such a beam. Beam position monitors measure mirror charges caused by the beam and extrapolate the beam's center of charge. Another idea would be to investigate if the interactions of the electron beam with the residual gas and the resulting emission of photons (called *beam induced fluorescence* or *BIF*) reveal useable information about the beam.

2. Theory of Beam Cooling

A charged particle beam in an accelerator is assigned an *emittance*, which describes the beam size, its energy spread and their corresponding evolution (in 6-dimensional phase space) in reference to the design orbit of the accelerator. The emittance increases over time through interactions of the particle beam with internal target experiments and the residual gas in the accelerator's beam pipe *(scattering)*. According to Liouville's theorem phase space volume cannot be compressed by conservative forces, which means the emittance of a charged particle beam cannot be decreased by accelerator optics (e.g. quadrupoles). Beam cooling can overcome this obstacle.

The following summary of concepts is based on textbooks [32], [30] and review articles [54].

2.1. Phase Space

2.1.1. Liouville's Theorem

In a Cartesian coordinate system the motion of a particle is fully determined by the three spatial coordinates (x, y, z) and the corresponding momentum components (p_x, p_y, p_z). This information is represented by a point in six-dimensional phase space (x, p_x, y, p_y, z, p_z). A particle beam is described by an ensemble of these points in phase space. The particle beam is characterized by the density distribution of the points in phase space. When observed as a function of time t, the density distribution changes its shape, but occupies an equal volume at all times, as long as the acting forces are conservative. According to Liouville's theorem, the local particle density ρ is invariant, if the forces acting on the particle can be described by a Hamiltonian.

The Hamiltonian of a relativistic particle is

$$H = q\Phi + c[(\mathbf{P} - q\mathbf{A}^2 + m^2c^2]^{1/2} \tag{2.1}$$

with $\mathbf{P}$ the conjugate momentum of the spatial coordinate $\vec{x}$, the Coulomb potential Φ and the vector field $\mathbf{A}$ related to the magnetic field $\mathbf{B} = \nabla \times \mathbf{A}$ [43]. The conjugate momentum is

$$\mathbf{P} = \mathbf{p} + q\mathbf{A} \tag{2.2}$$

with the normal momentum $\mathbf{p}$. In a drift section of an accelerator $\mathbf{A} = 0$ and therefore $\mathbf{P} = \mathbf{p}$. The derived equations of motion *(Hamilton's equations)* are

$$\dot{P}_i = -\frac{\partial H}{\partial x_i}, \quad \dot{x}_i = \frac{\partial H}{\partial P_i}, \quad i = 1, 2, 3. \tag{2.3}$$

To prove Liouville's theorem one considers the continuity equation of the density function $\rho(x_1, P_1, x_2, P_2, x_3, P_3, t)$ in 6-dimensional phase space:

$$\sum_{i=1}^{3} \left[\frac{\partial}{\partial x_i}(\rho \dot{x}_i) + \frac{\partial}{\partial P_i}(\rho \dot{P}_i) \right] + \frac{\partial \rho}{\partial t} = 0. \tag{2.4}$$

Expansion of this term leads to

$$\sum_{i=1}^{3} \left[\rho \frac{\partial \dot{x}_i}{\partial x_i} + \dot{x}_i \frac{\partial \rho}{\partial x_i} + \rho \frac{\partial \dot{P}_i}{\partial P_i} + \dot{P}_i \frac{\partial \rho}{\partial P_i} \right] + \frac{\partial \rho}{\partial t} = 0 \tag{2.5}$$

and with (2.3) the first and third term add up to 0. Therefore,

$$\sum_{i=1}^{3} \left[\dot{x}_i \frac{\partial \rho}{\partial x_i} + \dot{P}_i \frac{\partial \rho}{\partial P_i} \right] + \frac{\partial \rho}{\partial t} = 0 \tag{2.6}$$

i.e.

$$\frac{\mathrm{d}\rho}{\mathrm{d}t} = 0 \tag{2.7}$$

This means that the local particle density along a trajectory in the 6-dimensional phase space is invariant.

2.1.2. Reference Orbit and Curvilinear Coordinates

In accelerator physics the reference orbit is the ideal path a particle can travel along in the accelerator and is a result of the accelerator lattice design. The reference orbit is situated in the magnetic center plane of the accelerator, where only radial forces act on a hypothetical particle traveling on that trajectory.

A curvilinear coordinate system (x, y, s) is now introduced, which moves with the reference orbit $\mathbf{r}_0(s)$ of the beam line, i.e. the distance traveled along the reference orbit s determines the position of the coordinate system. (Figure 2.1)

The x-axis and the tangential unit vector $\mathbf{u}_s$ define a plane congruent to the magnetic center plane of the accelerator. The trajectory of a particle relative to the reference orbit can be described by

$$\mathbf{r}(s) = \mathbf{r}_0(s) + x(s)\mathbf{u}_x(s) + y(s)\mathbf{u}_y(s) \tag{2.8}$$

with $\mathbf{u}_x$ and $\mathbf{u}_y$ being the unit vectors of the x- and y-axes. The corresponding differential of the (x, y, s) coordinate system is defined as

$$\mathrm{d}\mathbf{r} = \mathbf{u}_x dx + \mathbf{u}_y dy + \mathbf{u}_s(1 + hx)ds \tag{2.9}$$

with $h = 1/\rho_0$ the curvature of the reference orbit. For a drift section, where no magnetic deflection occurs, the curvilinear coordinate system transitions to a
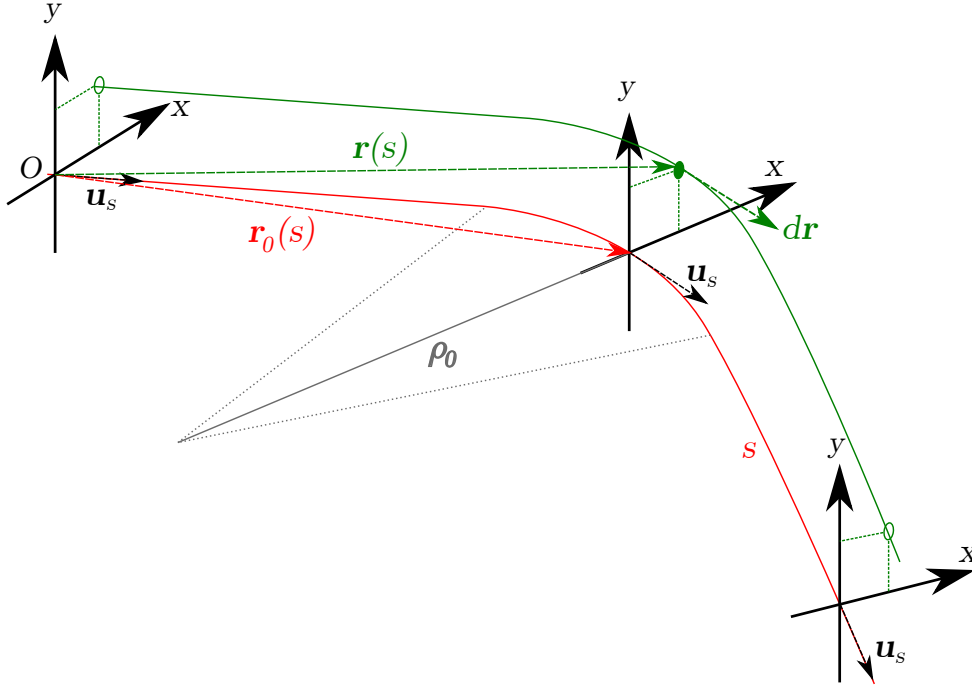
Figure 2.1.: Curvilinear coordinate system (x, y, s), coordinate origin O, the tangential unit vector $\mathbf{u}_s$, reference orbit $r_0(s)$ with the beam path s, the local radius of curvature ρ_0, a particle trajectory $\mathbf{r}(s)$ and its differential $d\mathbf{r}$.

Carthesian coordinate system continuously.

The description of a particle in 6-dimensional phase space can be adjusted from the standard notation (x, p_x, y, p_y, z, p_z) to the curvilinear coordinates. In the transverse direction the phase space can be characterized by the spatial deviation from the reference orbit x and y, and the deviation of the corresponding direction of movement (or angle) x' and y'.

$$x' = \frac{\mathrm{d}x}{\mathrm{d}s}, \quad y' = \frac{\mathrm{d}y}{\mathrm{d}s} \tag{2.10}$$

For the longitudinal direction phase space is described by the longitudinal spatial deviation l and the relative momentum deviation δ compared to the reference orbit.

$$l = -v_0(t - t_0), \quad \delta = \frac{p - p_0}{p_0} \tag{2.11}$$

The longitudinal coordinates l, δ are a snapshot of the particle trajectory and therefore refer to a stationary lab frame, i.e. there is no Lorentz boost to or from the moving curvilinear coordinate system. The adjusted description for one particle

in 6-dimensional phase space is

$$\mathbf{x}(s) = \begin{pmatrix} x \\ x' \\ y \\ y' \\ l \\ \delta \end{pmatrix} = \begin{pmatrix} \text{radial spatial deviation} \\ \text{radial directional deviation} \\ \text{axial spatial deviation} \\ \text{axial directional deviation} \\ \text{longitudinal spatial deviation} \\ \text{relative momentum deviation} \end{pmatrix} \qquad (2.12)$$

Those six values are small compared to a typical radius of curvature, so the following units are generally used:

$$x, y, l \;\; [mm]$$
$$x', y' \;\; [mrad]$$
$$\delta \;\; [^0/_{00}]$$

2.1.3. Particle Beam and the Emittance Ellipse

While $\mathbf{x}(s)$ describes one particle, the whole particle beam can be represented by the density distribution of many superimposed single particle trajectories $\rho(\mathbf{x}) = \rho(x, x', y, y', l, \delta)$ as a function of s. We first look at $\rho(x, x')$ the projection of the density distribution on the (x, x') plane. These density distributions can generally be outlined by an ellipse, usually called phase space ellipse.

The radial phase space ellipse can be represented by a symmetric (2×2)-matrix σ_x with a positive determinant.

$$\sigma_x = \begin{pmatrix} \sigma_{11} & \sigma_{12} \\ \sigma_{12} & \sigma_{22} \end{pmatrix} \qquad (2.13)$$

The equation for the phase space ellipse is

$$\mathbf{X}^T \; \sigma_x^{-1} \; \mathbf{X} = 1 \qquad (2.14)$$

with $\mathbf{X}$ the vector from the coordinate origin to the border of the ellipse, its transpose $\mathbf{X}^T$

$$\mathbf{X} = (x, x'), \;\; \mathbf{X}^T = \begin{pmatrix} x \\ x' \end{pmatrix} \qquad (2.15)$$

and the inverse matrix σ_x^{-1}

$$\sigma_x^{-1} = \frac{1}{\det(\sigma_x)} \begin{pmatrix} \sigma_{22} & -\sigma_{12} \\ -\sigma_{12} & \sigma_{11} \end{pmatrix} \qquad (2.16)$$

The solution of equation 2.14 gives us the squared emittance ε_x^2

$$\varepsilon_x^2 = \det(\sigma_x) = \sigma_{22} x^2 - 2\sigma_{12} x x' + \sigma_{11} x'^2 \qquad (2.17)$$

Therefore, the emittance can be written as

$$\varepsilon_x = \sqrt{\det(\sigma_x)} = \sqrt{\sigma_{11}\sigma_{12} - \sigma_{12}^2} \qquad (2.18)$$

with $[mm \cdot mrad]$ as its unit of measurement. The area of the phase space ellipse is

$$E_x = \pi\varepsilon_x \qquad (2.19)$$

and sometimes also referred to as emittance. The smaller its size, the better the quality of the beam, generally.
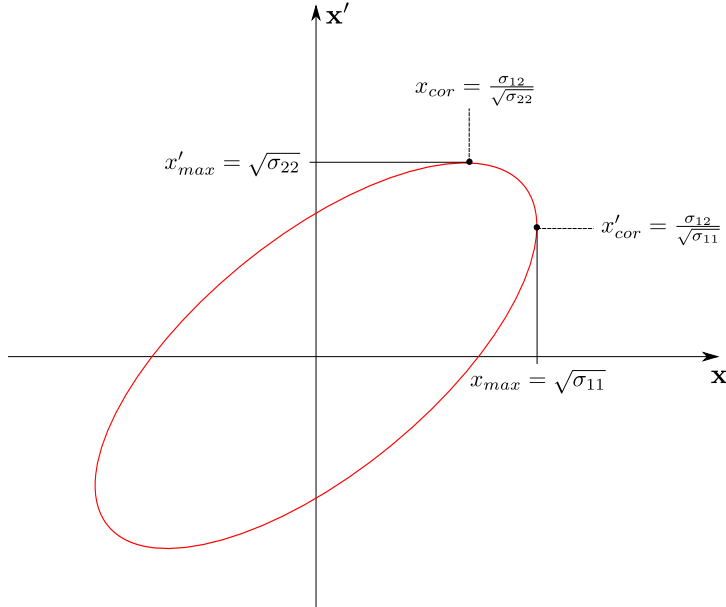

Figure 2.2.: Phase space ellipse in the (x, x') plane with correlation to σ_x matrix elements.

The geometric meaning of the matrix elements is indicated in Figure 2.2. The maximum values in x and x' directions are

$$x_{max} = \sqrt{\sigma_{11}}, \quad x'_{max} = \sqrt{\sigma_{22}} \qquad (2.20)$$

The correlation between spatial and directional deviation of the beam is given by σ_{12}.

The particle beam can be convergent, at its minimum spatial extension (*beam waist*) or divergent along its trajectory in the accelerator. The correlation with the emittance ellipse is depicted in Figure 2.3. At the *beam waist* of the particle beam in a drift section (where no external forces act on the beam), the ellipse is upright and the correlation between spatial and directional deviations is zero ($\sigma_{12} = 0$).
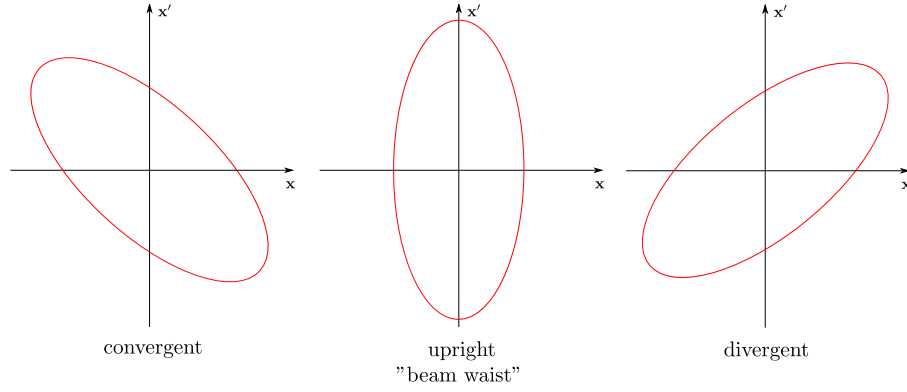
17

Figure 2.3.: Evolution of the emittance ellipse in the (x, x') plane during beam transport.

2.1.4. The Density Distribution in Phase Space

The assumption of a homogeneous density distribution might be too inaccurate in most cases, a two dimensional normal (or Gauss) distribution, however, is a much more realistic model for a beam in a particle accelerator. The normalized two dimensional normal distribution reads

$$\rho(\mathbf{x}) = \frac{1}{2\pi\varepsilon_x} \exp\left(-\frac{1}{2}\mathbf{x^T}\sigma_x^{-1}\mathbf{x}\right) \tag{2.21}$$

and is depicted in Figure 2.4. The phase space ellipse

$$\mathbf{X}^T \ \sigma_x^{-1} \ \mathbf{X} = 1 \tag{2.22}$$

marks the contour line (parallel to the (x, x') plane), where the density is decreased by a factor of $(\exp -1/2)$ from its maximum. This is one standard deviation $(\sigma^{SD})^*$ of the two dimensional normal distribution and incorporates 39.3% of the density. It represents the $1\sigma^{SD}$ emittance

$$\varepsilon_x^{1\sigma^{SD}} = \varepsilon_x = \sqrt{\sigma_{11}\sigma_{22} - \sigma_{12}^2} \tag{2.23}$$

The phase space ellipse

$$\mathbf{X}^T \ \sigma_x^{-1} \ \mathbf{X} = 4 \tag{2.24}$$

marks the contour line (parallel to the (x,x') plane), where the density is decreased by a factor of $(\exp -4/2)$ from its maximum. This is the $2\sigma^{SD}$ emittance and it incorporates 86.5% of the density.

$$\varepsilon_x^{2\sigma^{SD}} = 4\varepsilon_x^{1\sigma^{SD}} \tag{2.25}$$

---

*The letter σ is used twice in this introduction and distinguished by the superscript SD for the standard deviation. σ^{SD} has no connection to σ_x
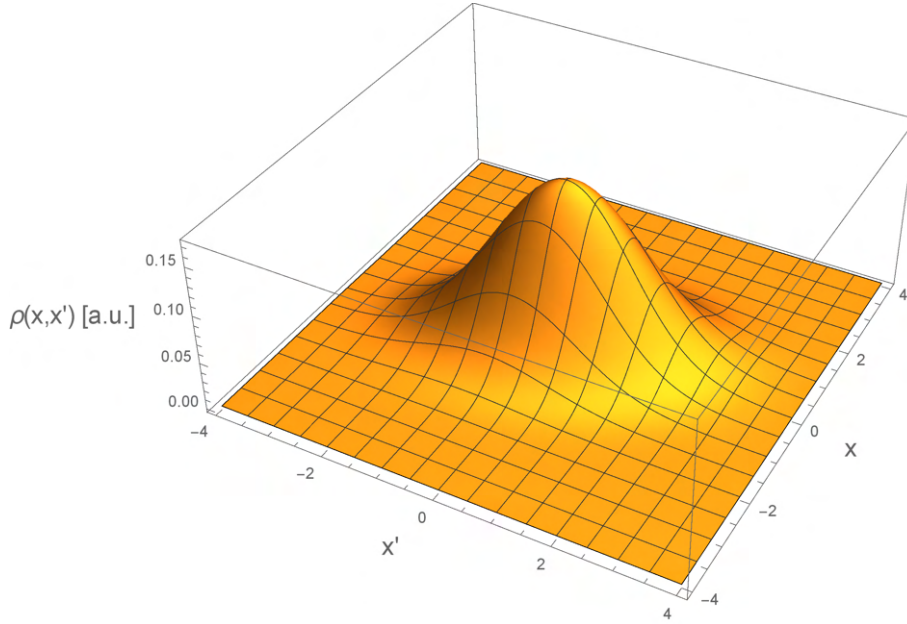
Figure 2.4.: Two dimensional density distribution in the (x, x') plane [9].

To cover 98.9% of the density one has to use the $3\sigma^{SD}$ emittance.

$$\varepsilon_x^{3\sigma^{SD}} = 9\varepsilon_x^{1\sigma^{SD}} \tag{2.26}$$

The specification above is necessary for comparisons between different accelerators or particle beams. For electron accelerators the $1\sigma^{SD}$ emittance is mostly stated, for proton accelerators the $2\sigma^{SD}$ emittance.

2.1.5. Circular Accelerators and the Machine Ellipse

The *equilibrium orbit* of a circular particle accelerator is defined by its magnetic field distribution (i.e. arrangement of magnets), corresponds to the reference orbit from chapter 2.1.2 and utilizes the same (x, y, s) coordinate system. The equilibrium orbit is closed , i.e. the orbit starts and ends at the same point and is periodic. The equations of motion along the equilibrium orbit are the *Hill differential equations*, here exemplified for the y direction

$$\frac{\mathrm{d}^2 y}{\mathrm{d}s^2} + K(s)y = 0, \quad K(s) = K(s + C) \tag{2.27}$$

with the circumference of the equilibrium orbit C. It differs from the equation of a harmonic oscillator by a periodic function $K(s)$, making it a *quasi-harmonic oscillator*. For particles with spatial and directional deviations from the equilibrium orbit, these equations are solved by so called *Betatron oscillations*.

In accordance with Chapter 2.1.3 the solution of the Hill differential equations can also be described by an ellipse, the so called *machine ellipse* with an area of

$$E = \pi\varepsilon = \text{const.} \tag{2.28}$$

The machine ellipse equation is called *Courant-Snyder-Invariant* and reads, exemplified for the (y, y') plane

$$\gamma y^2 + 2\alpha y y' + \beta y'2 = \varepsilon \tag{2.29}$$

with the *Twiss parameters* α, β and γ, which are the *Betatron functions*[†] $\alpha(s)$, $\beta(s)$ and $\gamma(s)$ at a specific point.

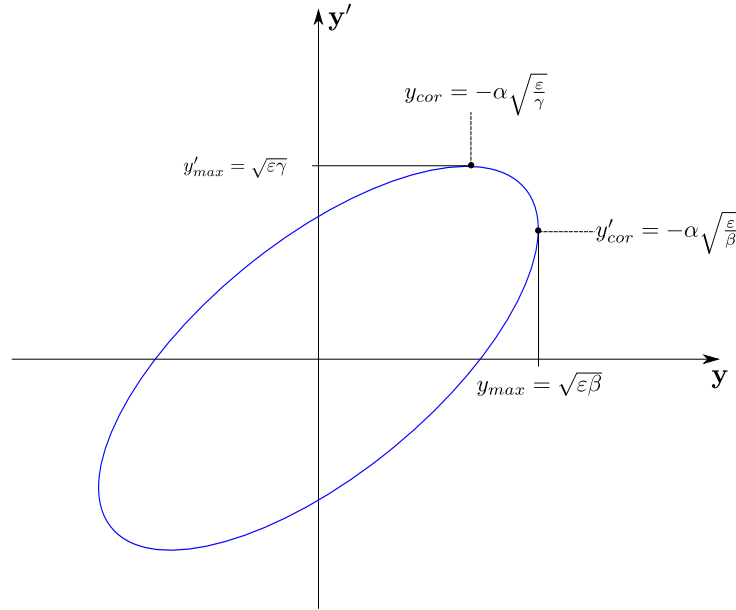A representation of this ellipse is depicted in Figure 2.5. A particle moves along

Figure 2.5.: Machine ellipse in the (y, y') plane with correlation to Twiss parameters.

the border of a continously changing phase space ellipse with a constant area. The maximum width of the beam (here for the y direction) is called *beam envelope* and is depicted in Figure 2.6

$$y_{max}(s) = \sqrt{\varepsilon\beta(s)} \tag{2.30}$$

2.1.6. Beam Ellipse and Machine Ellipse

The machine ellipse can differ significantly from the beam ellipse, e.g shortly after beam injection. In that case the phase space ellipse of the beam slowly adapts

---

[†]*Betatron functions* are often called *optical functions* or *lattice functions*.
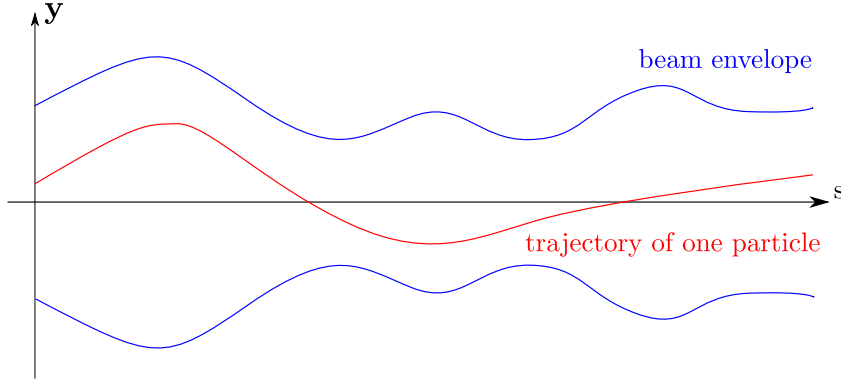
Figure 2.6.: Beam envelope in the y plane and a trajectory of one random particle.

to the machine ellipse (through a process called filamentation) at the expense of growing beam emittance (i.e. lower beam quality). Therefore, beam and machine ellipses should be matched as accurately as possible at the point of injection into the circular accelerator.

When they are matched, there is the following correlation between the σ matrix from Chapter 2.1.3 and the Twiss parameters:

$$\sigma_x = \begin{pmatrix} \sigma_{11} & \sigma_{12} \\ \sigma_{12} & \sigma_{22} \end{pmatrix} = \varepsilon_x \begin{pmatrix} \beta_x & -\alpha_x \\ -\alpha_x & \gamma_x \end{pmatrix} \tag{2.31}$$

2.2. Beam Emittance

Considering σ_x^{SD}, $\sigma_{x'}^{SD}$, σ_y^{SD}, $\sigma_{y'}^{SD}$, σ_l^{SD} and σ_δ^{SD} as the standard deviations of the one dimensional density distributions for the variables of the six dimensional phase space vector introduced with Equation (2.12) and the special case of upright phase space ellipses for the (x, x'), (y, y') and (l, δ) planes in Chapter 2.1.3, the emittances can be characterized (based on $\varepsilon_x = \sqrt{\sigma_{11}\sigma_{22}} = x_{max}x'_{max}$) as

$$\varepsilon_x = \sigma_x^{SD}\sigma_{x'}^{SD}$$
$$\varepsilon_y = \sigma_y^{SD}\sigma_{y'}^{SD} \tag{2.32}$$
$$\varepsilon_l = \sigma_l^{SD}\sigma_\delta^{SD}$$

This assumption is viable, because there are always beam waists for the transversal planes of a circular accelerator, i.e. upright ellipses and therefore a disappearing correlation between spatial and angular deviations ($\sigma_{12} = 0$). The longitudinal ellipse in the (l, δ) plane is generally upright. This property in combination with

Equations (2.30) and (2.32) allows the expressions:

$$\sigma_y^{SD} = \sqrt{\varepsilon_y \beta_y}$$
$$\sigma_{y'}^{SD} = \sqrt{\frac{\varepsilon_y}{\beta_y}}$$

(2.33)

exemplified for the (y, y') plane.

2.3. Beam Temperature

The concept of a beam temperature originates from the kinetic theory of gases. The mean squared deviation in the rest frame of the reference particle, i.e. the center-of-mass frame, defines the beam temperature analogous to the kinetic theory of gases.

$$\frac{kT_x}{2} = \overline{\frac{p_{x, \, cm}^2}{2m}} = \frac{p^2}{2m}\sigma_{x'}^2 = \frac{p^2}{2m}\frac{\varepsilon_x}{\beta_x}$$

$$\frac{kT_y}{2} = \overline{\frac{p_{y, \, cm}^2}{2m}} = \frac{p^2}{2m}\sigma_{y'}^2 = \frac{p^2}{2m}\frac{\varepsilon_y}{\beta_y}$$

(2.34)

$$\frac{kT_l}{2} = \overline{\frac{p_{l, \, cm}^2}{2m}} = \frac{p^2}{2m\gamma^2}\sigma_{\delta}^2 = \frac{p^2}{2m\gamma^2}\frac{\varepsilon_l}{\beta_l}$$

The subscript *cm* denotes the corresponding variables being in the center-of-mass frame. The factor $1/\gamma^2$ in the longitudinal temperature results from a Lorentz transformation from the rest frame to the lab frame.

The decrease of the emittance and therefore the beam temperature over time via beam cooling can be described by the exponential relation

$$\varepsilon_y(t) = \varepsilon_y(0) \exp\left(-\frac{t}{\tau}\right)$$

(2.35)

The rate of attenuation $1/\tau$ determines the velocity of the emittance decrease. The accompanying reduction in geometric extension and momentum uncertainty increases the beam quality.

2.4. Beam Heating

There are effects that counteract the beam cooling, i.e. the beam is heated. This heating can result from the coulomb interactions of the particles in the beam itself, scattering on the residual gas in the accelerator and as a specific example the

interactions with an internal target in a storage ring. The emittance (here for the y direction) in the storage ring increases according to

$$\varepsilon_y = \varepsilon_{y,0} + \frac{1}{2} N \beta_y \Theta^2_{rms} \tag{2.36}$$

with the number of turns N, the Betatron function at the target position β_y and the variance of small-angle scattering due to coulomb interactions inside the target

$$\Theta_{rms} \approx Z \frac{14.1 \text{MeV}}{pv} \sqrt{\frac{x}{x_{rad}}} \tag{2.37}$$

with the charge number of the particles in the beam Z, the momentum p, the velocity v, the target thickness x and the radiation length in the target material x_{rad} [31], [57].

2.5. Adiabatic Damping and Normalized Emittance

During the acceleration of a particle beam the process of *adiabatic damping* (or *pseudo damping*) contracts the emittance ellipse, but is not considered *beam cooling*. This effect does not contradict and can be explained by Liouville's theorem (Chapter 2.1.1). If the particle trajectories are decoupled in the (x, p_x), (y, p_y) and (z, p_z) planes in phase space, an upright phase ellipse (here in the (x, p_x) plane) obeys

$$\Delta x \Delta p_x = \text{const.} \tag{2.38}$$

In accordance with Chapter 2.1.3 and $x = \Delta x$, $x' = \sin(x') = \frac{\Delta p}{p}$ for small angles x' (as depicted in Figure 2.7) the emittance can be described as

$$\varepsilon_x = \Delta x \frac{\Delta p_x}{p} = \frac{\text{const.}}{p}. \tag{2.39}$$

In the presence of acceleration, comparisons of emittances can, therefore, only be made, if the dependence on the momentum p is taken into account. Generally $p/m = \beta\gamma$ is used to express the *normalized emittance*

$$\varepsilon_x^{\text{n}} = \varepsilon_x \beta\gamma \tag{2.40}$$

which is proportional to the phase space ellipse in the (x, p_x) plane.

2.6. Stochastic Cooling

According to Liouville's theorem the density of a particle beam in phase space is not impacted by electromagnetic fields, i.e conservative forces. This holds true for constant and time-dependent fields, but strictly speaking only for a continuous medium. The particle beam, however, is comprised of individual particles, so only certain small volumes in phase space are occupied, with the rest being empty. If
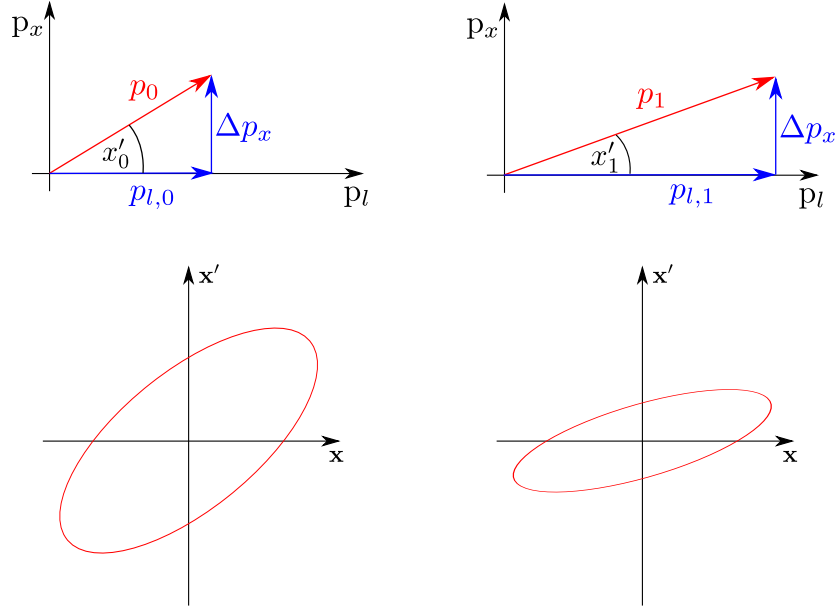
Figure 2.7.: Momentum and phase space ellipse of a particle in the (x, x') plane before (*left*) and after (*right*) acceleration; $x'_0 > x'_1$.

the coordinates of all particles would be known, one could exchange empty and occupied volumes with each other to decrease the beam emmitance with conservative forces, without violating Liouville's theorem. A statistical way to do this was discovered by van der Meer in 1968 [39].

For the transverse directions, respectively, a so called *pick-up* probe measures the spatial deviation from the reference orbit of a random sample of particles. A *kicker* magnet positioned a distance downstream (depending on a constant phase shift of the beams Betatron oscillations) is momentarily activated, as the measured sample passes it and therefore slightly moves (or kicks) the sample in the direction of the reference orbit (see Figure 2.8). The theoretical maximum of the *cooling* (or *damping*) *rate* $\frac{1}{\tau}$ is derived in [32] and results in

$$\frac{1}{\tau} \leq \frac{W}{N} \tag{2.41}$$

with the bandwidth of the cooling systems electronics W and the number of particles in the beam N. Longitudinally a circular pick-up can measure deviations, that can subsequently be reduced by small, appropriate accelerations of the related sample by a circular, so-called *RF-kicker*. One advantage of stochastic cooling is that the cooling rates $\frac{1}{\tau_x}$, $\frac{1}{\tau_y}$ and $\frac{1}{\tau_z}$ can be controlled individually [41].
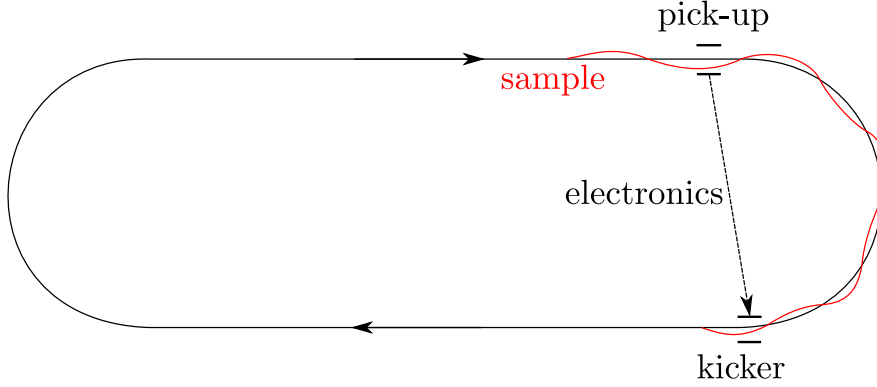
Figure 2.8.: Schematic of stochastic cooling.

2.7. Electron Cooling

The type of beam cooling relevant for this thesis is *electron cooling*. In electron cooling a high current electron beam ($I_{e-beam} \approx 1A$) is overlaid with a hadron or ion beam. The electron beam is *cold*, i.e. has a low beam temperature (see Chapter 2.3) and matches the speed of the hadrons on the accelerators reference orbit. Through coulomb interactions between both beams, the spatial and directional deviations of the hadron (or ion) beam and, therefore, the emittances ε_x, ε_y and ε_l are decreased simultaneously.

In practical applications electrons are created by a (most often thermionic) source inside a solenoid field (i.e. longitudinal magnetic field), accelerated (up to now, mainly electrostatically), redirected via a toroidal magnetic field to overlay with the beam intended to be cooled. In the *cooling section*, where the electron beam surrounds the hadron (or ion) beam, both are guided inside a solenoid field. The electrons propagate along spiral trajectories following the magnetic field lines. At the end of this section, the electrons are again redirected via a toroidal magnetic field, decelerated and dumped in the collector (see Figure 2.9). The direction of the hadron (or ion) beam does not change due to its several orders of magnitude higher momentum.

The fact that both beams are velocity matched, results in the following correlations between its momenta and energies

$$\frac{p_e}{p} = \frac{E_e}{E} = \frac{T_e}{T} = \frac{m_e}{m} \tag{2.42}$$

with $p = m\beta\gamma$, $E = m\gamma$ and $T = E_{kin} = m(\gamma - 1)$. That means, a 100 keV electron beam can cool a proton beam with a kinetic energy of 1837.6 MeV.

The main electron-ion interaction that results in cooling of the ions is Rutherford scattering in the rest frame of the electrons (see Figure 2.10). The differential cross-
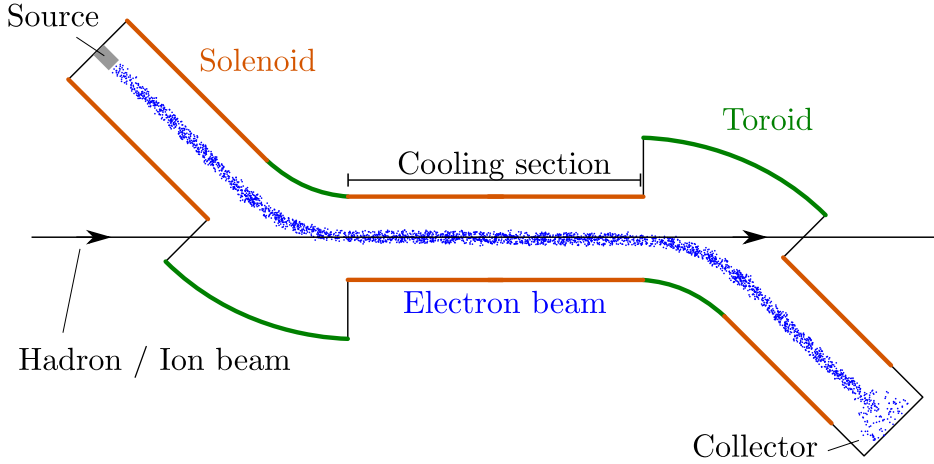
Figure 2.9.: Schematic of electron cooling.

section is

$$\frac{d\sigma}{d\Omega} = \frac{1}{(4\pi\varepsilon_0)^2} \frac{Z^2 e^4}{4E_{Ion}^2} \frac{1}{\sin^4(\frac{\theta}{2})} \tag{2.43}$$

with the ion charge Z, its energy in the rest frame of the electron E_{Ion} and the scattering angle θ. This differential cross-section shows that small-angle scatterings dominate. Therefore, a large number of interactions has to occur, for the momentum and energy transfer to be significant.

A simple derivation of the so called *cooling force*, a frictional force that describes the energy transfer from the ions to the electrons, considers a single electron-ion collision first.
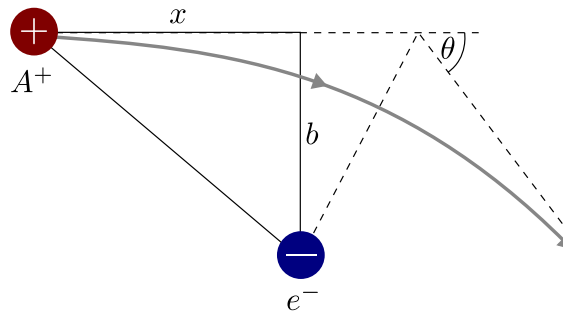
Figure 2.10.: Schematic of Rutherford scattering with an ion A^+, its initial direction x, an electron e^-, the scattering angle θ and the impact parameter b.

The impact parameter b in relation to the scattering angle θ is expressed by

$$b = \frac{Ze^2}{4\pi\varepsilon_0} \frac{1}{2E_{Ion}\tan(\frac{\theta}{2})}. \tag{2.44}$$

The transferred momentum from ion to electron can be determined by integrating the Coulomb force F_c over time. For $-\infty \to t \to \infty$ only the transverse component $F_{c\perp}$ contributes:

$$
\begin{aligned}
\Delta p_{Ion\to e^-} &= \int F_c \; \mathrm{d}t = \frac{1}{4\pi\varepsilon_0} \int \frac{Ze^2}{x^2+b^2} \; \mathrm{d}t \\[2mm]
&= \int_{-\infty}^{\infty} F_{c\perp} \; \mathrm{d}t = \frac{1}{4\pi\varepsilon_0} \int_{-\infty}^{\infty} F_c \frac{b}{\sqrt{x^2+b^2}} \; \mathrm{d}t \\[2mm]
&= \frac{1}{4\pi\varepsilon_0} \int_{-\infty}^{\infty} \frac{Ze^2 b}{v_{Ion}(x^2+b^2)^{3/2}} \; \mathrm{d}x \\[2mm]
&= \frac{2Ze^2}{4\pi\varepsilon_0 v_{Ion} b},
\end{aligned}
\tag{2.45}
$$

with the relative velocity of the ion in the rest frame of the electron $v_{Ion} = \mathrm{d}x/\mathrm{d}t$. The corresponding energy transfer is

$$\Delta E_{Ion\to e^-}(b) = \frac{\Delta p_{Ion\to e^-}^2}{2m_e} = \frac{2Z^2e^4}{(4\pi\varepsilon_0)^2 m_e b^2 v_{Ion}^2} \tag{2.46}$$

If one now considers a large number of scatterings, with the quantity of electrons n_e in the area perpendicular to $\mathbf{v}_{Ion}$ with radius b and the resulting area density $n_e b$, the *cooling force* F_{cool} can be described by integrating over all possible impact parameters b

$$F_{cool} = -\frac{\mathrm{d}E}{\mathrm{d}x} = 2\pi \int_0^{\infty} \Delta E_{Ion\to e^-}(b)\; n_e b \; \mathrm{d}b = \frac{4\pi Z^2 e^4 n_e}{(4\pi\varepsilon_0)^2 m_e v_{Ion}^2} \int_0^{\infty} \frac{\mathrm{d}b}{b} \tag{2.47}$$

In this case, where the multiple scattering occurs in a kind of electron gas, it is reasonable to consider certain cutoffs for the integration over the impact parameter.

$$\int_0^{\infty} \frac{\mathrm{d}b}{b} \;\to\; \int_{b_{min}}^{b_{max}} \frac{\mathrm{d}b}{b} = \ln\frac{b_{max}}{b_{min}} = L_c \tag{2.48}$$

with the Coulomb logarithm L_c, the minimal impact parameter b_{min} determined by the scattering angle of 180° (i.e. the maximum momentum transfer) and b_{max}, which is dependent on the mutual electromagnetic shielding of the electrons. A more detailed investigation of b_{max} would exceed the scope of this thesis, but the

2. Theory of Beam Cooling

Coulomb parameter scales with the ion velocity ($L_c \propto \ln v_{Ion}$) and for a standard case ($\beta_{e^-} \approx 0.5$, $v_{Ion} \approx 10^{-3}\beta_{e^-}c$) the Coulomb parameter can be approximated by $L_c \approx 10$ [54].

In application the electrons are guided by a solenoid field. The transverse momentum component $p_\perp$ forces them on a helical trajectory, rotating about the solenoid field lines with the cyclotron frequency

$$\omega_c = \frac{eB}{\gamma m_e} \tag{2.49}$$

and the gyration radius (often called Larmor radius)

$$r_c = \frac{p_\perp}{eB}. \tag{2.50}$$

This motion of the electrons influences the shielding properties of the electrons and, therefore, affects L_c. The electron speed $v_{e^-,rel}$ relative to the design orbit of the accelerator

$$v_{e^-,rel} = \sqrt{v_{e^-,\parallel}^2 + v_{e^-,\perp}^2} \tag{2.51}$$

describes the impact of additional electromagnetic interactions (e.g. misalignment of the solenoid field or space charge effects). The semi-empirical Parkhomchuk formula takes this into account and illustrates the cooling force in application as

$$F_{cool} \propto \frac{n_e Z^2 \, v_{Ion}}{(v_{Ion}^2 + v_{e^-,rel}^2)^{3/2}} \; \ln\left(\frac{b_{max} + b_{min} + r_c}{b_{min} + r_c}\right) \tag{2.52}$$

with the units $[eV/m]$ [51]. This formula highlights the necessity for a carefully aligned solenoid field ($v_{e^-,rel}$ small) with its field strength and the electron beam current as high as possible (r_c small, n_e large) to maximize F_{cool} and, therefore, optimize beam cooling. The *cooling* (or *damping*) *rate* for electron cooling is

$$\frac{1}{\tau} = \left|\frac{F_{cool}}{p_{Ion}}\right| \cdot \frac{\eta}{\gamma^2} \tag{2.53}$$

with the ratio of the cooling section length to the length of one design orbit $\eta = \frac{s_{cooling}}{s_{orbit}}$ and the Lorentz factor γ. The fraction η/γ^2 is needed to obtain the cooling time in the laboratory frame in order to directly compare $\frac{1}{\tau}$ with the cooling rate of stochastic cooling [16].

If both cooling methods are compared in terms of transverse emittance reduction, one finds, they might be used complementarily. It was shown that stochastic cooling works well for large emittance beams and electron cooling works well for small emittance beams (see Figure 2.11). A combination of both methods, where the halo and the core of the ion beam are affected respectively, can therefore be very effective (see Figure 2.12) [42].
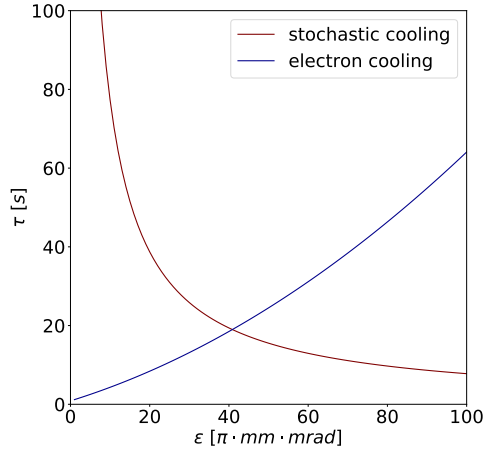
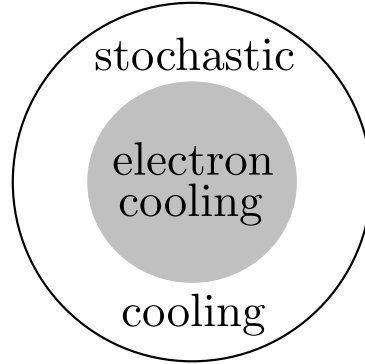**Figure 2.11.:** Cooling time of electron and stochastic cooling dependent on the emittance of the ion beam.

Figure 2.12.: Sketch of a beam cross-section depicting the most effective cooling method per region (*core* and *halo cooling*).

2.8. Other Beam Cooling Methods

Listed for the sake of completeness.

(*Synchrotron*) *radiation cooling* results from energy loss via synchrotron radiation of light particles (electrons / positrons), when they are forced onto curved paths by the accelerators dipoles. Only the longitudinal part of the momentum loss of the particles gets compensated by the accelerating components (e.g. accelerator cavities), therefore the radiation losses act as a friction towards transverse momentum [33].

Laser cooling works mainly in the longitudinal direction for suitable ions (with short lived excited states). Two lasers are positioned in line with the ion beam, opposite each other. Taking the Doppler effect and the directional absorption and isotropic emission of photons by the ions into account, the ions experience a directional momentum change in line with the lasers [16].

Ionization (or *muon*) *cooling* utilizes the longitudinal and transverse energy loss of particles in an absorber, followed by longitudinal acceleration as a damping mechanism for transverse momentum. This method does not work well for electrons or protons, because of Bremsstrahlung and non-elastic nuclear interactions respectively. It is used in muon accelerators / colliders, due to the fact that the cooling time matches the muon lifetime quite well ($\tau_\mu = 2.2\mu s$) [16]. These methods are outlined merely to contribute to a broader perspective, but will not be discussed further.

3. Experimental Setup

3.1. The Electron Cooler Test Bench

The apparatus used to generate electron beams in the Ampere regime for this thesis, from here on referred to as *electron cooler test bench*, is assembled from components provided by The Svedberg Laboratory (TSL) in Uppsala (electron source parts, solenoids), Forschungszentrum (FZ) Jülich (collector), GSI Helmholtzzentrum für Schwerionenforschung and Helmholtz-Institut Mainz (HIM), as well as equipment developed in-house (with support from the Institute for Nuclear Physics (KPH) at Johannes Gutenberg-University (JGU) Mainz). The test bench resembles an electron cooler, except for the usual bends of the beam pipe inside a toroid magnet and is depicted in Figure 3.1. The electron cooler test bench uses a thermionic barium dispenser cathode and an electrostatic potential to create and accelerate the electron beam. This beam travels in a longitudinal magnetic field, created by 4 solenoids, in a straight line, until it is decelerated and ultimately dumped into an oil-cooled collector. The deceleration is essential for the feasibility of energy recovery in this setup. A detailed description of the test bench can be found in [12]. Consequently it shall only be summarized in the following sections.

3.1.1. The Energy-Recovery-Setup

For the test bench a energy-recovering-setup is used, which means that the main high voltage (-18 kV) is applied by a relatively small high voltage (HV) power supply to the source and an insulated larger power supply, that is used to power the collector. This large power supply (collector PS) has the same potential as the electron source and is connected to wall power via an HV insulating transformer. It then applies a smaller, positive potential (+3 kV) to the collector, which is on a potential of -15 kV relative to the lab ground. Electrons are accelerated from the source into the main beam pipe to 18 keV, where experiments can be conducted (or particle beams potentially be cooled) and then decelerated by the collector optics to 3 keV and dumped there (see Figure 3.2). With this setup a $18\,keV$, $550\,mA$ electron beam can be produced in the middle section of the test bench, with the entire beam current provided by the collector power supply for only about $1.6\,kW$ instead of $10\,kW$ of wall power.
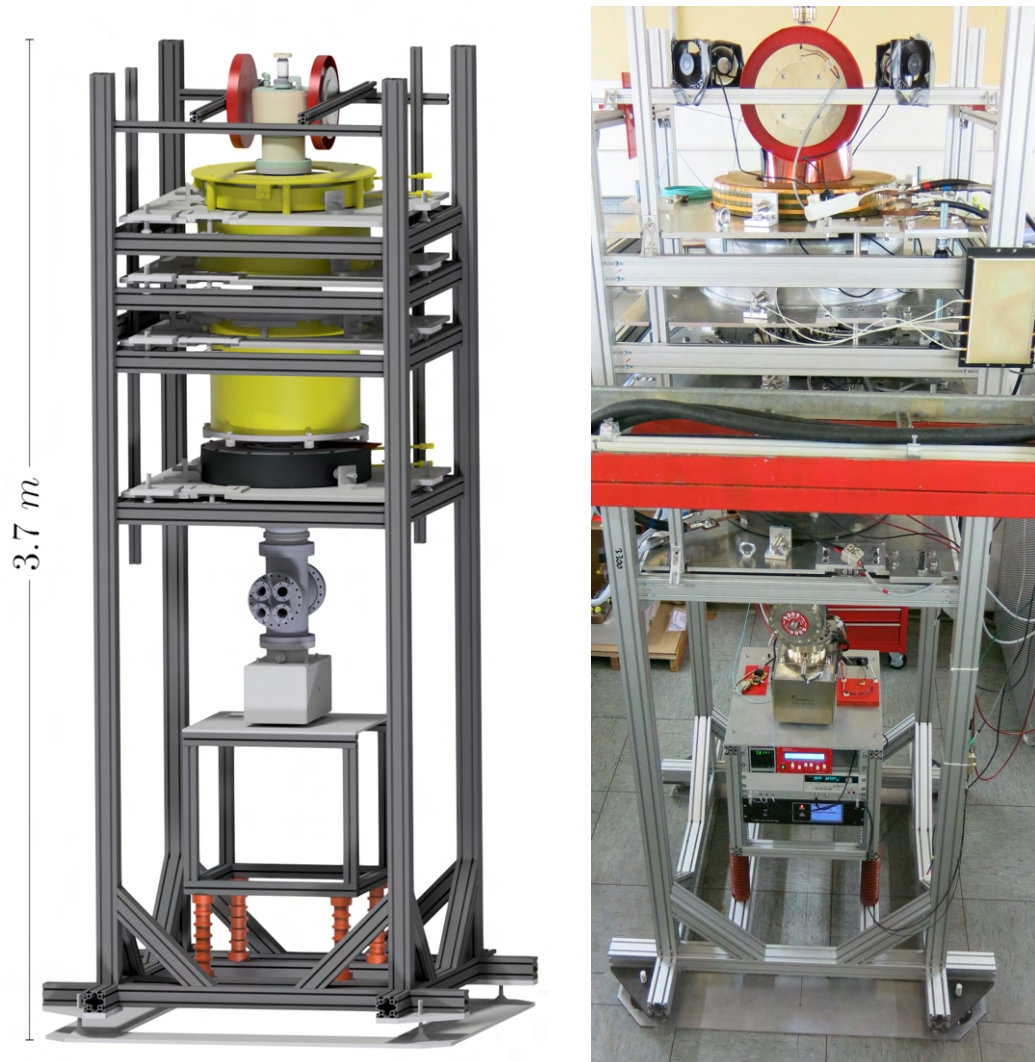
Figure 3.1.: CAD model of the test bench (*left*); photo of the test bench in the
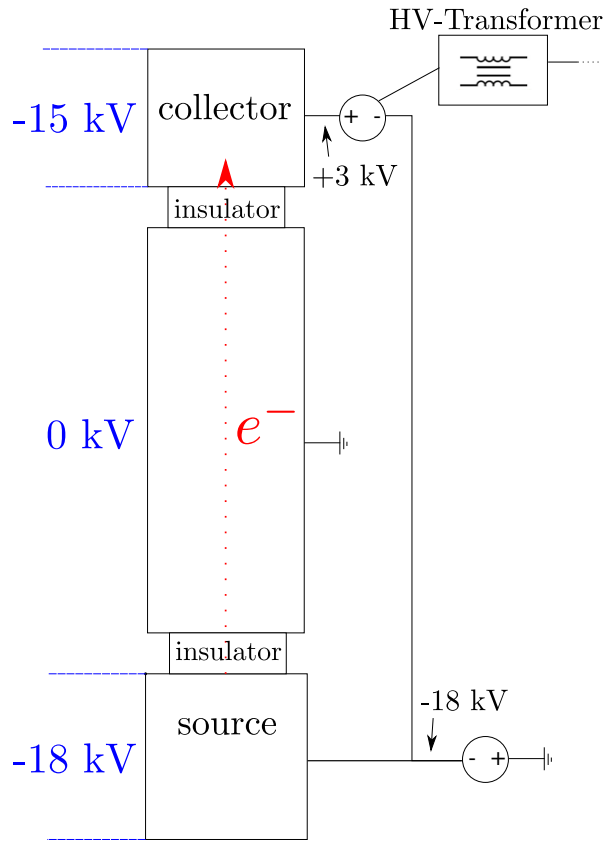KPH lab [12] (*right*).

Figure 3.2.: Schematic of the energy-recovery-setup; the potentials relative to the lab ground are shown in blue.
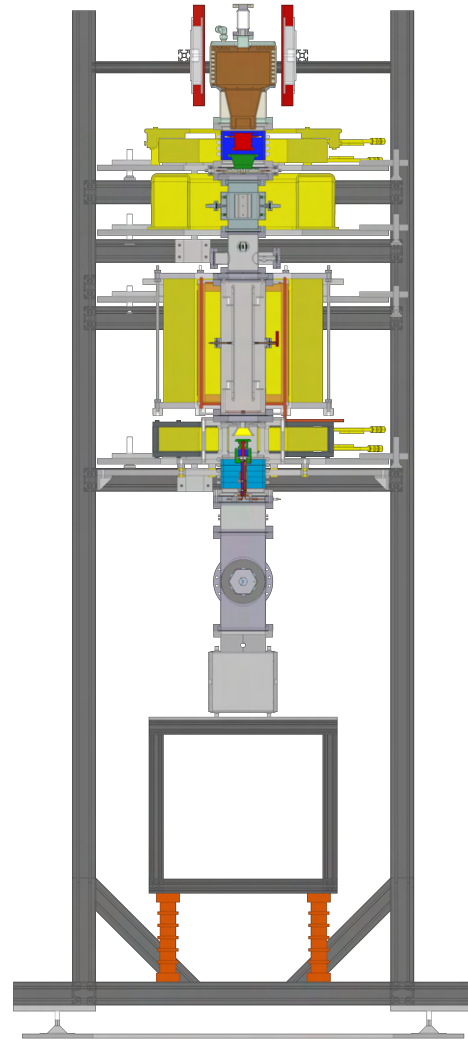
Figure 3.3.: Half section view of the test bench in extruded aluminum frame with 4 solenoids in yellow.

3.1.2. The Solenoids

The longitudinal magnetic field is created by 4 solenoids and envelops the cathode, the acceleration optics, a Wien filter, a segment with a viewport, a beam position monitor (BPM) and the deceleration optics (see Figures 3.3, 3.4). The maximum field is at the position of the electron emitting surface of the thermionic cathode. A gap between the Wien filter solenoid and the HV solenoid (legacy name; unrelated to the high voltage system of the test bench) was left open to facilitate access to the viewport.
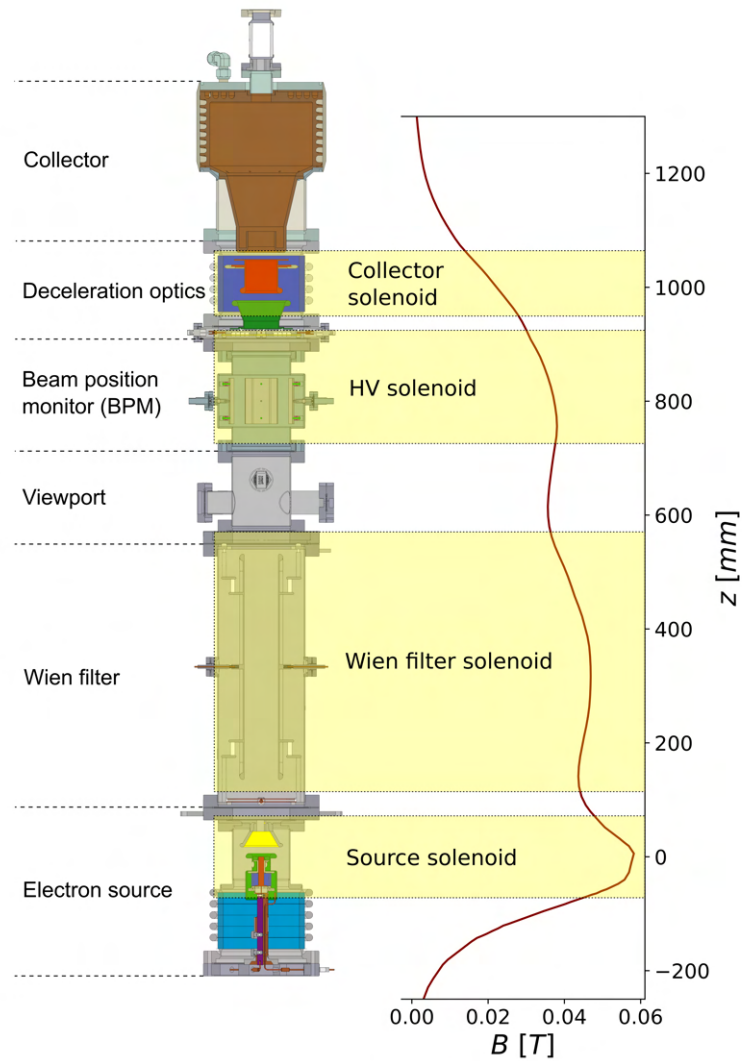
Figure 3.4.: Half section view of the test bench beam pipe with the sections, the solenoid positions (z-axis) and the simulated B-field strength along the z-axis $B(z)$ (x=0, y=0); (*HV solenoid* is a legacy name and unrelated to the high voltage system of the test bench).

3.1.3. The Wien Filter

A Wien filter exerts a direction of travel dependent electromagnetic force (Lorentz force F_L) on charged particles. In the case of electrons emitted from the thermionic source moving to the collector, the Wien filter is configured to balance out the

transverse Coulomb and the magnetic force.

$$\mathbf{F}_L = q(\mathbf{E} + \mathbf{v} \times \mathbf{B}) \tag{3.1}$$

Secondary electrons from the collector, generated e.g. by ionization, are deflected and dumped (on the Wien filters first aperture) to reduce their impact on the primary electron beam. This secondary current is in the order of $I_{sec} \approx 1\mu A$ for $I_{pri} \approx 550mA$. Detailed measurements can be found in [12], [13]. The present Wien filter was constructed in-house and is described in [25].

3.1.4. The Viewport

A viewport with a sapphire window (Ø 32mm) on a CF40 flange enables the view into the observation chamber behind it. The transmission of the window is approximately 85% from the UV- to the infrared part of the electromagnetic spectrum (see Figure 3.5). The chamber is blackened with a water-based colloidal graphite coating (Aquadag®) to suppress light reflections.
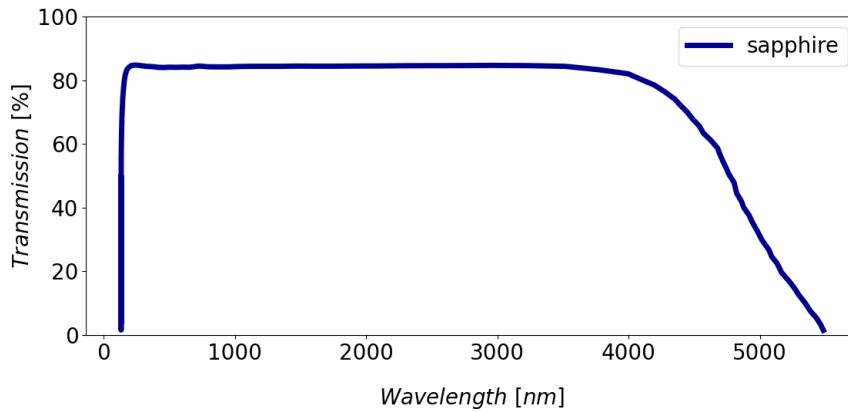
Figure 3.5.: Transmission curve of the sapphire window (according to the manufacturer [63]).

3.1.5. The Beam Position Monitor (BPM)

The BPM consists of two pairs of opposing metal plates (in the x and y direction) and is able to measure the position of the center of the electron beam charge non-invasively. The charged particles (i.e. the electrons) moving past the metal plates, which are insulated from the beam pipe, induce mirror charges in them (see Figure 3.6). This leads to the following mirror current in a plate

$$I_{mirror} = \frac{\mathrm{d}Q_{mirror}}{\mathrm{d}t} = \frac{A}{2\pi \cdot l \cdot s} \frac{\mathrm{d}Q_{e-beam}}{\mathrm{d}t} \tag{3.2}$$

with the area of the plate A, the length of the induced mirror charge in electron beam direction l and the transverse distance of the charge from the plate s. For a DC beam there is no change in the charge that influences the plate, meaning there is no mirror current. Therefore the beam current is modulated with $3\ MHz$ ($\Delta I < 10^{-6} A$) in the electron source. By comparing the measurements at opposing plates, the transverse position of the beam's center of charge can be determined.
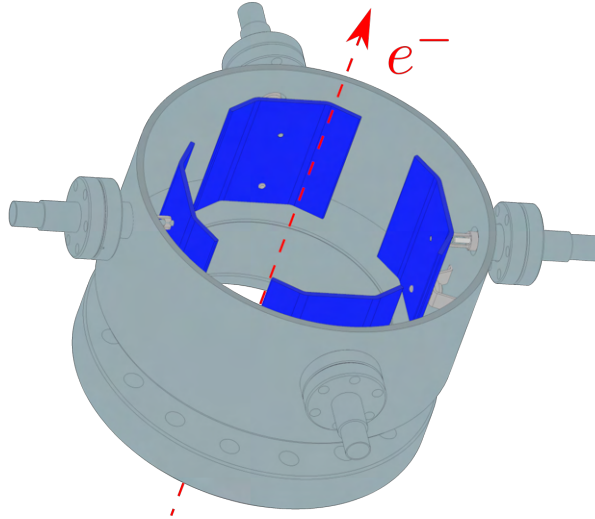

Figure 3.6.: The BPM module with the metal plates (insulated from the beam pipe), where the mirror charges are induced (*blue*).

3.1.6. The Deceleration Optics

Four insulated ring segments with a $25\ mm$ aperture form a scraper, which can detect a misaligned or overly wide electron beam on the individual segments. Downstream from that scraper is the deceleration electrode, on lab ground potential and identically shaped to the anode. Between that and the collector, the suppressor electrode is situated (see Figure 3.7). The suppressor electrode's potential is slightly more negative than that of the collector (in relation to lab ground; $U_{supressor} = -16kV$), which reflects low energy electron originating from inside the collector, as a result.

3.1.7. The Collector

The collector installed at the test bench is identical to the one used for the Cooler Synchrotron (COSY) cooler at FZ Jülich [14]. Behind the collector entrance the inner copper part extends conically to a larger diameter (Ø180 mm), where spiral cooling fins contact the outer, stainless steel shell. The recess between the shell and the fins acts like tubing, where insulating transformer oil is pumped through, to move away the heat created by dumping the decelerated electron beam. The

solenoid field barely reaches the wider part of the collector, where space charge related beam blow up occurs. The now large beam is then steered into the side wall by a pair of Helmholtz coils, to further spatially distribute heating of the collector and to protect the ion getter pump / vacuum gauge mounted atop the collector (see Figure 3.7).
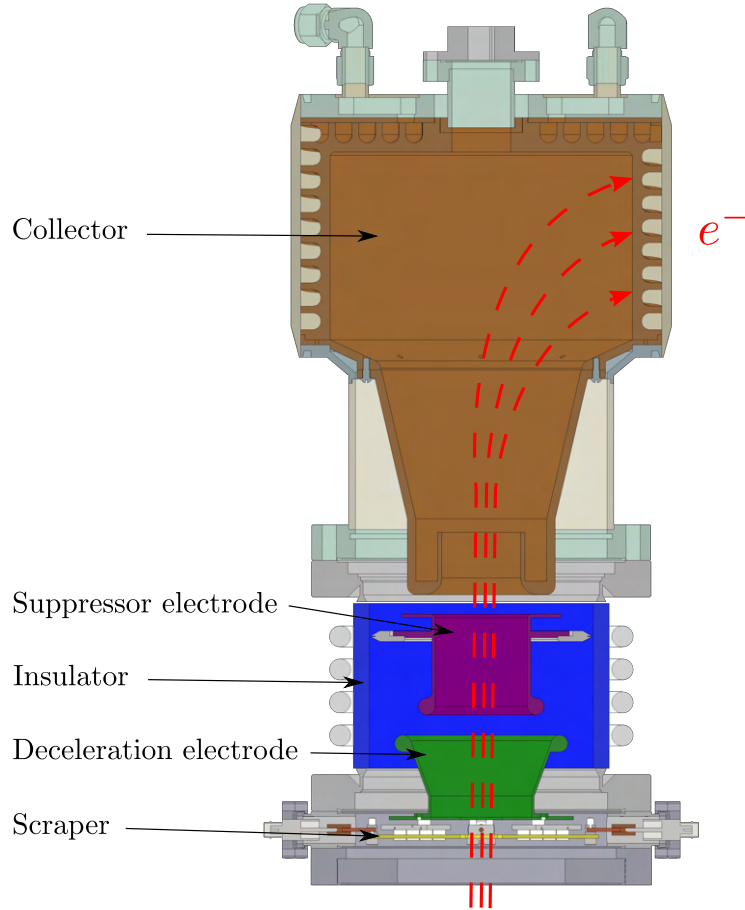

Figure 3.7.: Half cut section view of the deceleration optics and the collector, with the insulator (*blue*), the scraper segments (*yellow*), deceleration electrode (*green*), the suppressor electrode (*purple*) and examplary electron trajectories (*red*).

3.1.8. The Electron Source

The electrons are provided by a thermionic barium dispenser cathode with an extraction voltage of $U_{source} = -17\,kV$ (see Figure 3.8 *left*). The cathode reaches a temperature of $T_{cathode} \approx 1000 - 1100°C$ with about $P_{heat} \approx 20\,W$ of heating power. A Pierce electrode (PE) controls the magnitude of the extracted current $I_{e^-} = I_{col} = 0 - 550\,mA$ (provided by the collector power supply, see section

3.1.1) and spatially homogenizes the energy distribution of the electrons leaving the dispenser cathode, i.e. its electrical field counteracts the transversal space charge effects, forcing the emitted electrons onto a straight trajectory. The Pierce electrodes potential is negative compared to U_{source} and prevents electron emission with $U_{PE} = -3\,kV$ ($U_{PE,lab} = -20\,kV$ relative to lab ground) and facilitates $I_{e-} = 550\,mA$ with $U_{PE} = 0.3\,kV$ for the given source potential, respectively. The extractable current is described by the *Child-Langmuir-law* [54]:

$$I_{e-} = P_{source} \cdot U_{source}^{3/2} \tag{3.3}$$

with the so called *perveance* P_{source} approximately determined by the source geometry (i.e. the electron beam radius r_0 and the distance between cathode and anode d)

$$P_{source} = \left(\frac{r_0}{d}\right)^2 P_0 \,, \; P_0 = \frac{4}{9}\pi\varepsilon_0 c\sqrt{\frac{e}{m_e c^2}} \tag{3.4}$$

Simulations by TSL resulted in $P = 2.4 \cdot 10^{-7}\,A\,V^{-3/2}$ for the initial source design [62].

3.1.9. Gas Discharges in the Electron Source for Strong Electromagnetic Fields

The electron source produced by TSL (Uppsala) [56] was based on a layout developed for the Recycler Electron Cooler at Fermilab and designed for operation outside of a solenoid field [60]. In a previous dissertation experimenting with the electron cooler test bench [12] it was operated inside a solenoid field [11] and noted, that for certain electromagnetic field configurations in the electron source (i.e. accelerating potential $U_{source} < -17\,kV$ and solenoid field $B_{source} > 60\,mT$) gas discharges seemed to ignite and sustain themselves, which resulted in a rapid increase in pressure ($\frac{\partial}{\partial t}p \approx 10^{-8}\,mbar/s$) and therefore caused a breakdown of operation. With the help of simulations (via CST Studio Suite) it was concluded that for certain EM field configurations charged particles (e.g. electrons from field emission, cosmic radiation) are forced onto very long trajectories and are basically trapped in specific regions, where they have a high probability to ionize the residual gas and consequently ignite the discharge. These suspected regions A and B are depicted in Figure 3.9 (taken from [12]) assuming a longitudinal B-field in the z-direction. A modification of the Pierce electrode to shorten region B and remove region A was suggested.
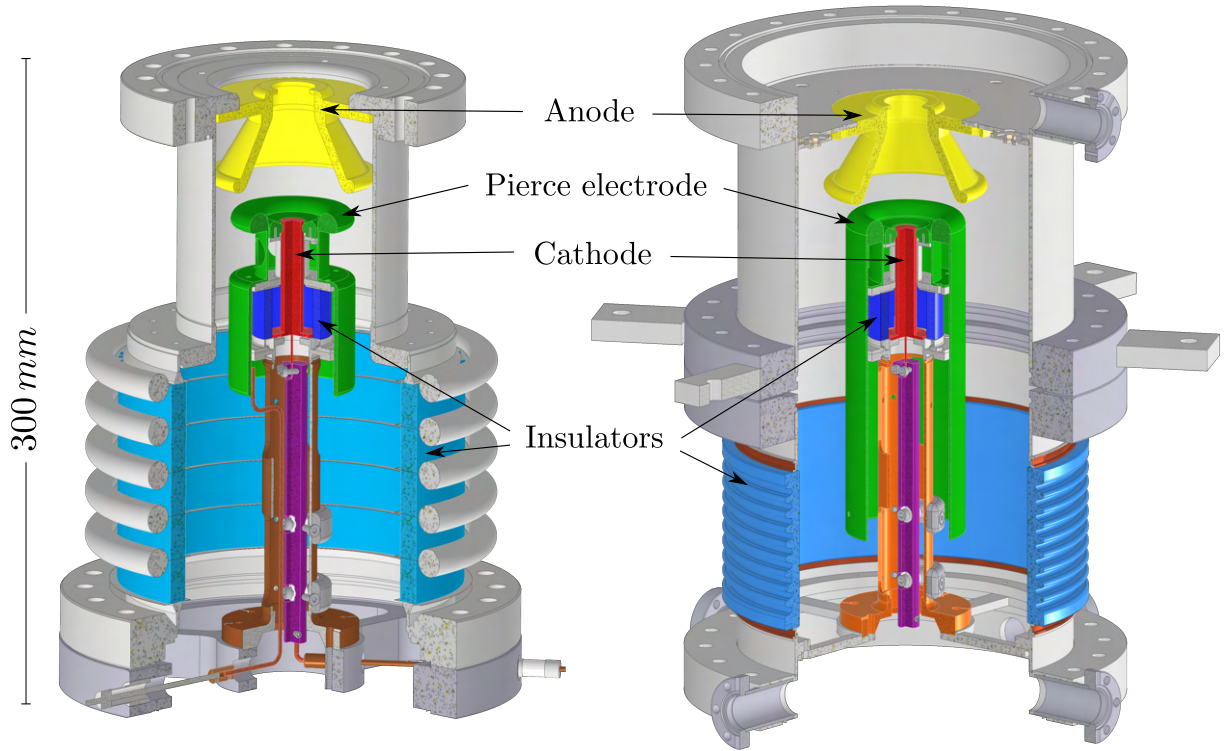
Figure 3.8.: Three quarter section view of the initial (*left*) and the upgraded (*right*) electron source design, with the following color coded parts: anode (*yellow*), cathode (*red*), Pierce electrode (*green*), ceramic insulators (*dark and light blue*).

3.1.10. The Electron Source Upgrade

Since the test bench had to be moved to a different laboratory for the experiments described later in this thesis, a new Pierce electrode was designed, under the premise of reusing as many components of the source as possible and keeping the geometry, relevant for the source's perveance, identical. Simulations with CST Studio Suite (see Figure 3.10) showed the desired results. Subsequently, the new Pierce electrode was manufactured in-house (by the KPH mechanical workshop). A new ceramic insulator was fabricated by an external company to permit source voltages of up to $U_{source} = -30\,kV$ and the top part of the source, housing the anode was widened to fit the Wien filter on top without an adapter flange (see Figure 3.8 *right*). All source components were cleaned (in an ultra sonic bath), assembled in the HIM cleanroom (see Figure 3.11) and prepared for HV tests (see also Chapter A.2.5).
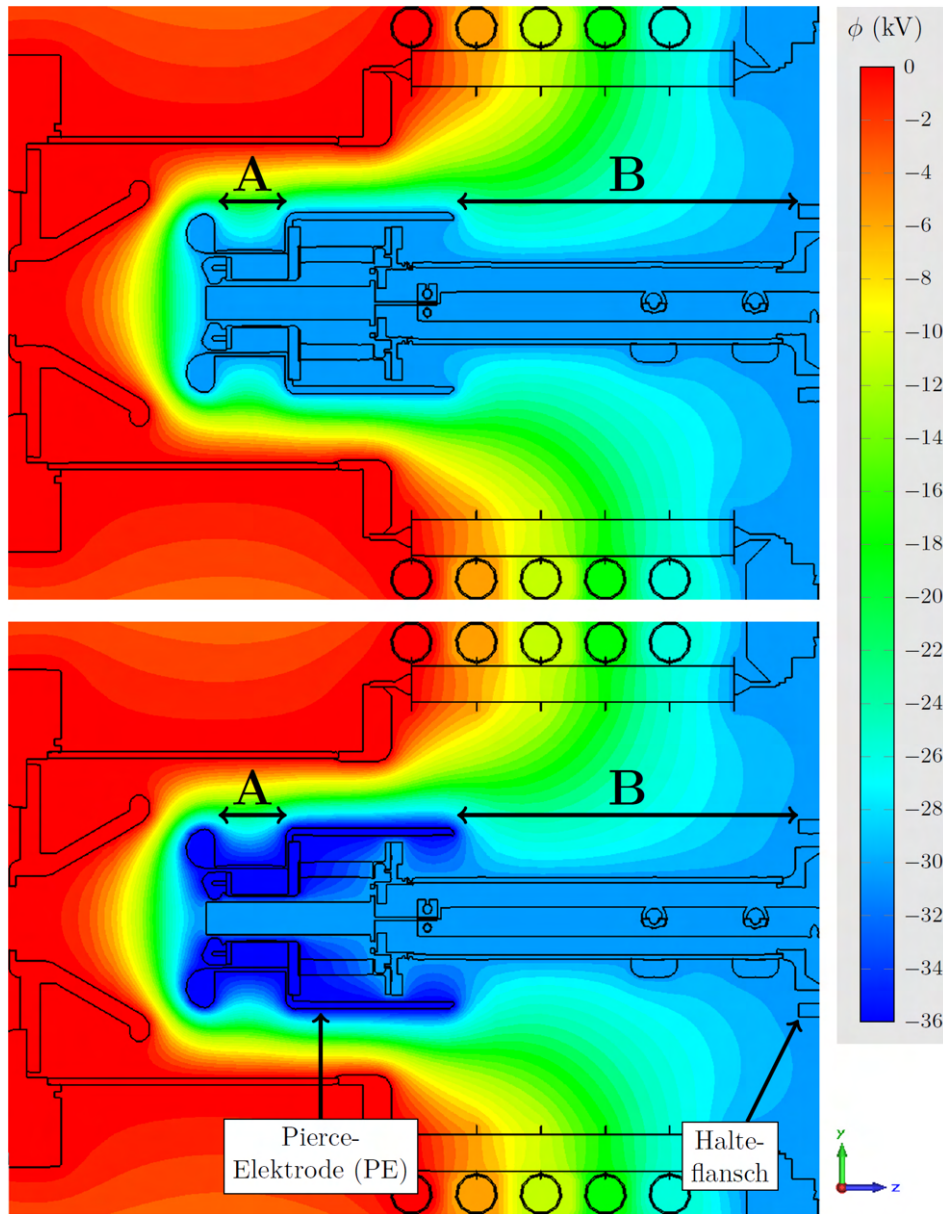
Figure 3.9.: Half cut section of the initial electron source in the y-z-plane, with its potential ($U_{source} = -30\,kV$) for two different Pierce electrode potentials (top: $U_{PE} = 0\,kV$, bottom: $U_{PE} = -6\,kV$) (This image was taken from [12]).
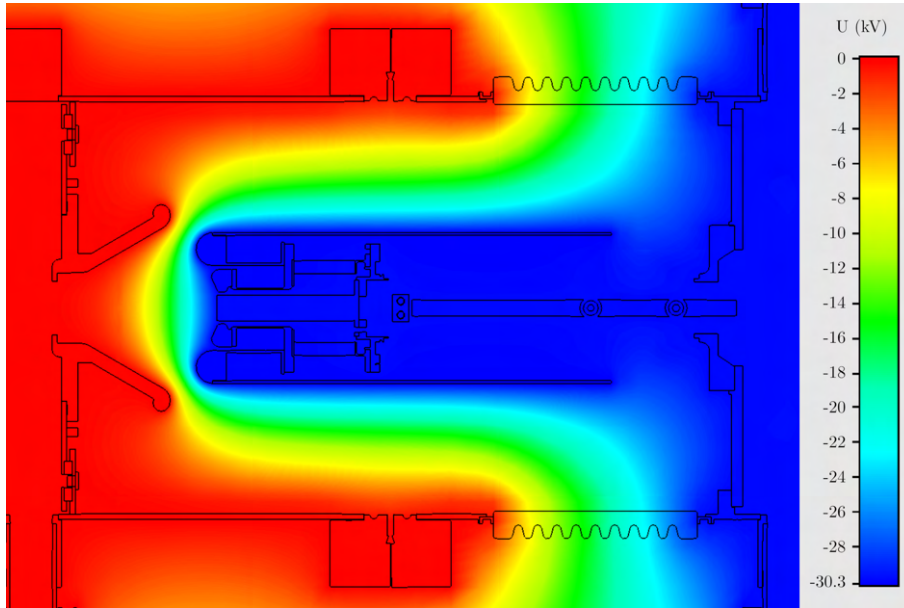
Figure 3.10.: Half cut section of the *upgraded* electron source in the y-z-plane, with its potential ($U_{source} = -30\,kV$, $U_{PE} = 0.3\,kV$).
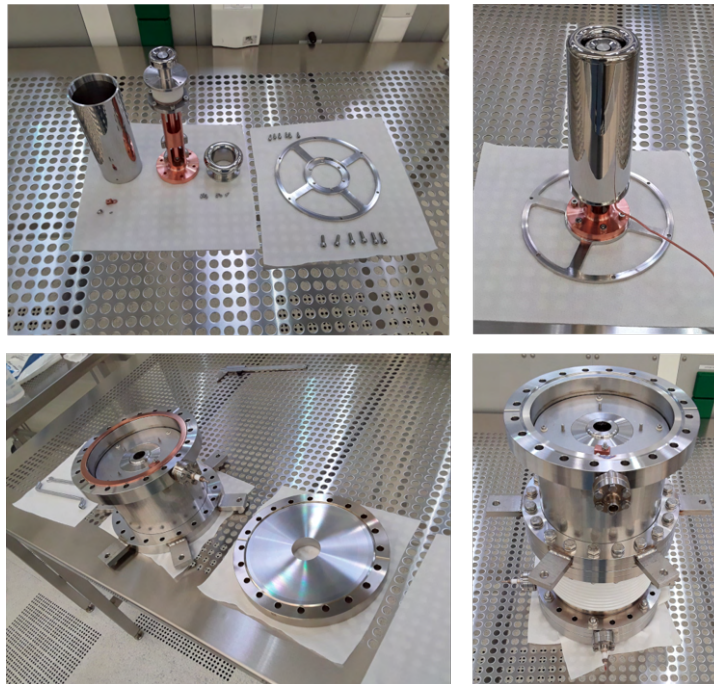

Figure 3.11.: The upgraded electron source in different stages of assembly in the HIM cleanroom.

3.1.11. High Voltage Tests

Only the assembled source was put into place at the test bench, closed up with a blank flange and outfitted with the source solenoid (see Figure 3.12). The source was evacuated and baked out ($T = 150°C$) until it reached Ultra-High Vacuum (UHV) conditions ($p = 8 \cdot 10^{-11}\,mbar$). The cathode was not heated, therefore no electrons could be emitted during this test. The required B-field strength at the cathode for operation of the test bench at $U_{source} = -30\,kV$ (and therefore $I_{e-} > 1\,A$) was determined to be $B_{source} = 60\,mT$ via start-to-end CST particle tracking simulations (see Figure 3.13). For the test, a constant magnetic field was set, the source voltage ramped up in $1\,kV$ increments and at those increments the pierce voltage was varied in the voltage regions need for operation. If that configuration was robust against gas discharges, the test was repeated with a stronger magnetic field and so on. The likelihood of ignition seemed to be proportional to both U_{source} and B_{source}, i.e. for lower B_{source} a higher U_{source} could be set without causing gas discharges and vice versa. At $B_{source} = 60\,mT$ with the potentials $U_{source} = -30\,kV$ and $U_{PE} = 0 - (-6)\,kV$ no gas discharges occurred, meaning the upgrade was proven successful.
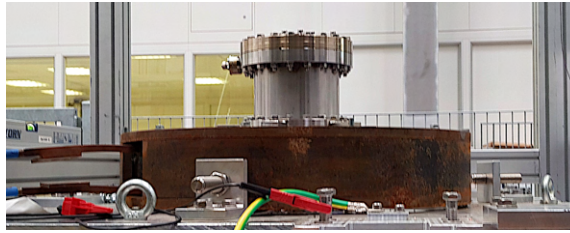

Figure 3.12.: The upgraded electron source during preparation of HV tests.

In the event of inaccuracies in the tracking simulation and the resulting need for even stronger solenoid fields, it was decided to test the electron source for the maximum magnetic field of the source solenoid ($B_{source} = 88\,mT$, determined by the solenoids thermal design). The gas discharge reappeared. To investigate this behaviour, further particle tracking simulations of the status quo were carried out. A large number of electrons (10^4) were started on the outside of the tubular part of the Pierce electrode with thermal energy ($E_{kin} = 0.025\,eV$) to find unusually long trajectories. For a given simulation time of $t_{sim} = 4\,\mu s$ (i.e the maximum time of flight along a trajectory, determined by the compute time, in this case about 48-72 h), the tracking algorithm produced trajectories of which 0.2% did not terminate or leave the simulation area (see Figure 3.14). As a comparison, an electron needs only $t_{e-beam} = 20ns$ to travel from the cathode to the collector walls. This shows that, with this source geometry and EM field configuration, some electrons are still trapped and probably able to ionize the residual gas. The electron trajectories wrapping around the tubular part of the Pierce electrode
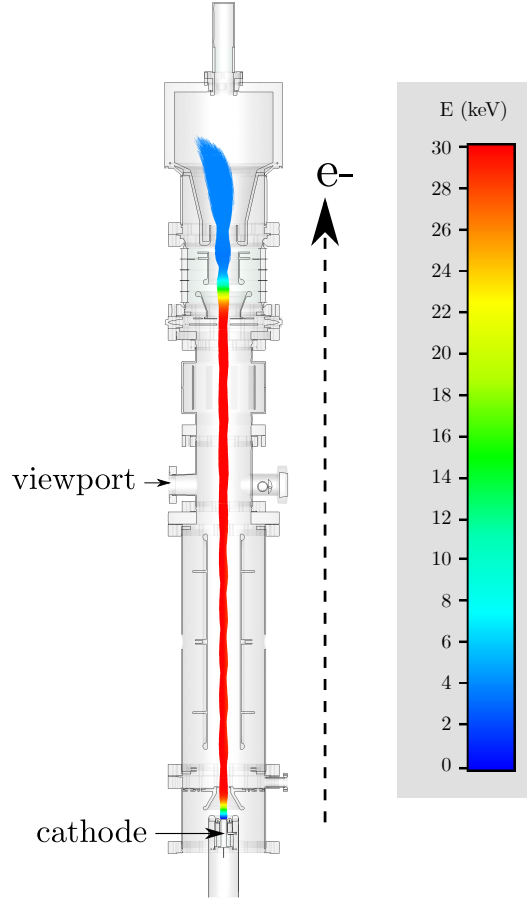
Figure 3.13.: The CST particle tracking simulation for $U_{source} = -30\,kV$.

conically, where they gain kinetic energy of up to $E_{kin} = 14\,keV$, suggest some kind of trapping of electrons. Examining trajectories that did not terminate more closely (see Figure 3.15) seemed to confirm that assumption. Investigating the area of the source showed minima of the electric potential along the solenoid field lines (see Figure 3.16), where electrons with sufficiently low starting energy might not escape and terminate at the source walls. They are trapped radially by the magnetic and axially by the electric field, a concept utilized to capture particles in a Penning trap [19]. At first, further modifications of the source were considered. An extension of the anode potential over the whole tubular part of the Pierce electrode would be possible, due to the high dielectric breakdown voltage inside a UHV vessel ($U_{break} \approx 1\,kV/mm$). Simulations deemed that to be unsuitable. Another possibility was to try straighten out the solenoid field lines and make them parallel to the electron beam axis. This can be achieved by adding a second solenoid below the source solenoid. According to additional simulations this change in EM field configuration is successful in eliminating minima along the magnetic
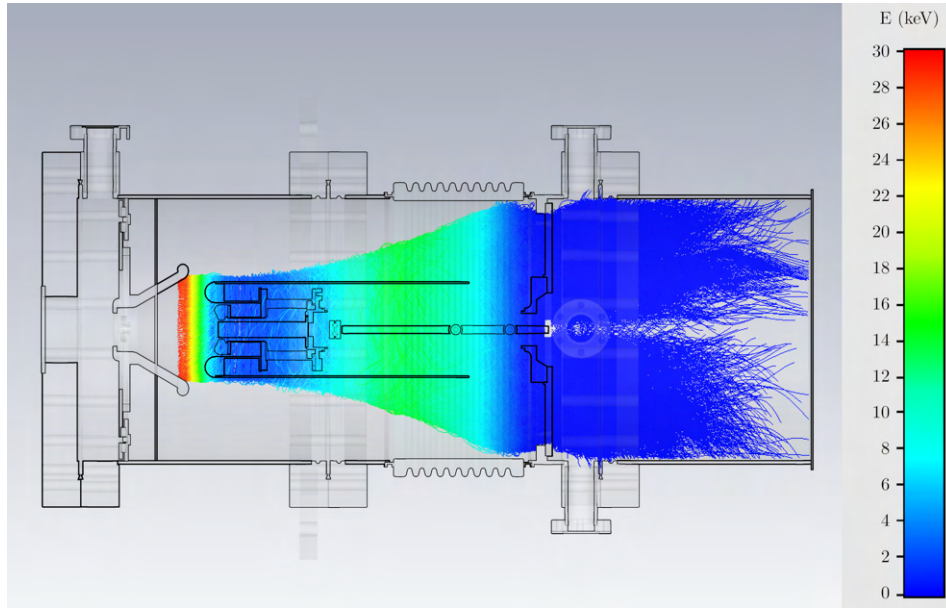
Figure 3.14.: CST particle tracking simulation of 10^4 field emission electrons started on the outside of the tubular part of the Pierce electrode, with a simulation time of $t_{sim} = 4\,\mu s$.
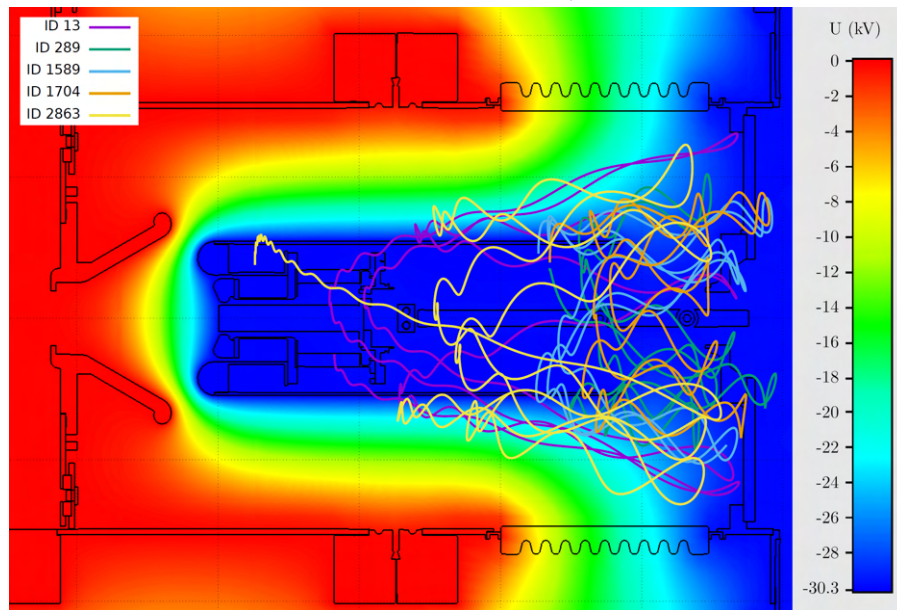

Figure 3.15.: 2D projection of 5 Trajectories that did not terminate in the simulation, for a simulation time of $t_{sim} = 45\,ns$.

field lines (see Figure 3.17). All simulated trajectories terminate after $t_{sim} = 28\,ns$ (see Figure 3.18). The collector solenoid of the test bench is identical to the source
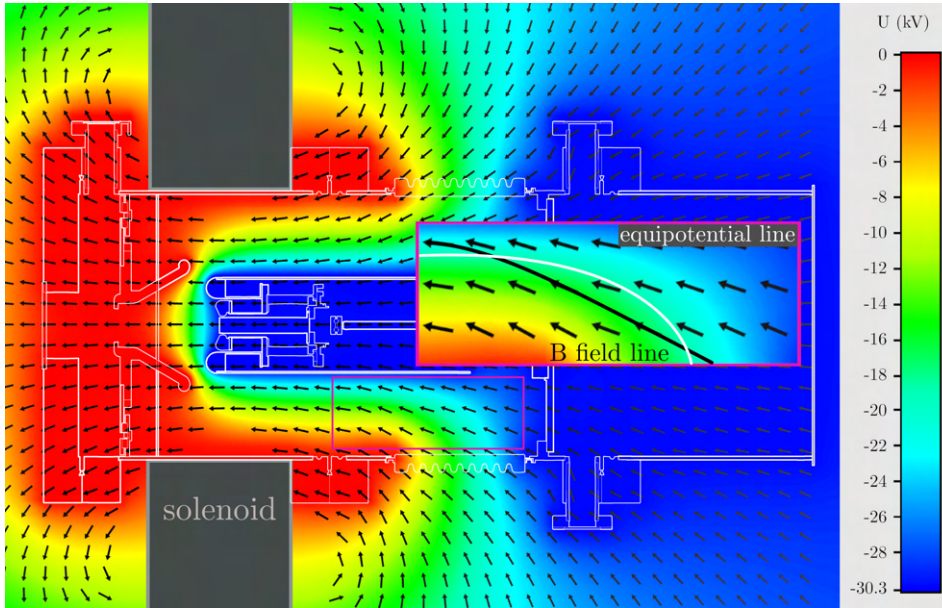
Figure 3.16.: CST Simulation of the potential (heat map) and the solenoid field (black arrows) on the y-z-plane. Potential minima along the magnetic field lines (represented by black arrows) in the pink rectangle.
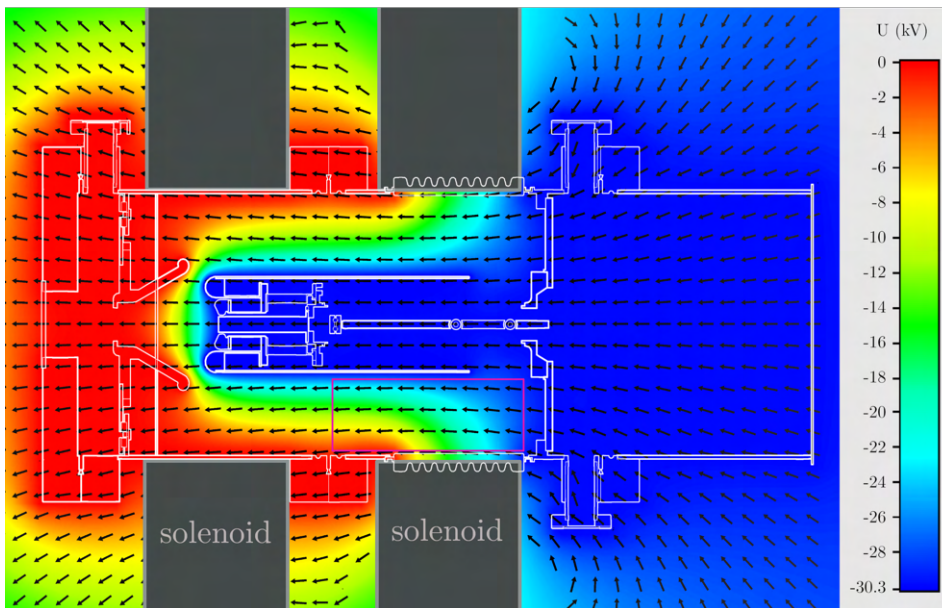
Figure 3.17.: CST Simulation of the potential (heat map) and the modified solenoid field (black arrows) on the y-z-plane. No potential minima along the magnetic field lines (represented by black arrows) in the pink rectangle.

solenoid, except for a yoke, so the simulated new EM field configuration could be assembled temporarily. This setup proved to be robust against gas discharges, for an accelerating voltage $U_{source} = -30\,kV$ and a combined solenoid field with $B_{source} = 115\,mT$. If needed, the test bench could be outfitted with an additional solenoid, without breaking the vacuum, in the future.
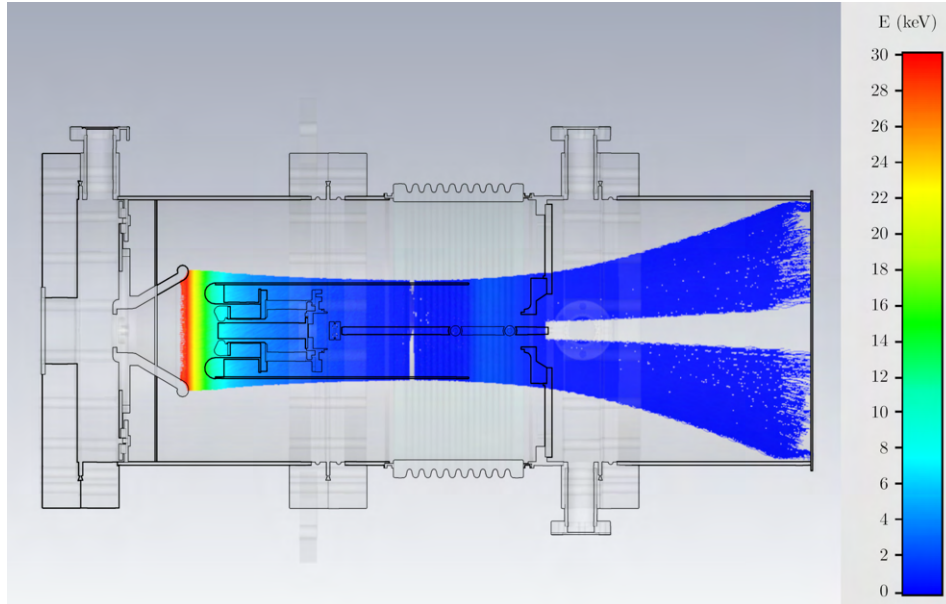

Figure 3.18.: CST particle tracking simulation of 10^4 field emission electrons started on the outside of the tubular part of the Pierce electrode, with a simulation time of $t_{sim} = 28\,ns$.

3.1.12. Setup of the Test Bench

After the HV tests, the deceleration optics were outfitted with a ceramic insulator identical to the new one at the source, preserving the initial geometry (see Figure 3.19). All parts of the vacuum vessel were installed on top of the source and baked-out at $T = 200° C$ over 5 days (see Figure 3.20), arriving at a final pressure of $p = 3 \cdot 10^{-11} \, mbar$. Afterwards the solenoids were positioned according to the simulations, then all necessary electrical and coolant connections were made.
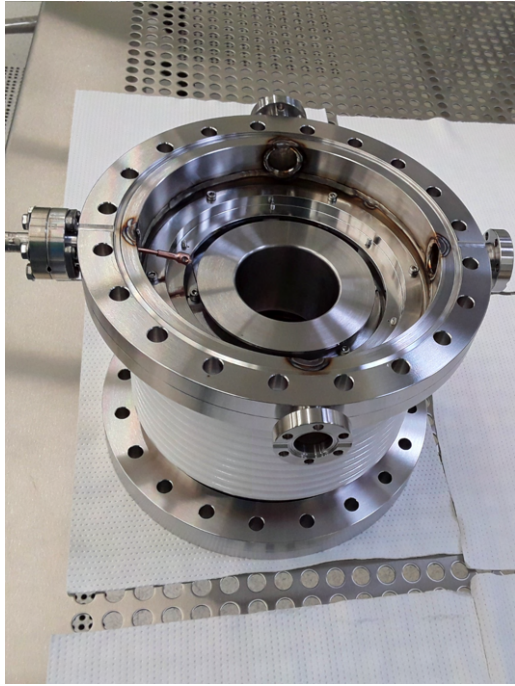
Figure 3.19.: Assembled deceleration optics with the new insulator in the HIM cleanroom.

Figure 3.20.: The vacuum vessel of the electron cooler test bench during bake-out preparations.

3.2. High Voltage Switch for Beam Interruptions

Under the assumption that residual gas particles in the test bench get ionized and consequently trapped in the potential of the electron beam, it would be convenient if the beam could be interrupted for a short time, to allow ions to reach the vacuum pipe and neutralize. This so called *ion clearing* was implemented at the recycler electron cooler at Fermilab and significantly improved it's cooling rate [1] [2]. To achieve this pulsing of the electron beam a fast, HV-capable switch (see Figures 3.22, 3.23), controlled by a pulse generator was connected to the Pierce electrode. Two power supplies, set to voltages allowing and prohibiting electron emission of the cathode respectively, were switched between and therefore used to charge and discharge the Pierce electrode. The limiting factors of such a setup are the maximum frequency, the peak current capabilities of the switch and the capacitive load of the Pierce electrode itself. The capacity was measured to be $C_{Pierce} = 780\,pF$ (including the connected cable). In the case at hand the power limit of the current inrush constraining resistors ($R = 1\,M\Omega$, $P_{max} = 2\,W$) would allow a pulse frequency of $f_{max} = 34\,Hz$, but for first measurements a frequency of $f = 15\,Hz$ was chosen, in accordance with the experiments at Fermilab (see Figure 3.21).

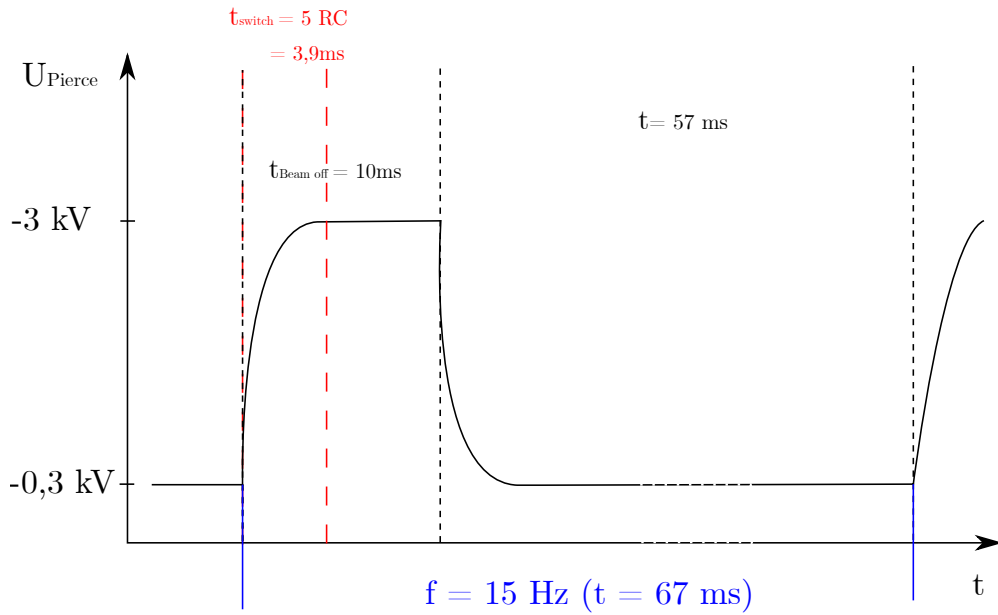**Figure 3.21.:** Pulsing scheme for ion clearing operation at the test bench.
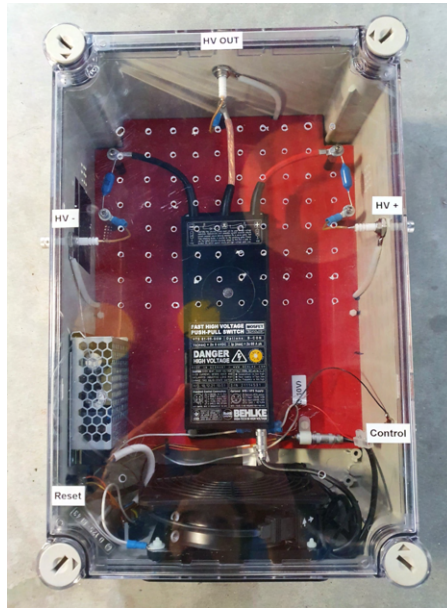
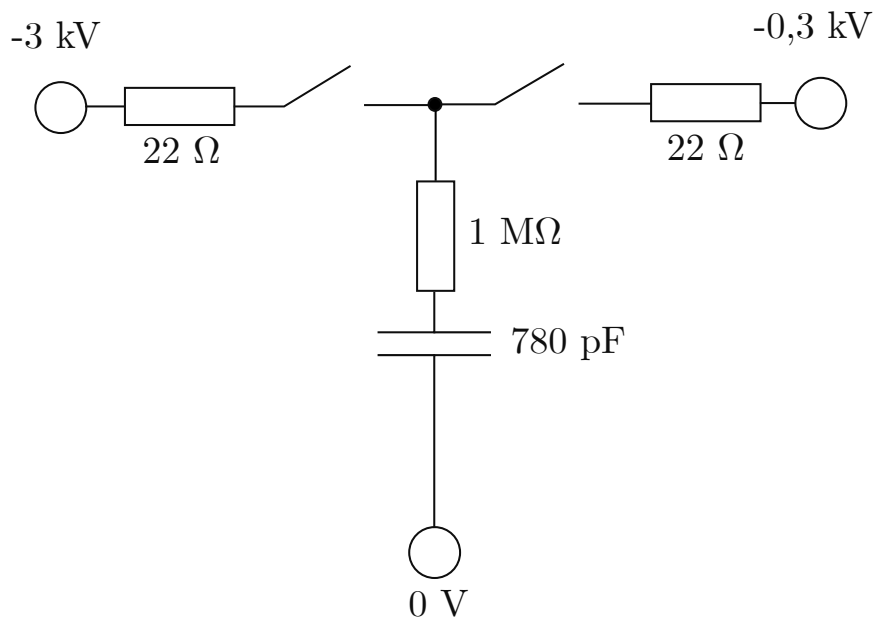**Figure 3.22.:** HV-switch with power supply and cooling fan.

Figure 3.23.: HV-switch schematic

3.3. Safety Measures

At the new installation location in the large HIM lab hall, which has a widespread user base, safety hazards needed to be mitigated. Radiation (Bremsstrahlung) and potentially deadly high voltage needed to be shielded against. During normal operation (with $U_{source} = -17\,kV$) no radiation could be detected outside the vacuum vessel of the test bench, but for higher source potentials and the possibility of total beam loss, caused by malfunctioning solenoids and interlocks, a lead shielding was required. To properly scale the thickness of the lead shielding, the maximum capabilities of the source's power supply ($U_{source,\,max} = -35\,kV$, $I_{source,\,max} = 10\,mA$) had to be taken into account. In case of total beam loss (e.g. on the scraper) the energy recovery ceases operation and the source power supply might provide a $I_{e-} = 10\,mA$ electron beam (if its interlock also fails). Lead sheets with a thickness of $d = 1\,mm$ and $d = 1.5\,mm$ are commonly available. Disregarding the shielding capabilities of the solenoids and the vacuum vessel itself, a $1\,mm$ lead shielding results an equivalent dose (standard human) in a distance of $1\,m$ of $D = 0.5\,\mu Sv/h$, a $1.5\,mm$ shielding results in $D = 1.2 \cdot 10^{-5}\,\mu Sv/h$ [47]. (*For comparison:* average natural dose rate in Germany is $D = 0.08\,\mu Sv/h$ [21].) The $1.5\,mm$ shielding was chosen to allow further upgrades in the future.

A framework for the shielding was designed out of extruded aluminium and fitted with 44 sheets of lead ($A \approx 1\,m^2$), sandwiched between two $1\,mm$ aluminium plates. The structural integrity of the framework was verified by the engineer at KPH for the weight of the shielding ($m_{shield} \approx 1t$). Each sheet was connected to lab ground and secured against removal from the outside. A door was installed in the bottom half of the enclosure, the top half acts as a lid and can be moved with the crane of the lab hall. This access to the test bench proved to be essential, when the HV transformer needed to be replaced and a coolant leakage at the collector had to be remedied (see Figure 3.24).

Opening the door of the enclosure controls the interlock system of the test bench, i.e. as soon as the door is opened the outputs of the HV power supplies are switched off. Power loss of the interlock system has the same effect (see [12] for a detailed description). In addition, two metal rods force the potentials, that can be reached on the outside of the test bench (U_{source}, $U_{collector}$) to ground mechanically (see Figure 3.25).
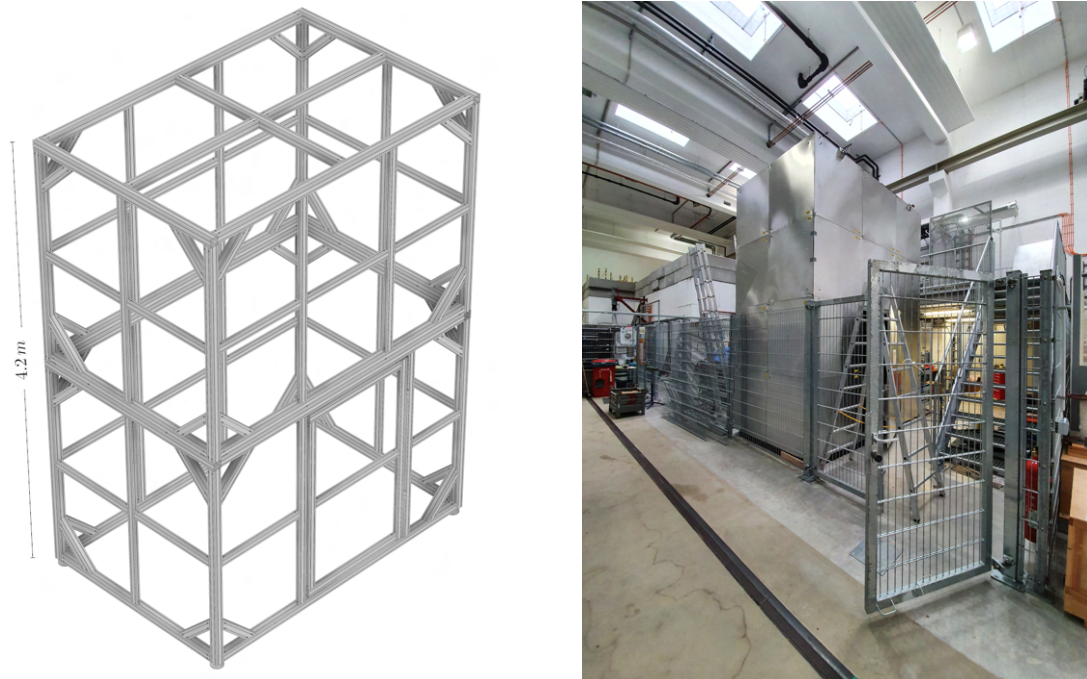
Figure 3.24.: CAD model of the framework for the shielding (*left*); photo of the test bench inside its shielding in the HIM lab hall (*right*).
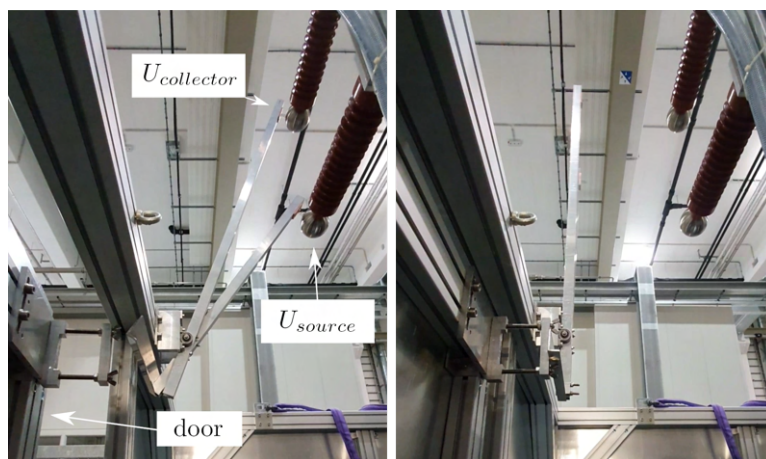

Figure 3.25.: Mechanism to force grounding inside the enclosure (prior to connection with lab ground).

3.4. Setups for Optical Measurements

3.4.1. Photomultiplier Tube (PMT) Setup

For first measurements of the BIF a setup with a PMT and a motorized lens and slit was utilized (see Figure 3.26). The lens was positioned in front of the viewport at a distance of approximately two times its focal length from the middle of the beam pipe. The motor was used to move the focus of the PMT setup. In front the PMT the slit could be moved sideways to scan along the width of the observed area, i.e. perpendicular to the electron beam. In addition to background photons
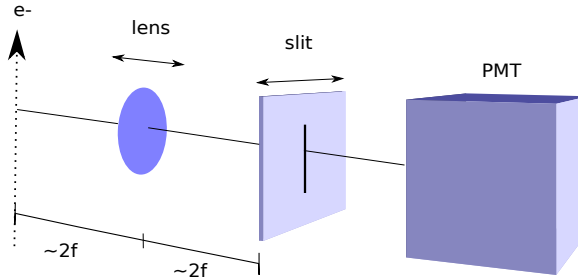

Figure 3.26.: Sketch of the PMT setup.

emitted by the heated cathode, at the position of the electron beam, a structured signal was found over the optical range of the EM spectrum $(400 - 700\,nm)$. The signal was assumed to be beam induced fluorescence (BIF). This assumption, in conjunction with the long measurement time of the PMT setup (approximately $90\,min$) motivated the next iteration of measuring equipment.

3.4.2. Low Light Cameras

At the time of publication of the thesis, two kinds of digital cameras capable of single photon counting are available: electron multiplying CCD *(emCCD)* and scientific CMOS *(sCMOS)* cameras. The measurement process with such image sensors is a two step process. Firstly: photon to electron conversion, secondly: electron to voltage conversion. The emCCD chip multiplies electrons after the first step, before the conversion into a voltage. On the other hand, both steps happen on the pixel itself for a sCMOS sensor [5], [29]. Although, the quantum efficiency (i.e. the low light capabilities) of an emCCD camera is about 12% higher and its readout noise and dark current are lower than the sCMOS variant, it has a lower resolution, needs to be cooled more, its gain register degrades over time and it costs approximately twice as much (see Table 3.1) [27], [28].

A company agreed to demonstrate both types at the test bench, to aid in the decision making process. Either camera was put in the same spot in front of the viewport of the test bench, with the same lens and bandpass filter $(425 - 475\,nm)$ (see Figures 3.27, 3.28).

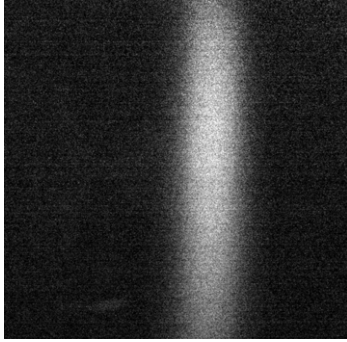| Type	QE_{max}	Resolution	T_{sensor}	dark current	readout-noise$_{rms}$
emCCD	94%	512×512	$-65°C$	0.005 e-/pixel/s	1 e-/pixel
sCMOS	82%	2048×2048	$-10°C$	0.06 e-/pixel/s	1.4 e-/pixel

Table 3.1.: Camera comparison: emCCD, sCMOS.

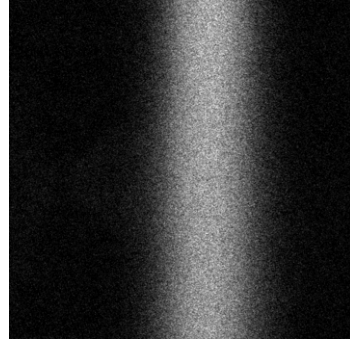**Figure 3.27.:** Image of the BIF taken with the sCMOS camera (4x4 binning for comparison with emCCD); $t_{exposure} = 5\,s$.

Figure 3.28.: Image of the BIF taken with the emCCD camera at maximum gain; $t_{exposure} = 5\,s$.

A comparison of a horizontal profile of both images, with appropriate scaling, shows what looks like a similar signal to noise ratio in this application (see Figure 3.29). Taking this information and the fact of the emCCDs high sensitivity to accidental over-exposure into account, the sCMOS camera was purchased.
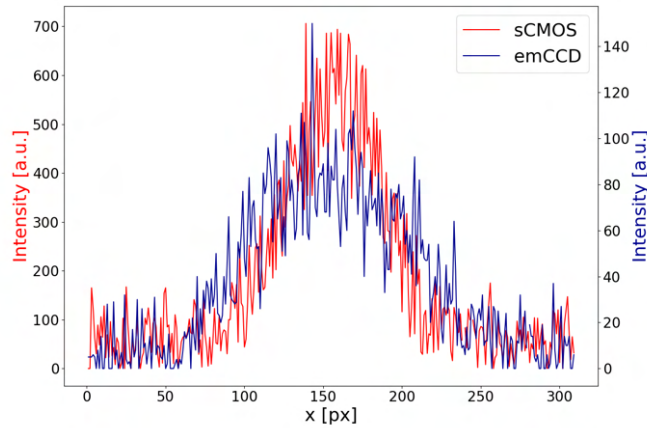

Figure 3.29.: Comparison of 2 horizontal profiles from Figures 3.27, 3.28, scaled on the y-axis (in arbitrary units).

3.4.3. The sCMOS Camera

The lens attached to the sCMOS camera had to be set to focus on the observation site (i.e. the middle of the beam pipe) and to optimize photon capture (lens: $35\,mm$, fixed focal length) [23]. The selection of the largest aperture, to maximize photon yield, results in a shallow depth of field [30]. A checkerboard pattern (5×5 with a checker size of $5\,mm$) was used to determine the distance, where an in-focus image could be captured and to measure the pixel density per millimeter at that given distance. The camera was mounted on a motorized stage to vary the distance to the pattern and a ring light was added to ensure even illumination (see Figure 3.30).
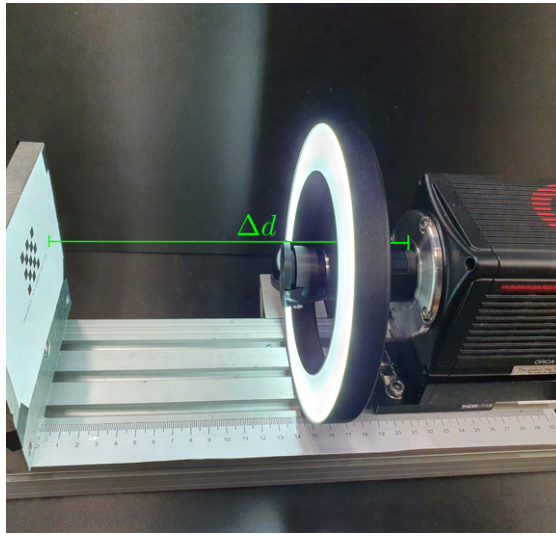

Figure 3.30.: The sCMOS camera on a motorized stage, the checkerboard pattern and a LED ring light.

To define the sharpness, a horizontal profile of the checkerboard images (at distances $\Delta d = 198 - 223\,mm$ in $0.5\,mm$ increments) was examined for the steepness of the intensity change for the transition between black and white. The blurrier an edge of a checkerboard square, the less steep the intensity change. For consistency the intensity change of the transitions white-black-white in the middle row of the pattern was fitted linearly. The average of the two highest and the two lowest intensities, utilized for the fits, was used then to find the corresponding x-value of both linear fits. This provided two distances in the x direction of the profile plot (A,B), the ratio of which was used as a measure for *sharpness*. The higher A/B, the *sharper* the image (see Figure 3.31).
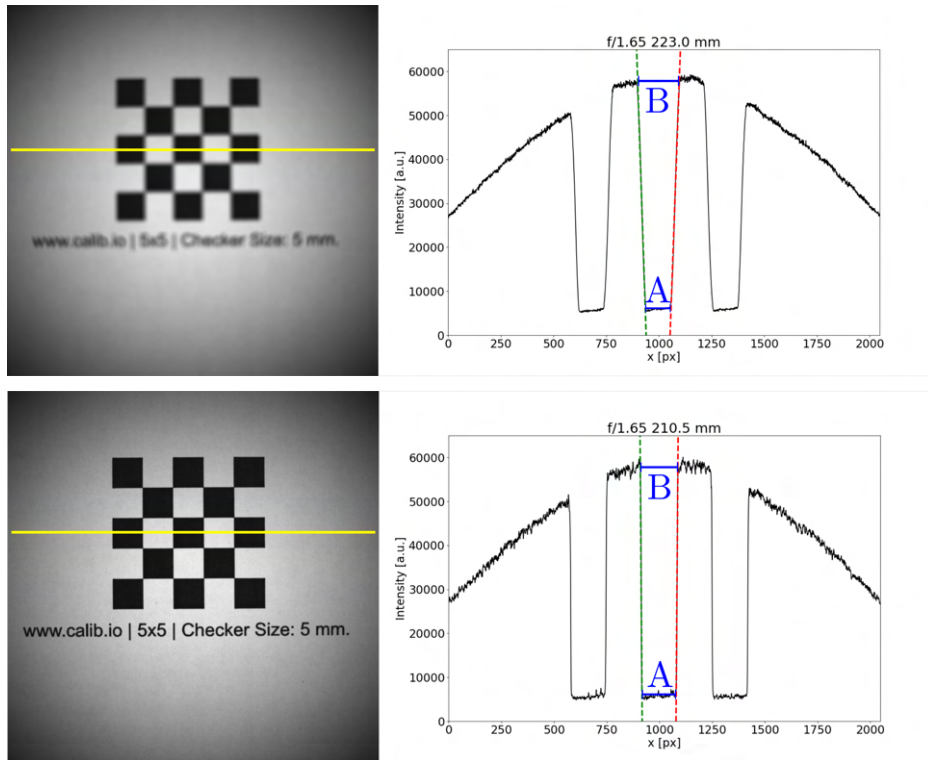
Figure 3.31.: Images captured at different distances Δd with a corresponding pro-
file plot (*at the yellow line*), fitted steepness of the intensity change
(*red, green*) and the spacings A and B (*blue*). Top: $\Delta d = 223\,mm$,
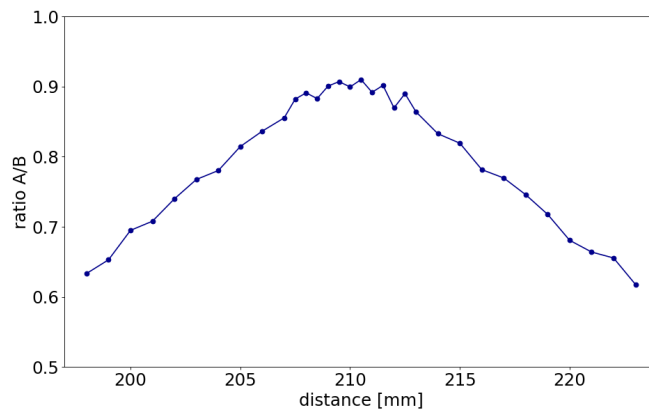bottom: $\Delta d = 210.5\,mm$.

Figure 3.32.: Ratio A/B (indicating sharpness) for different distances of the cam-
era from the checkerboard pattern.

The optimal distance $\Delta d_{opt} = 210.5\,mm$ for the camera with the given lens settings is depicted in Figure 3.32. To determine the pixel density (in $pixel/mm$), the checker size $(5\,mm)$ is compared to the distance

$$A + \frac{B - A}{2} = 162.22\,px + \frac{16.02\,px}{2} \equiv 5\,mm \rightarrow 34.05\,px \equiv 1\,mm \tag{3.5}$$

(see Figure 3.31). In theory the transition from black to white should be a step function. The fact that it is not, provided an estimation for the error in the x-direction $\Delta x_{checker} = 0,12\,mm$. This error is composed of the softness of the print and the tendency of an optical system to display a single point as a disk, a concept called *circle of confusion* or *CoC* [55]. The CoC is the only relevant part for BIF measurements. For the standard 600 dpi (dots-per-inch) laser print an error of 2 dots was assumed ($\Delta x_{print} = 2 \cdot 25,4\,mm/600 = 0,08\,mm$) [34]. According to

$$\Delta x_{checker} = \sqrt{\Delta x_{print}^2 + \Delta x_{CoC}^2}, \tag{3.6}$$

this resulted in

$$\Delta x_{CoC} = 0.09\,mm, \tag{3.7}$$

which in turn gave a depth of field (DoF) as stated by [4]

$$DoF = \frac{2 \cdot u^2 \cdot N \cdot c}{f^4 - u^2 \cdot N^2 \cdot c^2} = 13.84\,mm \tag{3.8}$$

with the distance to the object $u = 210.5\,mm - length_{lens} = 169.5\,mm$, the f-number of the lens $N = 1.65$, the focal length of the lens $f = 35\,mm$ and the diameter of the circle of confusion $c = 2 \cdot \Delta x_{CoC} = 0.18\,mm$. This showed that a focused image capture of the region, where the electron beam (with a diameter of $d_{e^-} \approx 10\,mm$) was expected, should be possible.

x_{calib}	0.03	$mm/pixel$
Δx_{CoC}	0.09	mm

Table 3.2.: The pixel density and the error in x-direction introduced by the optical system *(CoC = circle of confusion)*.

The optical vignetting seen in Figure 3.31 is caused by the geometry of the lens, the aperture size in relation to the focal length in particular. A smaller aperture size that prevents this effect reduces the photon yield by a factor of 6.5. As a result, the vignetting while using the largest aperture was deemed acceptable, but had to be kept in mind for the following measurements.

3.4.4. The Spectrometer

Preliminary measurements showed a signal at the position of the electron beam, assumed to be beam induced fluorescence (BIF) over the optical range of the EM spectrum ($400 - 700\,nm$), observed with adjacent, $50\,nm$ wide bandpass filters. Spectral analysis could potentially provide more information about the cause of the BIF. The limited space in front of the test benches viewport, confined by the solenoids and the expected low photon yield lead to the decision to build a prism spectrometer utilizing the sCMOS camera (see Chapter 3.4.3). A test setup was built up on an optical table, consisting of a lens, focusing photons (provided by an H_2 *spectral lamp*) on an adjustable slit. A cylindrical lens at its focal length was used to propagate the photons to a prism made of N-F2 flint glass, where the photons were refracted. Subsequently, these photons were collected by a camera lens and imaged on the sCMOS sensor. The footprint of that setup was modified (with an additional mirror) to fit the available space in front of the viewport at the test bench and mounted to a custom base plate. The optical components where boxed in, with all reflective surfaces blackened, to block scattered light inside the test bench's shielding (see Figure 3.33).
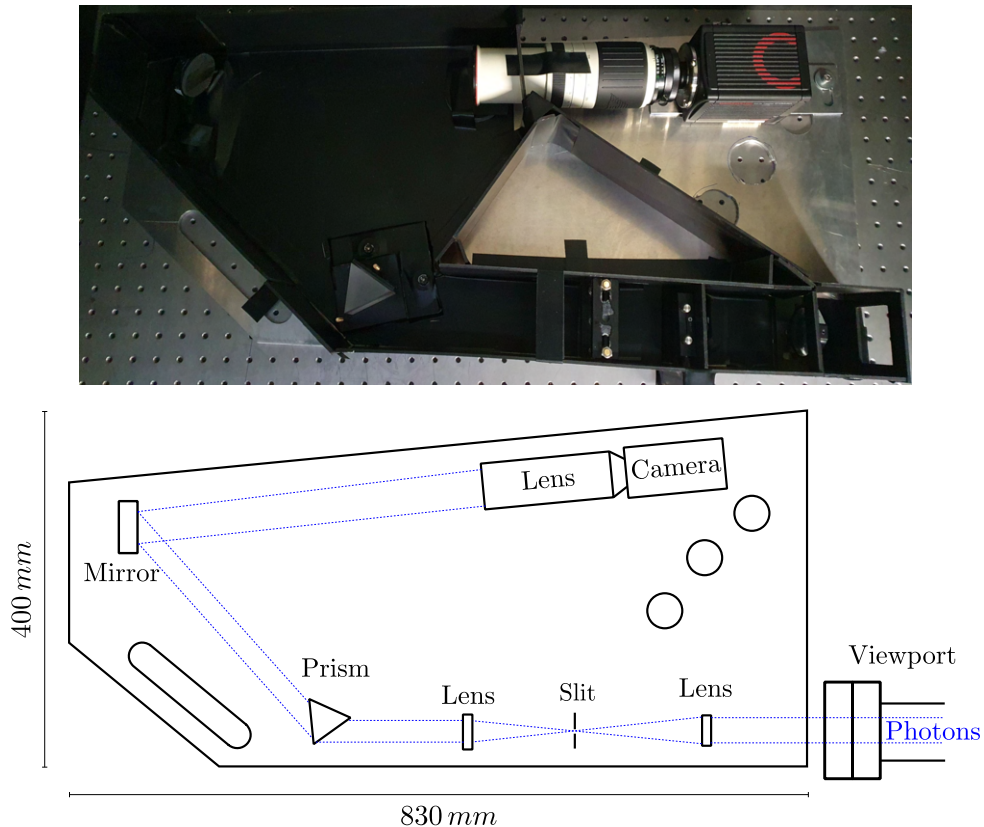

Figure 3.33.: Photo of the assembled spectrometer without its lid (*top*); schematic of the spectrometer (*bottom*).

3.4.5. Calibration of the Spectrometer

The impact position of the measured photons on the sCMOS chip is determined by the dispersion of the installed prism. The dispersion of a prism depends on its wavelength and material dependent refraction index $n(\lambda)$. The refraction index of transparent materials is described by the *Sellmeier equation*

$$n^2 = 1 + \frac{B_1 \cdot \lambda^2}{\lambda^2 - C_1} + \frac{B_2 \cdot \lambda^2}{\lambda^2 - C_2} + \frac{B_3 \cdot \lambda^2}{\lambda^2 - C_3}, \tag{3.9}$$

with experimentally determined material constants B_i, C_i. The utilized prism (equilateral, side length $l = 50\,mm$) was made from N-F2 flint glass. (see Table 3.3; [53], [59]).

	$\mathbf{B_1}$	$\mathbf{B_2}$	$\mathbf{B_3}$	$\mathbf{C_1}$	$\mathbf{C_2}$	$\mathbf{C_3}$
N-F2	1.39757	0.15920	1.26865	0.00996	0.05469	119.24835

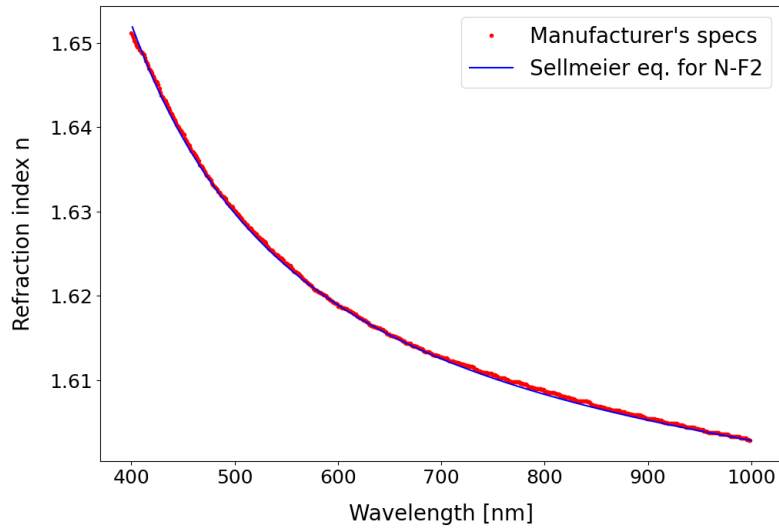**Table 3.3.:** Sellmeier constants of the utilized N-F2 flint glass prism [59].

Figure 3.34.: Refraction index $n(\lambda)$ according to the Sellmeier equation and the manufacturer's technical specifications.

Starting from snell's law of refraction

$$n_1 sin(\theta_1) = n_2 sin(\theta_2) \tag{3.10}$$

with the refraction indices in different media n_i, the angle of incidence θ_1 and the angle of refraction θ_2 in relation to the surface normal in combination with the

geometry of the equilateral prism (see Figure 3.35), the refraction angle θ_{t2} can be expressed as [30]:

$$\theta_{t2} = sin^{-1} \left[(sin\,\alpha)(n^2 - sin^2\,\theta_{i1})^{1/2} - sin\,\theta_{i1}cos\,\alpha \right]. \tag{3.11}$$

The impact position of the measured photons on the sCMOS chip of the camera Δx_{chip} with a distance d from the prism is given by

$$sin\,\theta_{t2} = \frac{\Delta x_{chip}}{d} = sin\,\alpha \cdot \sqrt{n^2 - sin^2\,\theta_{i1}} - sin\,\theta_{i1}cos\,\alpha \tag{3.12}$$
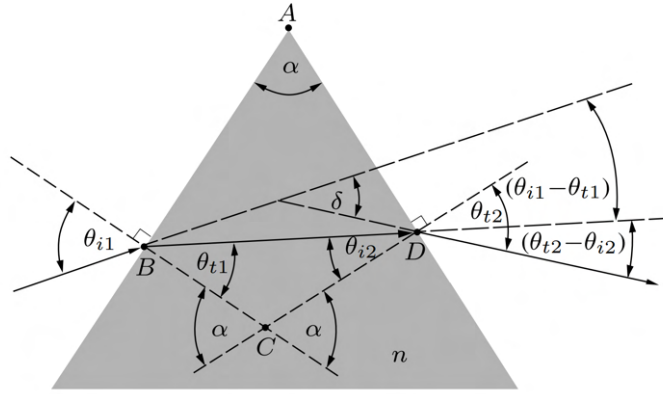

Figure 3.35.: Geometry of an equilateral prism with refraction angles taken from *E.Hecht - Optik* [30].

Using two semiconductor lasers and a H_2 spectral lamp could be used to map known wavelenghts to positions on the sCMOS chip (see Figure 3.36). The $H\alpha$ and $H\beta$ lines of the *Balmer series* and the center wavelengths of the lasers ($\lambda_{blue} = 403.8 \pm 1\,nm$, $\lambda_{red} = 639.5 \pm 1\,nm$) provided known λ values. The information about the center wavelength of the blue laser originates from the manufacturers calibration sheet, while the red one was measured with a second spectrometer. This measurement differed from the manufacturers documentation by $1\,nm$ and therefore justifies the assumed $\pm 1\,nm$ error. The spectral width of these compact semiconductor laser modules might be a result of their longitudinal multimodal operation. Equation 3.12 could then be used to define a fit function, that is able to describe the relation of the impact location of the measured photons and their wavelengths:

$$\Delta x_{fit} = k_0 - d \cdot sin\,\alpha \cdot \sqrt{n(\lambda)^2 - sin^2\,k_1} + d \cdot sin\,k_1 \cdot cos\,\alpha \tag{3.13}$$

with $\alpha = 60°$ and k_0 introduced to compensate for the reversal of the spectrum caused by the mirror in the spectrometer setup. This function was fitted to the four known wavelength values and is depicted in Figure 3.37
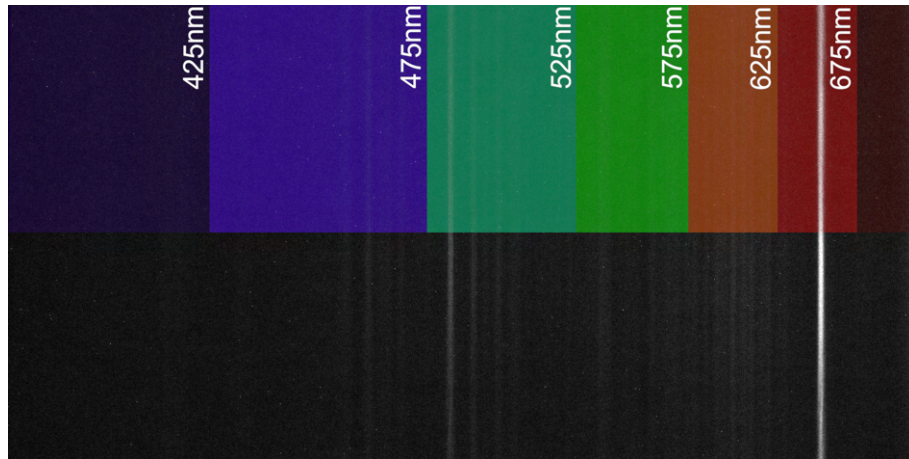
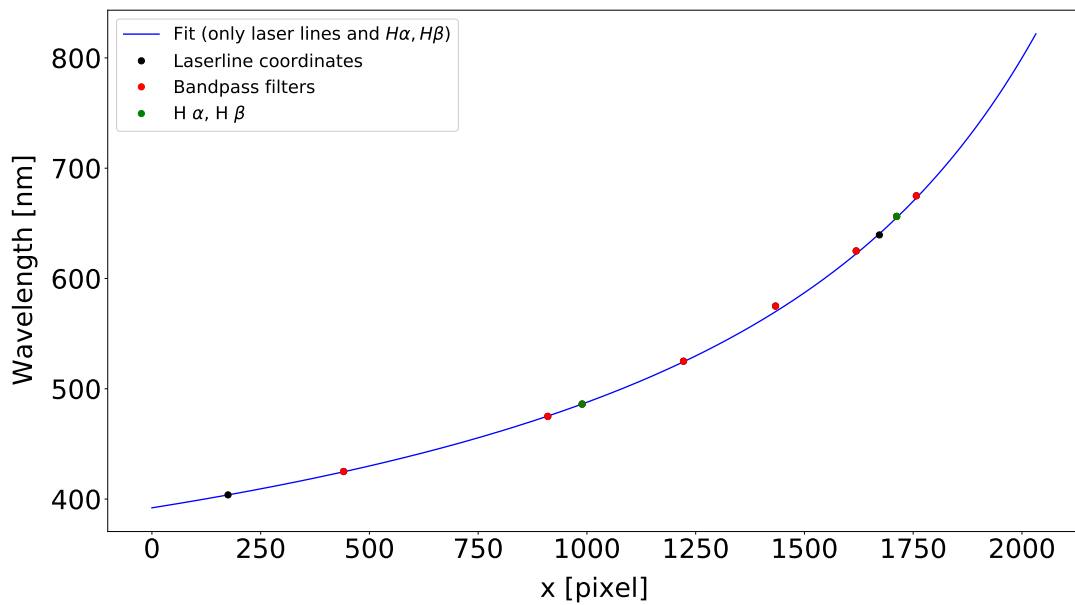**Figure 3.36.:** Measured H_2 spectrum with marked wavelength regions, obtained with the help of bandpass filters.

Figure 3.37.: Fitted calibration function with data points (with additional data, obtained with the help of bandpass filters).

k_0	k_1	d
53473.14	0.50	47230.87

Table 3.4.: Fitted values

Additional data generated by observing a continuous spectrum through a set of bandpass filters with known edges is also depicted. Although this data was deemed not suitable for the fit, because of unknown uncertainties for the edges of the filters, it seemed to fit reasonably well and was included in the reduced chi-squared (χ^2_{red}) test of the fit function. The determined $\chi^2_{red} = 1.30$ suggests adequate agreement of model and data. The residual standard error of this calibration was calculated with the same dataset to be $\Delta\lambda_{SE} = 2.10\,nm$.

3.4.6. Spectral Resolution

The spectral resolution $\Delta\lambda$ of such a device refers to its ability to distinguish spectral lines in close proximity to each other. It is related to the dispersion of the prism, as well as the width of the slit and defines the *resolving power*

$$R = \frac{\lambda}{\Delta\lambda} \tag{3.14}$$

The spectral resolution can be calculated via

$$\Delta\lambda = \left(b + \frac{f\lambda}{a}\right)\frac{\mathrm{d}\lambda}{\mathrm{d}x} \tag{3.15}$$

with the slit width b, the focal length f, the aperture a and the f-number $f/a = 4.5$ of the optics (i.e. the camera lens) and the size of one pixel on the camera sensor $\mathrm{d}x = 6.5\,\mu m$ [20]. The slit width was determined via single-slit diffraction to be $b = 250\,\mu m$. The spectral resolution can also be determined experimentally by measuring the *Full Width at Half Maximum (FWHM)* of monochromatic light [7]. At a wavelength distance of FWHM, a second wavelength can just be detected, as illustrated in Figure 3.38. The Table 3.5 shows a comparison of the results, using both methods.

$\lambda\,[nm]$	$\Delta\lambda\,[nm]$	R	$FWHM\,[nm]$	R_{FWHM}
403.8	2.7	148.9	2.1	194.1
639.5	13.6	47.0	10.1	63.4

Table 3.5.: Spectral resolution and resolving power for wavelengths of 2 laserlines 3.39.

Although there are differences in the acquired values, which might result from inaccuracies of the slit width measurement and the Gaussian fits of the laserline measurements, they portray the spectral resolution of the prism spectrometer reasonably well. The large slit width was chosen for the expected low photon yield of the BIF, resulting in a compromise with relatively low resolving power.
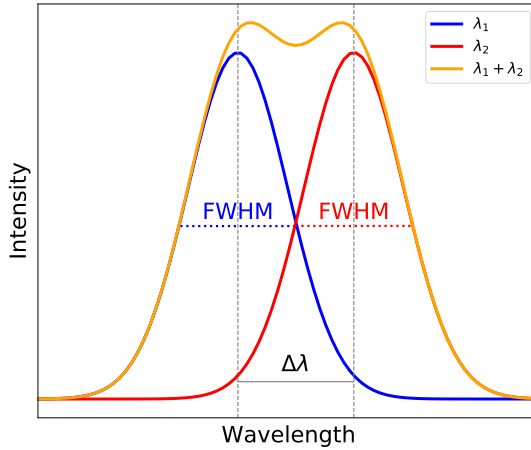
Figure 3.38.: Illustration of 2 hypothetical signals of equal intensity and different wavelengths, with $\Delta\lambda = FWHM$ and their expected resulting signal in a spectrometer.
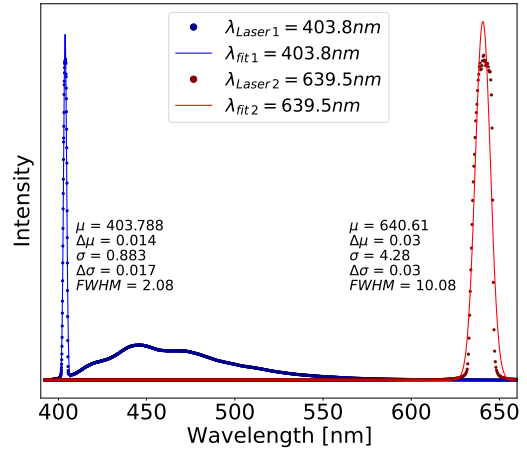
Figure 3.39.: Calibrated measurement of 2 laserlines with corresponding Gaussian fit curves.

3.4.7. Image Acquisition and Processing

Image acquisition was done with the proprietary software provided by the manufacturer of the camera, the output of which is a $16 - Bit$ TIFF (tagged image file format) grayscale image. This type of image is able to store an unlimited amount of custom metadata (or tags), including offsets, conversion factors, binning information and the temperature of the image sensor [3]. Further processing was done with the open-source software ImageJ, which was developed to process images in a scientific environment and is used in astronomy, biology, medical science and physics, among other fields [49].

4. Measurements and Analysis

4.1. Direct Observation of Beam Induced Fluorescence

Early photon detection in front of the viewport at the electron cooler test bench with the PMT setup introduced in the previous chapter, suggested the presence of *beam induced fluorescence (BIF)*. Subsequently, the low light camera was placed in front of the viewport at a distance from the beam that allowed it to be in focus, based on the previously described camera and lens setup. All following measurements presented have a background measurement subtracted in order to compensate for scattered light inside the shielding of the test bench, possible inconsistencies on the camera chip and the background caused by the heating of the cathode. These background measurements are readings taken with the electron beam switched off and the cathode still heated, recorded immediately before or after the corresponding observations for the same duration. As it turned out, a higher beam current facilitated by a source voltage of up to $-30\,kV$ was not needed for the measurements. To avoid high strain on the equipment, such as potential X-ray damage to the camera sensor, it was decided to stay close to the proven parameter $U_{oldsource} = -17\,kV$. The first measurements were taken at the bench with an acceleration voltage $U_{source} = -18\,kV$ and a beam current $I_{e-} = 550\,mA$ at a pressure of $p = 3 \cdot 10^{-10}\,mbar$. A $50\,nm$ wide bandpass filter with a *center wavelength (CWL)* of $\lambda_{CWL} = 450\,nm$ was used to illuminate the camera sensor for $t_{exposure} = 30\,s$ (see Figure 4.1).
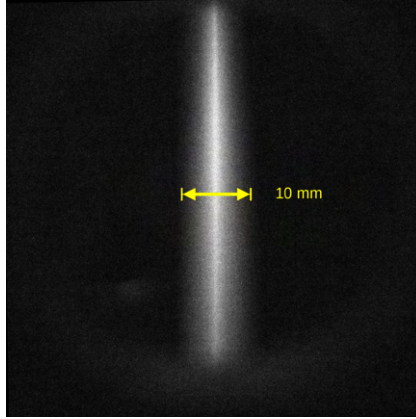

Figure 4.1.: Image of the BIF in the wavelength range $425 - 475\,nm$ with $t_{exposure} = 30\,s$. The approximate width of the signal ($10\,mm$) indicated in yellow.

This measurement produced an image of the anticipated signal at the position of the electron beam. This signal has a width of approximately $s_0 \approx 10\,mm$ and a perpendicular profile similar to a *Laplace distribution* rather than a Gaussian distributed profile, which is very prevalent for beam observations in accelerator physics (see Figure 4.3). The following profiles are averaged over 500 rows of the image, carefully extracted to avoid the influence of vignetting caused by the given camera and lens setup, described earlier. Taking the diameter of the *circle of confusion* of the optical system Δx_{CoC} into account as the error of the measurement in x-direction, the width determined in Figure 4.3 is

$$s = s_0 - \Delta x_{CoC} = 12.15\,mm - 0.09\,mm = 12.06\,mm, \qquad (4.1)$$

which is compatible with the initial width defined by the cathode's surface area and the subsequent solenoid field configuration. The error bar of the intensity distribution of Figure 4.3 Δy was evaluated as the *standard error of the mean* for the averaging process

$$\Delta y = \frac{s_y}{\sqrt{n}} = \frac{1}{\sqrt{n}} \cdot \sqrt{(\frac{\sum_{i=1}^{n}(y_i - \overline{y})^2}{n})} \qquad (4.2)$$

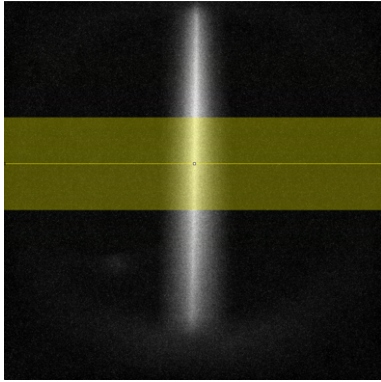with the number of rows over which the average was taken $n = 500$. In order to

Figure 4.2.: Indication of averaging region of Figure 4.1 (*yellow band*).
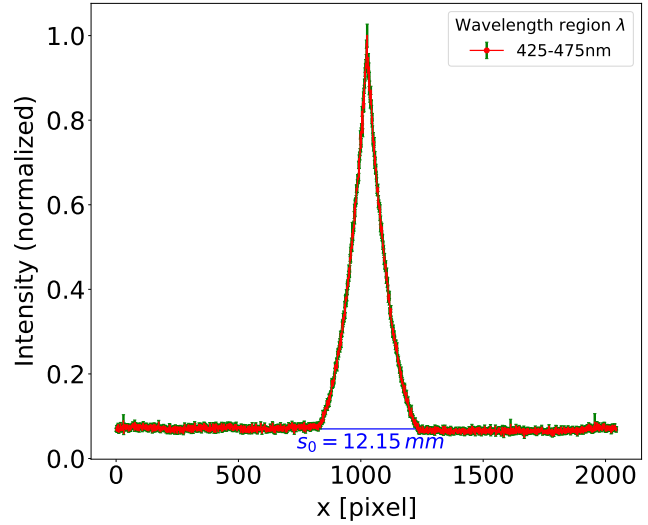

Figure 4.3.: Profile of the first BIF observation with standard errors of the mean (*green*) and the determined width.

confirm that the measured peak is not a result of systematic errors introduced by the optical setup, the approximately $10\,mm$ wide part of a H_2 spectral tube was measured with the same settings at a distance inside the optical setup's depth of field. In this area of the spectral tube the emission of a homogeneously distributed

H_2 gas column could be observed (see Figure 4.4). The photon yield was reduced to a count rate equivalent to the BIF by utilizing absorptive neutral density filters with a transmission of $T = 10^{-4}\%$. The resulting profile showed a *Gaussian-like* peak (see Figure 4.5). Therefore it could be concluded that the measured *Laplace-like* distribution of the BIF is not an effect of the optical setup.
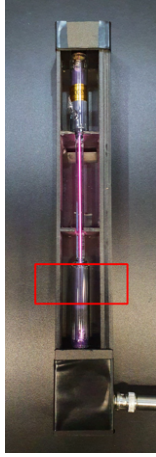

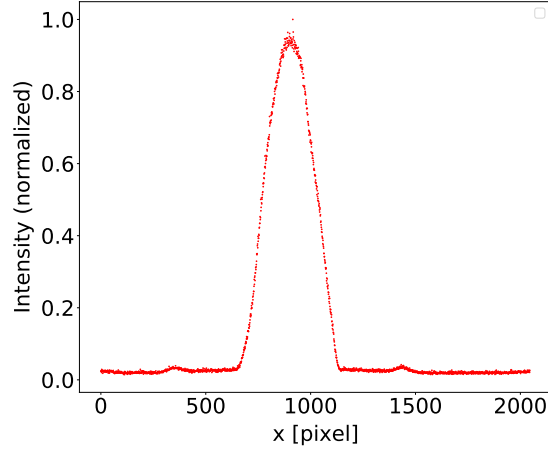**Figure 4.4.:** H_2 spectral tube with observed part indicated in red.

Figure 4.5.: Profile from the observation of the H_2 spectral tube.

4.1.1. Comparison with a Tracking Simulation

A CST particle tracking simulation was performed for the given parameters of the test bench. Looking at a slice of the simulated trajectory at the z position (i.e. the position in the direction of the electron beam) of the viewport, the simulated diameter $s_{sim} = 9.06\,mm$ is in the same order of magnitude as the measured value $s = 12.06\,mm$ (see Figure 4.6). The measured value corresponds to the x-axis of the simulated slice of the trajectories. The simulation also shows an oscillation of the beam diameter similar to Figure 3.13. This phenomenon is called *envelope scalloping* (or *galloping*) and can be explained by imperfections in the electromagnetic fields of such a device. In case of this simulation the most likely culprits are small transversal components of the longitudinal magnetic field at the transition points from one solenoid to the next [50], [15]. The largest simulated beam diameter $s_{sim2} = 11.83\,mm$ suggest a diameter that can be reached via envelope scalloping, that is even closer to the measured one (see Figure 4.7). At the test bench this effect is amplified by imperfect solenoid fields, among other things. Taking into account that the measurement integrates over many envelope oscillations, the measured value matches the simulations adequately.
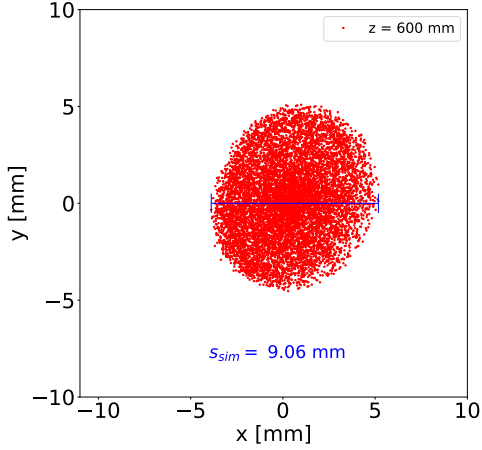
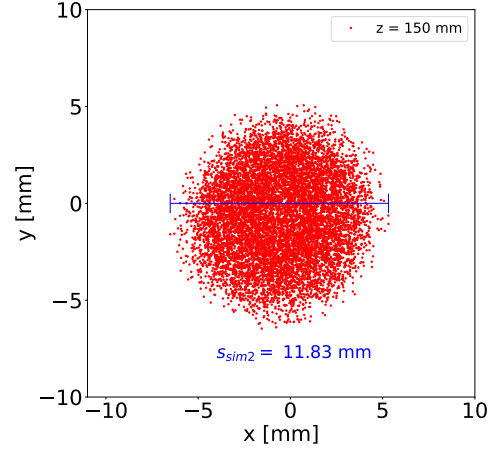**Figure 4.6.:** Top view of the simulated beam slice at $z = 600 \, mm$.

Figure 4.7.: Top view of the simulated beam slice at $z = 150 \, mm$.

4.1.2. Measurements with Bandpass Filters

To continue, the BIF was measured with a set of $50 \, nm$ wide bandpass filters that covered the visible spectrum. The signal shape is present in all wavelength regions with varying intensities (see Figure 4.8).
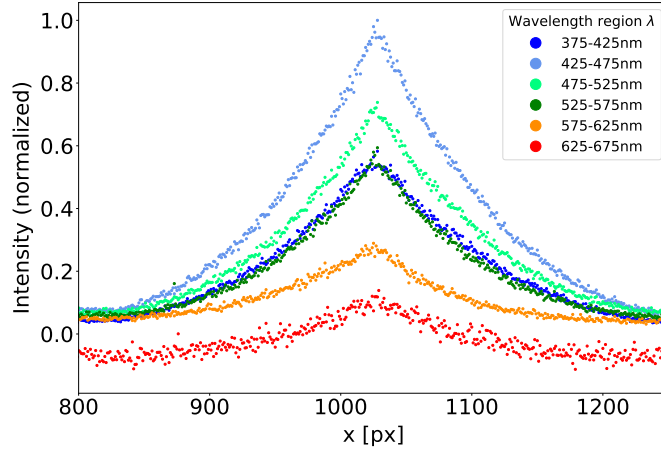

Figure 4.8.: Profiles of the measured BIF in different wavelength regions ($t_{exposure} = 30 \, s$ each).

These variances indicate the presence of a distinctive number of spectral lines with different intensities in each wavelength region, which suggests a spectral analysis of the measured photons. In the range around $\lambda = 650 \, nm$ the cooling effect of the cathode produced by the emission of electrons could be observed [22]. The background measurement, where the electron beam is switched off, recorded higher val-

ues outside the peak than the one with the electron beam. This can be illustrated, if the cathode is approximated as a black body. According to Planck's law the amount of black body radiation of this thermionic cathode ($T_{cathode} = 1373 - 1473\,K$) is significant in the spectral range of $550 - 675\,nm$ (see Figure 4.9). The spectrally resolved measurement described in Chapter 4.2 can be used to approximate a cool down of $\Delta T = 4 - 5\,K$ (see also Chapter A.2.4).
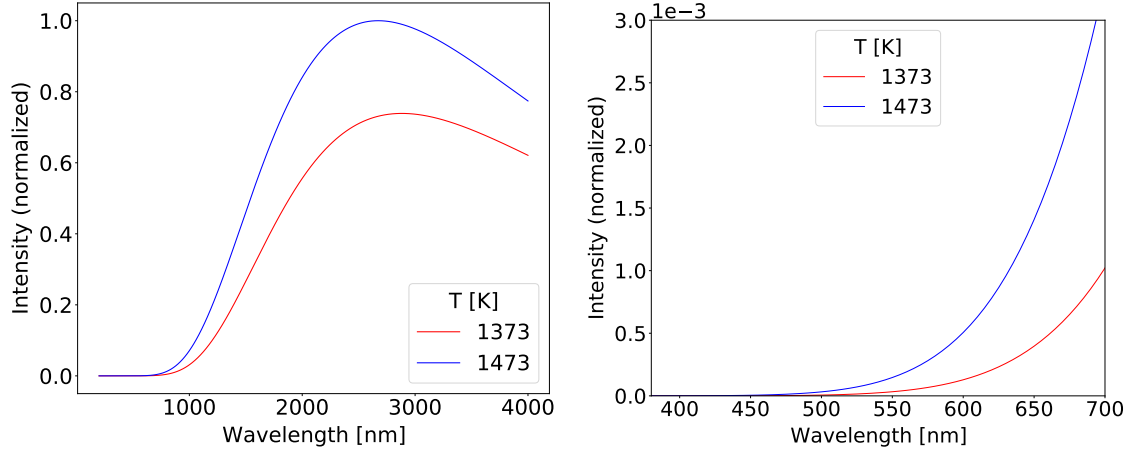

Figure 4.9.: Black body radiation of the thermionic cathode according to Planck's law; zoomed in on the visible range on the left.

This and the fact that in the two measurements of largest wavelengths, the signal-to-noise ratio was relatively low, indicated that for electron beam correlated and non-wavelength dependent measurements it would be advisable to concentrate on wavelengths between $400\,nm$ and $550\,mn$.

4.1.3. Measurements at Different Beam Currents

For the next set of measurements a bandpass filter with $\lambda = 400 - 550\,nm$ was utilized. The beam current was increased in $\Delta I_{e-} = 50\,mA$ increments up to $I_{e-} = 550\,mA$. The BIF increased for higher electron beam currents, as was to be expected (see Figure 4.10). When the profile intensities were integrated and compared, an overproportional correlation presented itself (see Figure 4.11). The BIF is therefore not only dependent on the number of electrons interacting with the residual gas. Particles in the residual gas are likely getting ionized and then trapped in the potential of the electron beam.

4.1.4. The Electromagnetic Potential of the e^--Beam as an Ion Trap

The DC electron beam of the test bench can be approximated as a homogeneous charge distribution, which explains a radial trapping effect directly. For an electron beam with an acceleration voltage $U_{source} = -18\,kV$, a beam current of $I_{e-} = $
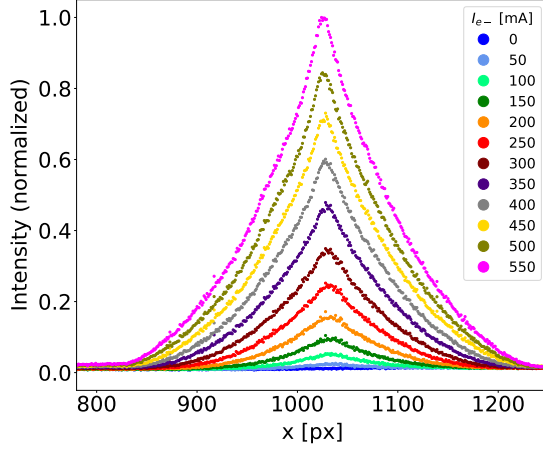
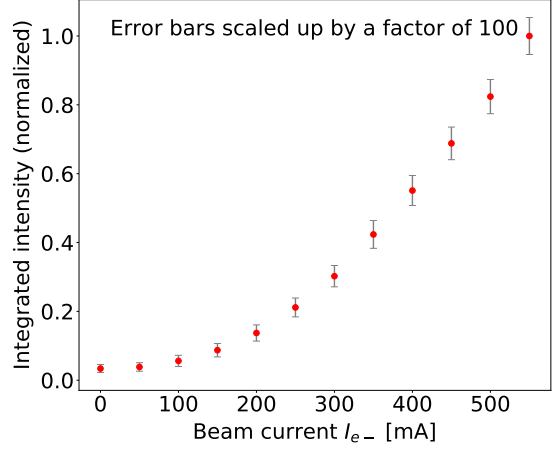**Figure 4.10.:** Profile of the BIF for different electron beam currents.

Figure 4.11.: Comparison of the total intensities via integrals over the individual profile peaks with scaled error bars (from Gaussian error propagation).

$550\,mA$ and a radius $R_{e-beam} = 6\,mm$ the charge density ρ_0 is

$$j = \frac{I_{e-}}{\pi R_{e-beam}^2} = \rho_0 \beta c \quad \rightarrow \quad \rho_0 = 6.27 \cdot 10^{-5} \frac{C}{m^3} \tag{4.3}$$

with $\beta = 0.26$ and the speed of light c. This charge density causes an electric potential Φ inside the beam pipe according to

$$\begin{aligned}
\Phi(r) &= \frac{\rho_0}{4\varepsilon_0}(R^2 - r^2) \qquad \text{for } \boxed{r \leq R} \\
\Phi(r) &= \frac{\rho_0\,R^2}{2\varepsilon_0} \ln\frac{R}{r} \qquad \text{for } \boxed{r > R}
\end{aligned} \tag{4.4}$$

with $R \equiv R_{e-beam}$ (see Appendix A.2). With the beam pipe at $r = 75\,mm$ set to lab ground, this rotationally symmetric potential is illustrated in Figure 4.12.

The longitudinal potential curve was visualized with a CST simulation, where a simplified version of the test bench's beam pipe is set to $\Phi_{beam\,pipe} = 0\,V$ and a homogeneous charge distribution represented the electron beam. The essential parts of this model for the case at hand are the two apertures (Ø20 mm) created by the anode and the deceleration optics. Both are on the same potential as the beam pipe, but much closer to the charge distribution, which leads to a shallower potential at their positions (see Figure 4.13). As a result, ions can also become longitudinally trapped in the potential of the electron beam. The possibility of longitudinal trapping in a magnetic bottle (i.e. a local minimum in the solenoid field) was investigated via simulations and showed a slight potential well ($\Delta B \approx 2\,mT$).
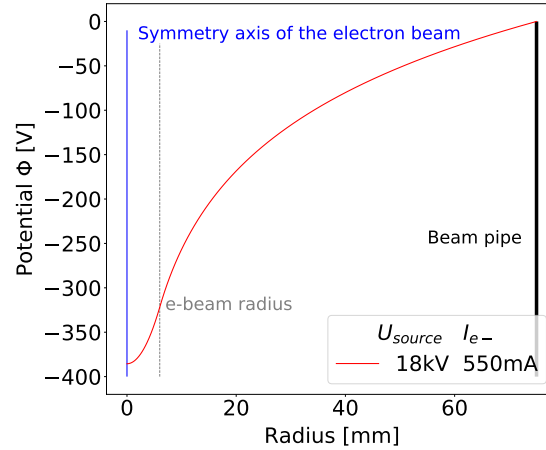
Figure 4.12.: 1-dimensional representation of the electron beam potential (with a grounded beampipe).

The solenoid field was then modified by altering the current of one solenoid, effectively removing the minimum and still allowing beam transport in the simulations. Subsequently, these modifications were tested experimentally, but did not change the photon measurements. When comparing B-field measurements taken outside of the beam pipe under both conditions with the corresponding simulated values in the region around the viewport, a small difference was observed. This finding suggests that a magnetic bottle never existed at the test bench itself. Consequently, this trapping mechanism can most likely be disregarded.
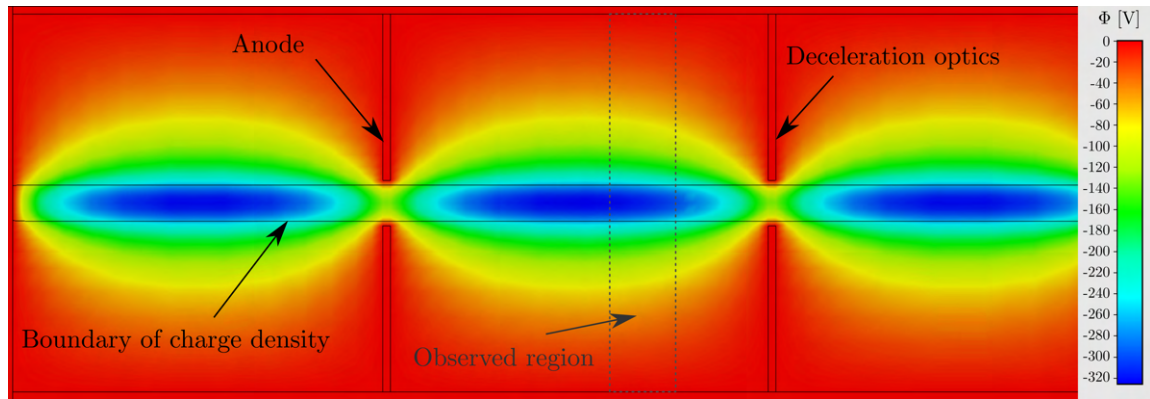
Figure 4.13.: Heat map of the CST-simulated, simplified model of the potential of a homogeneous charge distribution (on the center plane).

At this point similarities to *electron beam ion traps (EBITs)* became evident. An EBIT uses an electron beam with high charge density inside a magnetic field to trap (and further ionize) ions, comparable to the electron cooler test bench. Longitudinal trapping in EBITs is realized with drift tubes on opposing electrostatic

potentials [36]. Typical EBITs produce electron beams with much higher charge densities than the test bench with somewhat similar beam energies and currents (see Table 4.1). Over time electron beam ion traps can ionize the confined particles

	$U[kV]$	$I[mA]$	$\rho_e - [1/cm^3]$	radius$_{e-beam}[\mu m]$	p [mbar]
test bench	18	550	$3.9 \cdot 10^8$	6000	$3 \cdot 10^{-10}$
NIST EBIT	up to 33	up to 150	$4.0 \cdot 10^{12}$	30	$1 \cdot 10^{-10}$

Table 4.1.: Comparison of typical operating parameters [46].

to higher charges (so called *charge-breeding*). Depending on the different parameters of the trap an equilibrium state between the ionization and the recombination processes will be reached after seconds [18]. Because of the much lower charge density at the test bench, it is not clear to what extent and in what presumably larger time frame charge breeding occurs.

Another consequence of looking into EBITs, especially spectroscopy at them, was the fact that a background emitted from barium ions, which are constantly evaporated by the commonly used barium dispenser cathodes, is often detected [38]. When looking into the technical documentation of the thermionic barium dispenser cathode installed in the test bench, the evaporation rate could be approximated to $ER_{Ba} \approx 0.04 \frac{\mu g}{cm^2 \cdot h}$ [17]. Since the barium is continually replenished, it will not reach an equilibrium charge state for all ions, which is typically utilized for spectral measurements at an EBIT. If barium has an impact on the measurements at the test bench, they are only comparable to background observations at an EBIT.

4.1.5. Electron-Ion Interactions in an Electron Cooler

The pressure $p = 3 \cdot 10^{-10} mbar$ measured inside the beam pipe of the test bench is in the *UHV (ultra-high vacuum)* regime, meaning there was a particle density of about $\varrho \approx 10^6 \frac{1}{cm^3}$ with a mean free path of about $s_{mf} = 10^3 \, km$ [52]. The $I_{e-} = 550 \, mA$ electron beam current provides an electron flux of $N_{e/s} = 3.4 \cdot 10^{18} \frac{1}{s}$.

The dominant element of the residual gas in a baked-out UHV vessel is hydrogen [6], with a particle density of $\varrho_{H_2} = 1.39 \cdot 10^6 \frac{1}{cm^3}$, evaluated for the given pressure at the test bench. H_2 has an electron-impact ionization cross section of $\sigma_{H_2,e-i} = 0.021 \text{Å}^2$ for $E_{kin} = 18 \, keV$ electrons [48].

The number of electrons ionizing the assumed H_2 molecules in the residual gas every second, inside a volume $V_{Target} = 1.13 \, cm^3$ (determined by the beam radius $r_{e-beam} = 6 \, mm$), is given by [40]

$$- \mathrm{d}N_{e/s} = \frac{N_{Target}}{V_{Target}} \, \sigma_{H_2,e-i} \, N_{e/s} \, \mathrm{d}x \approx 1.13 \cdot 10^7 \, \frac{1}{s} \qquad (4.5)$$

which is equivalent to the number of particles, in this case H_2, ionized every second. Considering the evaporation rate of barium given earlier and assuming an escape

velocity of about $v_{Ba} = 100\frac{m}{s}$, the particle density in the volume of the electron beam could be approximated to

$$\varrho_{Ba} = \frac{ER_{Ba}}{v_{Ba} \cdot A_{e-beam}} \approx 3.39 \cdot 10^6 \, \frac{1}{cm^3} \tag{4.6}$$

The associated electron-impact ionization cross section was extrapolated from data, via an exponential fit, to be $\sigma_{Ba,e-i} = 0.106\text{Å}^2$ for $E_{kin} = 18 \, keV$ electrons [8]. The semi-empirical Lotz formula [37] is traditionally used to calculate this cross section but tends to overestimate its value [10]. The cross section for the conditions at the test bench calculated with the Lotz formula was a factor of 35 higher than the estimate above and would be reasonable in the $100 - 200 \, eV$ electron energy region, according to experimental data [8]. Nevertheless, if the estimate for the cross section is used to calculate in accordance with Equation 4.5, it comes out to

$$- \, \mathrm{d}N_{e/s} \, = \, -\frac{N_{Target}}{V_{Target}} \, \sigma_{Ba,e-i} \, N_{e/s} \, \mathrm{d}x \, \approx \, 1.31 \cdot 10^7 \, \frac{1}{s} \tag{4.7}$$

barium atoms ionized every second. This would be about 15% more than the number of ions calculated for the H_2 molecules in the residual gas. A spectral analysis might provide deeper insight into this question.
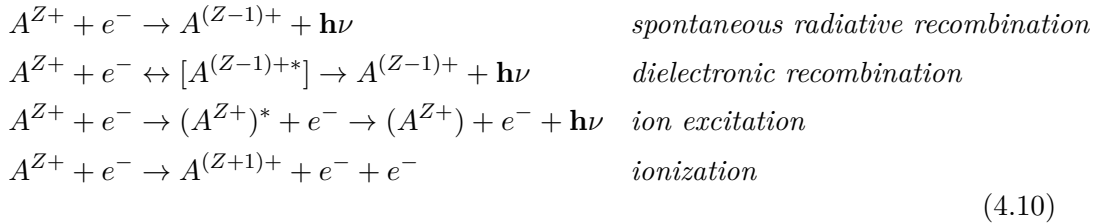
After the initial ionization of a particle in the residual gas, which is described by

$$A + e^- \rightarrow A^+ + e^- + e^- \, , \tag{4.8}$$

there are a few common electron-ion interactions besides the *repeated elastic scattering*

$$A^{Z+} + e^- \rightarrow A^{Z+} + e^- \, , \tag{4.9}$$
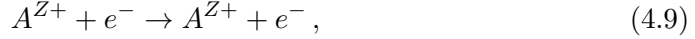
which is defined as *electron cooling* (or heating, dependent on the electron velocities in the CM frame). These are

$$
\begin{array}{ll}
A^{Z+} + e^- \rightarrow A^{(Z-1)+} + \mathbf{h}\nu & \text{\textit{spontaneous radiative recombination}} \\
A^{Z+} + e^- \leftrightarrow [A^{(Z-1)+*}] \rightarrow A^{(Z-1)+} + \mathbf{h}\nu & \text{\textit{dielectronic recombination}} \\
A^{Z+} + e^- \rightarrow (A^{Z+})^* + e^- \rightarrow (A^{Z+}) + e^- + \mathbf{h}\nu & \text{\textit{ion excitation}} \\
A^{Z+} + e^- \rightarrow A^{(Z+1)+} + e^- + e^- & \text{\textit{ionization}}
\end{array}
\tag{4.10}
$$

three of which produce photons [54]. As dielectronic recombination and spontaneous radiative recombination are most likely to occur for matched velocities of electrons and ions, the interaction anticipated to produce a majority of the photons at hand is *ion excitation*. Dielectronic recombination and spontaneous radiative recombination might occur due to secondary electrons from the ionization process. At some point an equilibrium state has to be reached, where the number of newly

ionized particles equals the number of ions that are able to escape the potential due to interactions that have been disregarded so far (e.g. scattering with energy transfer large enough to overcome the potential and/or shielding of the potential by cations). This means that an increase and subsequent plateauing of the signal might be detected, depending on the time frame. Related measurements can be found in Chapter 4.1.7.

4.1.6. The Shape of the Measured Signal

To motivate the shape of the signal, it was assumed that the ion density is much smaller than the electron density, i.e. the ions do not change the electrostatic potential of the beam, the ions do not gain momentum during the ionization and the ions do not interact with each other, the non-ionized parts of the residual gas and the magnetic field. Taking advantage of the rotational symmetry of the potential, the problem was studied 1-dimensionally. After the ions are created at one specific time t_{ion} inside the beam (and it's potential), they perform a harmonic oscillation. As a result, all ions created at t_{ion} anywhere inside the beam arrive at the lowest point of the potential ($r = 0$) at the same time. Because residual particles are ionized constantly, a large number of ions are located in the region correlated with the center of the signal. Looking at an area defined by two concentric circles
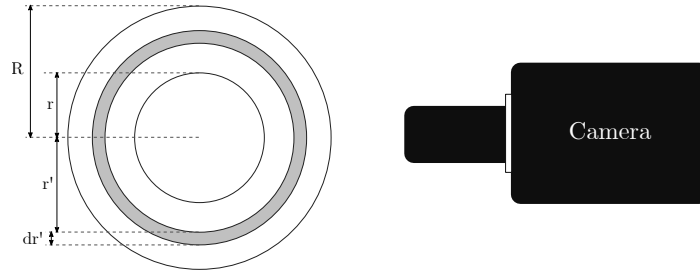

Figure 4.14.: Schematic of the electron beam related to the model considerations.

(*annulus*) (r' and $r' + \mathrm{d}r'$) inside the electron beam radius R (see Figure 4.14), the area charge density at r' is defined by

$$\sigma(r') = \frac{\mathrm{d}Q(r')}{\mathrm{d}A(r')}. \tag{4.11}$$

Therefore the change in charge at r' is

$$\mathrm{d}Q(r') = \sigma(r')\, 2\pi r'\, \mathrm{d}r'$$

$$with \quad A(r') = \int_r^R \underbrace{2\pi r' \mathrm{d}r'}_{\mathrm{d}A(r')} = \pi(R^2 - r^2). \tag{4.12}$$

This charge is accelerated by the potential, i.e. it moves to a location with radius r. The part of the charge density at r comprised of the ions created at r' is

$$\sigma(r, r') = \frac{dQ(r')}{dA(r)} = \frac{\sigma(r') \, 2\pi \, r' \, dr'}{2\pi \, r \, dr}. \tag{4.13}$$

Integrating over r provides the *area charge density* $\sigma(r)$

$$\sigma(r) = \int_r^R \sigma(r, r') \, dr = \int_r^R \frac{\sigma(r') r' \, dr'}{r}. \tag{4.14}$$

A few transformations:

$$
\begin{aligned}
r \, \sigma(r) &= \int_r^R \sigma(r') r' \, dr' & \text{differentiate } \frac{d}{dr} \\
\sigma(r) + r \, \sigma'(r) &= \underbrace{\sigma(R)}_{=0} R - \sigma(r) \, r & \text{transform} \\
\frac{\sigma'(r)}{\sigma(r)} &= -1 - \frac{1}{r} & \text{integrate } \int dr \\
\ln(\sigma(r)) &= -r - \ln(r) & \text{exponentiate}
\end{aligned}
\tag{4.15}
$$

$$\sigma(r) = e^{-r - \ln(r)} = \frac{e^{-r}}{r} \tag{4.16}$$

This model for the charge density of the ions diverges at $r = 0$, but this is also the point where the assumptions made about the ions break down. To see if it describes the observations, the derived equation could be compared to the aforementioned Laplace (or double exponential) distribution [24], which is given by

$$f_{LD}(x) = \frac{1}{2\phi} e^{-\frac{|x - \theta|}{\phi}} \tag{4.17}$$

with the location parameter θ and the scale parameter $\phi > 0$. Introduction of an amplitude parameter a, which is due to the fact that the observed signal is a projection of the ion distribution and a transition $r = \tilde{r} + \Delta r$ (with $\Delta r << r$) to avoid division by zero, lead to the fit-function

$$f_{fit} = \frac{a}{2\phi} \exp - \frac{|\tilde{r} + \Delta r + \ln(|\tilde{r} + \Delta r|) - \theta|}{\phi}. \tag{4.18}$$

This fit function describes the shape of the measurements quite well and therefore lends some credibility to the derived model (see Figure 4.15). A possible physical interpretation of the necessity of Δr in this context might be, that in the region of the peak, there is a small area with large number of ions, where this function does not describe the signal shape as a result of space charge compensation. The signal shape can be used to determine the lowest point of the electromagnetic potential of the electron beam, which corresponds to its center of charge, like a BPM is able to. During conversations with EBIT experts it was discussed that the sharp edge at the transition from signal to background most likely marks the edge of the ion trapping potential and therefore the beam itself, which would be a clear advantage compared to BPMs.
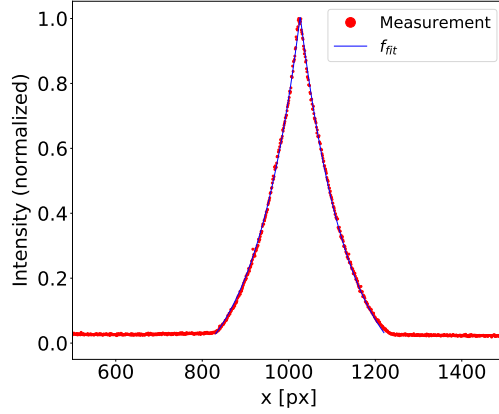
Figure 4.15.: BIF measurement with an $I_{e-} = 550\,mA$ electron beam and the derived fit function.

4.1.7. Time-Dependent Changes of the Beam Induced Fluorescence

Comparing the electron cooler test bench to an EBIT lead to an investigation of the BIF in relation to the time after the switch on of the electron beam. The relatively low charge density of the test bench in respect to an EBIT suggested charge breeding times on the scale of minutes, if charge breeding would occur at all. A $I_{e-} = 550\,mA$ electron beam was therefore switched on and a set of $t_{exposure} = 30s$ long measurements started simultaneously (see Figure 4.16). As beam operation increases the pressure over time to about $p = 3 \cdot 10^{-10}\,mbar$ mostly through electron impact and the resulting temperature increase in the (oil-cooled) collector, the measurements were normalized for said pressure. The data showed an intensity increase of the BIF, plateauing after 3-5 minutes (see Figure 4.17). Although this result seems to indicate some kind of charge breeding, it has to be noted that the vacuum gauge is installed below the cathode, i.e. the aperture of the anode might mask a time-dependent, local pressure difference existing near the viewport. The previous current-dependent measurements were acquired in a time frame that allowed for this accumulation period. Nonetheless, the overproportional relation of the BIF intensity to the beam current was verified by consecutively lowering the beam current from its maximum, after accumulation.

4.1.8. Ion Clearing through Beam Interruptions

The previously mentioned ion clearing and the corresponding influence on the BIF was investigated next. Although these measurements were prepared in accordance with the experiment at Fermilab, i.e. a pulse rate of $f = 15\,Hz$, data was taken with $f = 1\,Hz$. An electron beam with test bench settings for $I_{e-} = 550mA$ DC, was switched off for $t_{off} = 100 - 500\,ms$ and compared with the DC beam and a first beam with $f = 15\,Hz$ (see Figure 4.18). All measurements present $\Delta t_{beam} = 30\,s$ of a switched on electron beam, i.e. each measurement was extended in time to
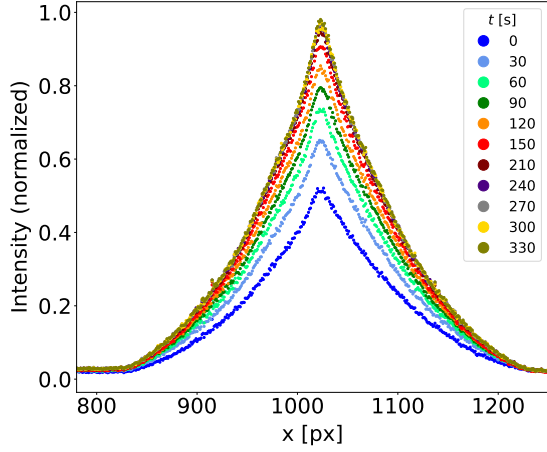
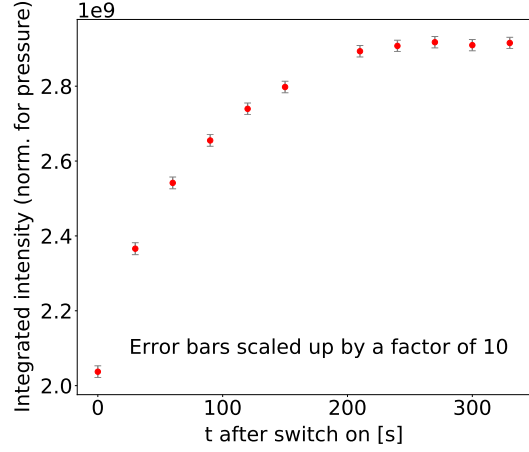**Figure 4.16.:** Profile of the BIF after switch on of the electron beam.

Figure 4.17.: Comparison of the intensities normalized for pressure via integrals over the individual profile peaks with scaled error bars (from Gaussian error propagation).

ensure comparability (e.g. the BIF of a $30\,s$ DC beam was compared to a $60\,s$ measurement of a pulsed beam that was switched off for $0.5\,s$ every second). This was utilized as a normalization for time. Before each measurement the electron beam was put into DC mode for a few minutes to account for the accumulation plateau mentioned before (see Chapter 4.1.7).

$$\Delta t_{measurement} = 30\,s \cdot (1 + f \cdot t_{off}) \tag{4.19}$$

Under the assumption that the measured photon intensity correlates directly with the number of ions, which potentially interfere with the cooling ability of such an electron beam, the goal of minimizing the measured photon intensity whilst maximizing the *duty cycle* (i.e. the percentage of time the electron beam is switched on and therefore able to cool hadrons) becomes clear. Figure 4.18 shows that it is possible to have an electron beam with a duty cycle of 97% ($f = 15\,Hz$, $t_{off} = 2\,ms$), that traps less ions than a 50% duty cycle beam ($f = 1\,Hz$, $t_{off} = 500\,ms$). If the charge and discharge time is regarded analogous to a capacitor (see Chapter 3.2) it takes about $t_{off} = 4\,ms$ to switch the electron beam off completely. For $t_{off} > 4\,ms$ Figure 4.19 shows a diminishing reduction of measured photons for a pulse frequency of $f = 15\,Hz$. It also shows that for a shut off time $t_{off} = 10\,ms$ an electron beam retains a duty cycle of 85% while reducing the measured photon and therefore most likely ions significantly.

When the electron beam is switched off, the ions are still affected by the solenoid field. They are forced onto a circular trajectory with the Larmor radius r_L and the
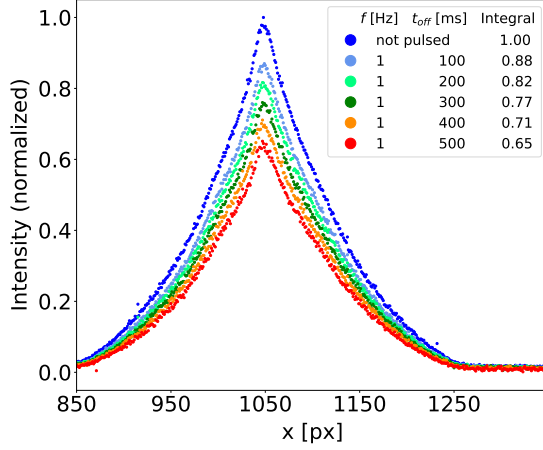
Figure 4.18.: Profile of the BIF for a pulsed electron beam ($f = 1\,Hz$) compared to a DC beam.
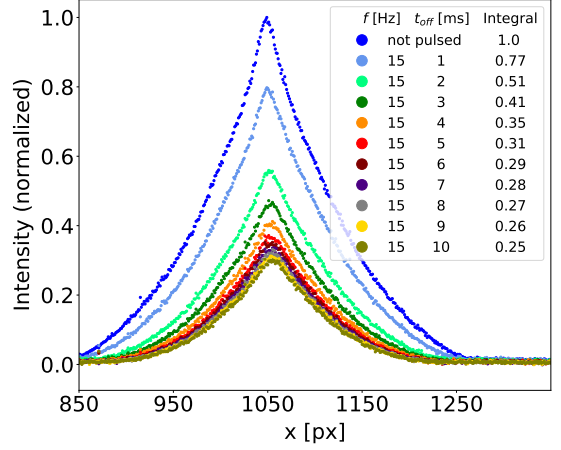
Figure 4.19.: Profile of the BIF for a pulsed electron beam ($f = 15\,Hz$) compared to a DC beam.

cyclotron frequency ω_c [40]

$$r_L = \frac{v_\perp}{\omega_c} \quad \text{and} \quad \omega_c = \frac{|q|}{m} \cdot B \tag{4.20}$$

The likely more abundant barium ions in low charge states (e.g. +1 to +6) with a kinetic energy of about $E_{kin,Ba^{z+}} \approx 10\,eV$ (e.g. from the electromagnetic potential at the location of ionization) move along a trajectory with a radius larger than the beam pipe and are consequently neutralized there, if they are not colliding with the apertures in the direction parallel to the beam path. The remaining intensity seen in Figure 4.19 is caused by newly ionized particles or far less likely by H_2^+ ions on circular trajectories with low longitudinal velocity.

Study of accumulation over a time span of minutes during pulsed operation yielded no clear results. Readings over hours showed the previously measured accumulation over about $3\,min$, but at varied plateaus with no conclusive connection to the measured pressure values at the cathode, even after interruptions of operation for up to an hour with all electromagnetic fields disabled (see Figure A.1). This leads to the conclusion that this phenomenon might at least partly be attributed to local pressure differentials near the viewport, which could not be measured with the pressure gauge located below the cathode. It was also observed in the following measurement, resulting in a smaller reduction of the photon count for $f = 15\,Hz$.

The pulse frequency was now varied in the viable region of $5 - 30\,Hz$ in $5\,Hz$ increments. The shut off times (t_{off}) $1\,ms$, $5\,ms$, $7\,ms$, $10\,ms$ were measured and can be found in detail in Figure A.10. Figure 4.20 summarizes these findings and their correlation with the duty cycle of the electron beam and the trapping of ions in its potential. It is evident that once $t_{off} = 5\,ms$ is reached, it is preferable to raise the frequency of the beam interruption to suppress ion trapping and preserve the

duty cycle of the electron beam, because the electron beam is completely switched off after $4\,ms$ and the ions can escape the region of the potential and neutralize at the wall of the beam pipe in fractions of $1\,ms$ even if they have a kinetic energy of only single digit eVs.
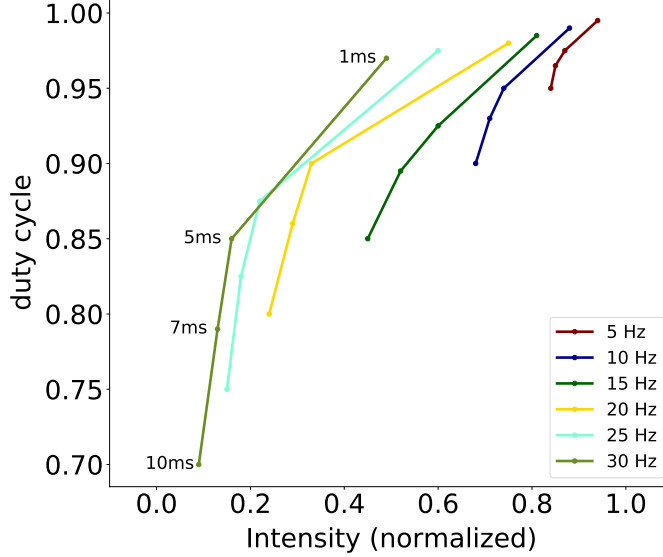

Figure 4.20.: Measurements indicating the correlation of the pulse configuration, duty cycle of the electron beam and the photon intensity; $f = [5\,Hz, 10\,Hz, 15\,Hz, 20\,Hz, 25\,Hz, 30\,Hz]$, $t_{off} = [1\,ms, 5\,ms, 7\,ms, 10\,ms]$.

4.1.9. Approximation of Photon Count

The number of photons produced should be roughly proportional to the number of trapped ions. The most likely culprit for the photon emission seemed to be the expected barium in the vacuum vessel not the hydrogen in the residual gas. The spectrally resolved measurements presented in the next chapter give no indication of the usual hydrogen lines, especially the dominant $H\alpha$ line. Should higher charge states of barium exist, the number of photons emitted by each one per unit of time might vary. The amount of detected photons in case uniform emission is assumed, depends on the area of the lens opening and the quantum efficiency of the camera chip. According to the manufacturer of the camera the number of detected photons N_γ is given by

$$N_\gamma = \frac{CF \cdot readout\,value}{QE} \tag{4.21}$$

with a conversion factor $CF = 0.48$ calibrated for each individual camera and the wavelength-dependent quantum efficiency of the sCMOS chip (see Figure A.2). A $10\,mm$ long segment of the electron beam ($U_{source} = -18\,kV$, $I_{e-} = 550\,mA$) was

observed for $t_{exposure} = 30\,s$ with the set of $50\,nm$ wide bandpass filters mentioned before (see Figure 4.22). In these regions, the quantum efficiency was averaged. The distance between the opening of the Ø$20\,mm$ lens and the electron beam was $r = 169\,mm$ (see Figure 4.21). The sphere segment covered by the camera lens was approximated by the area of the lens opening.
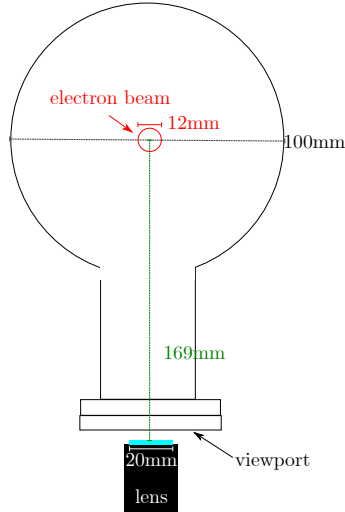

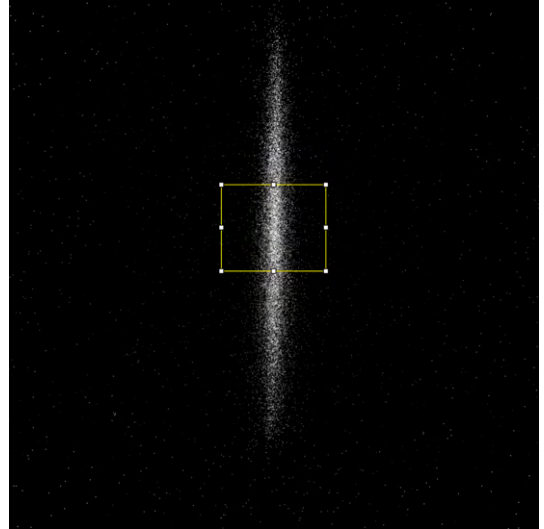**Figure 4.21.:** Top view of the observation chamber behind the viewport.

Figure 4.22.: The BIF with a $375 - 425\,nm$ bandpass filter. The observed area is highlighted by the yellow rectangle.

The total measured photon count was $N_\gamma = 2.63 \cdot 10^5\,\frac{1}{s}$ and is broken down in Table 4.2. The ratio of the lens area to the surface area of a sphere with radius r

wavelength $[nm]$	readout value	QE	$N_\gamma[1/s]$
$375 - 425$	1840413	0.40	$7.36 \cdot 10^4$
$425 - 475$	3098587	0.60	$8.26 \cdot 10^4$
$475 - 525$	2325634	0.78	$4.77 \cdot 10^4$
$525 - 575$	1756660	0.83	$3.39 \cdot 10^4$
$575 - 625$	937098	0.83	$1.81 \cdot 10^4$
$625 - 675$	339099	0.78	$6.95 \cdot 10^3$
		sum	$2.63 \cdot 10^5$

Table 4.2.: Breakdown of photon count per wavelength region.

around the observed area multiplied with the number of measured photons, taking the transmission of the viewport into account, should give an estimate for the total

amount of photons emitted in the $10\,mm$ long segment of the electron beam.

$$N_{\gamma,\,total} = \frac{A_r}{A_{lens} \cdot Tx_{viewport}} \cdot N_\gamma \approx 1.77 \cdot 10^9 \frac{1}{s} \tag{4.22}$$

with the transmission of the viewport $Tx_{viewport} = 0.85$. Under the assumption of only Ba^+ being created with the ionization rate $\frac{\partial N_{Ba+}}{\partial t} = 1.31 \cdot 10^7 \frac{1}{s}$ estimated earlier, the total number of Ba^+ ions in this $10\,mm$ segment would be $N_{Ba+} = 3.14 \cdot 10^9$ after the previously measured accumulation period of $t = 240\,s$. If every ion emits a photon due to preceding excitation or radiative recombination, every once in a while (e.g. $\Delta t = 1 - 2\,s$), the estimated amount of photons $N_{\gamma,\,total}$ would emerge.

4.2. Spectrally Resolved Measurements

Shortly after placing the spectrometer in front of the viewport between two solenoids, the importance of careful alignment became apparent. The prism was temporarily exchanged with a mirror and the adjustable slit opened to about $10\,mm$. Using a $400 - 550\,nm$ bandpass filter the whole spectrometer oriented to the signal itself. The slit width was gradually reduced while ensuring that a signal was maintained at each step. After refitting the prism, a few tests were carried out to ensure a scalable measurement protocol. The necessity for background subtraction became clear early on and forced a protocol that took a balanced cooling of the cathode through electron emission and reheating during a background measurement without an electron beam into account. A protocol like that ensures that the individual background measurements do not differ significantly from each other, which enables a combination of very long series of measurements. Another requirement was a measurement duration that allowed for the accumulation period of about $4\,min$. This could be achieved for a $I_{e-} = 550\,mA$ DC beam by an initial cool down of the cathode through $10\,min$ of beam operation, a $10\,min$ interruption and after that the start of the measurement alternating between again $10\,min$ beam operation with signal acquisition and $10\,min$ background measurement without an electron beam. This was repeated 60 times for a total measurement duration of $10\,h$. For a pulsed beam ($f = 15\,Hz$, $t_{off} = 10\,ms$) with identical test bench settings the protocol was adjusted to $12\,min$ signal and $12\,min$ background measurements, repeated 59 times, resulting in a matching duration (see Figure 4.23). After that the spectrometer was removed from the test bench to measure the slit width, needed to determine the spectral resolution as presented in Chapter 3.4.6. This time the data was averaged over 700 pixel rows, as indicated in Figure 4.24. Both data sets showed peaks at the same wavelengths, with different intensities. The heat differences of the cathode during DC operation, pulsed emission and suspended operation generated a misalignment of the intensity data. Both data sets showed negative intensities in their minimum values, because of the subtraction of a background created by a hotter cathode, which therefore emitted more heat (i.e. black body) radiation. This effect was more pronounced for data points at higher wavelengths (see Figure 4.25). To ensure better comparability of both data sets, they were realigned by subtracting a fit through data with no apparent peaks with Planck's law [40]

$$\varrho(\lambda, T) = \frac{8\pi hc}{\lambda^5} \frac{1}{\exp(\frac{hc}{\lambda k_B T}) - 1} \tag{4.23}$$

as a fit-function, with the Planck constant h, the Boltzmann constant k_B and the speed of light c (see Figures 4.26, A.3).
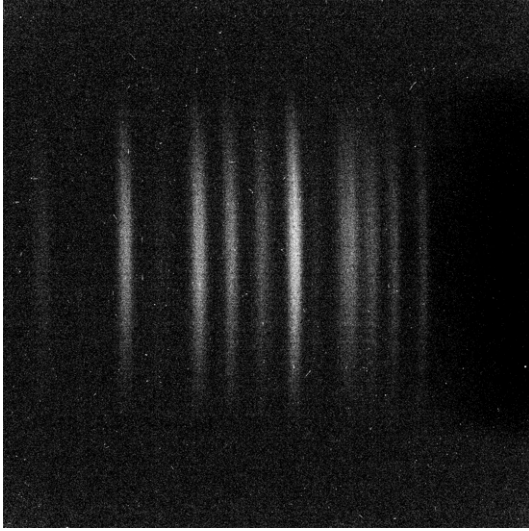
Figure 4.23.: Spectrally resolved measurement with a DC electron beam over $t = 10\,h$.
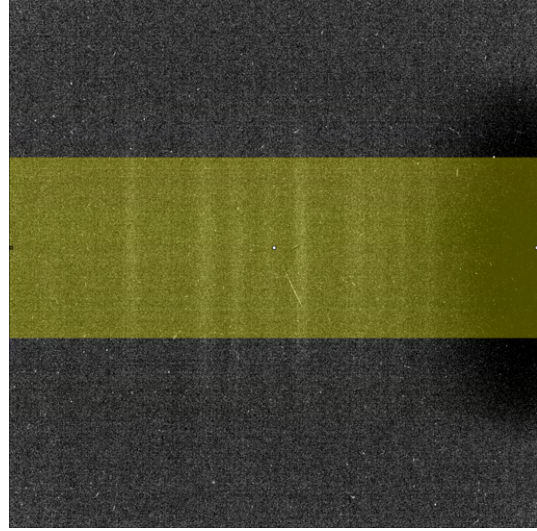

Figure 4.24.: Spectrally resolved measurement with a pulsed electron beam over $t = 10\,h$ (with the averaging region indicated in yellow).
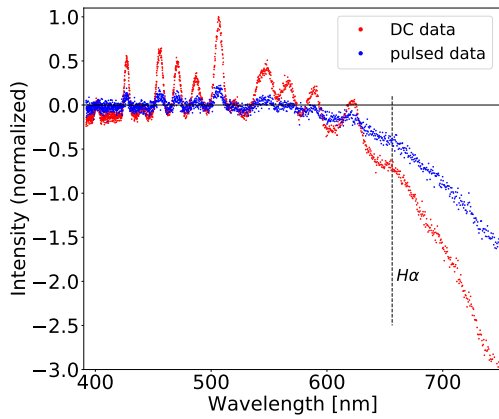

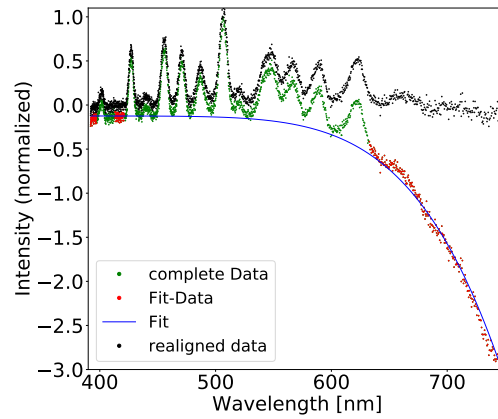**Figure 4.25.:** Data from the spectrally resolved measurements.

Figure 4.26.: Realignment of the DC data with a fit of Planck's law.

Comparing the aligned data sets showed different relations $\frac{signal_{pulsed\,beam}}{signal_{DC\,beam}}$ between peaks of specific wavelength regions (see Figure 4.29. This suggests that the larger this relation is, the faster the processes that create the corresponding peak are. This could be due to different excitations or charge states of barium or even different ions. Although the presence of hydrogen is inevitable in a baked-out UHV vessel [6], it contributed with its strongest line $H_\alpha = 656\,nm$ in trace amounts at most. All measured peaks could be attributed to spectral lines of barium, if intensity and

charge states were not taken into account (and a charge state up to Ba^{35+} was used). The same is true for argon, which occurs with a partial pressure hundreds of times lower than hydrogen in such a vessel [45], [58], [35], [26]. At this time, the presence of different ions in varying states during operation of the electron beam has been confirmed for the electron cooler test bench, and this is likely to be the case in similar devices. However, further determination of the exact composition of the ions is currently not possible.

4.3. Final Measurements

After completing the spectral measurements the HV capabilities of the upgraded electron source underwent a final test. The initial parameters derived from simulations at *TSL*, namely $U_{source} = -26\,kV$, $U_{PE} = -0.38\,kV$ and $I_{e-} = 1\,A$ could be confirmed [62]. Furthermore, a $I_{e-} = 1\,A$ electron beam with an accelerating voltage of $U_{source} = -30\,kV$ was shown (see Figure 4.27). The corresponding profiles are depicted in Figure 4.28. For higher beam currents, additional optimizations have to be made at the test bench.
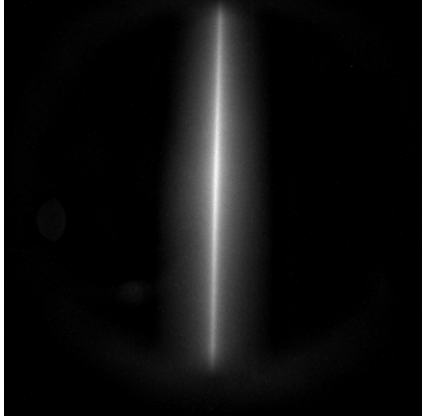

Figure 4.27.: Image of the BIF with a $U_{source} = -30\,kV$, $I_{e-} = 1\,A$ electron beam ($\lambda = 400 - 550\,nm$, $t_{exposure} = 30\,s$).
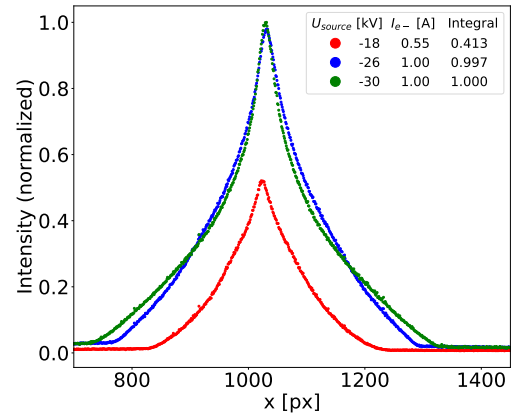

Figure 4.28.: Measured profiles for 3 different sets of operating parameters at the test bench.
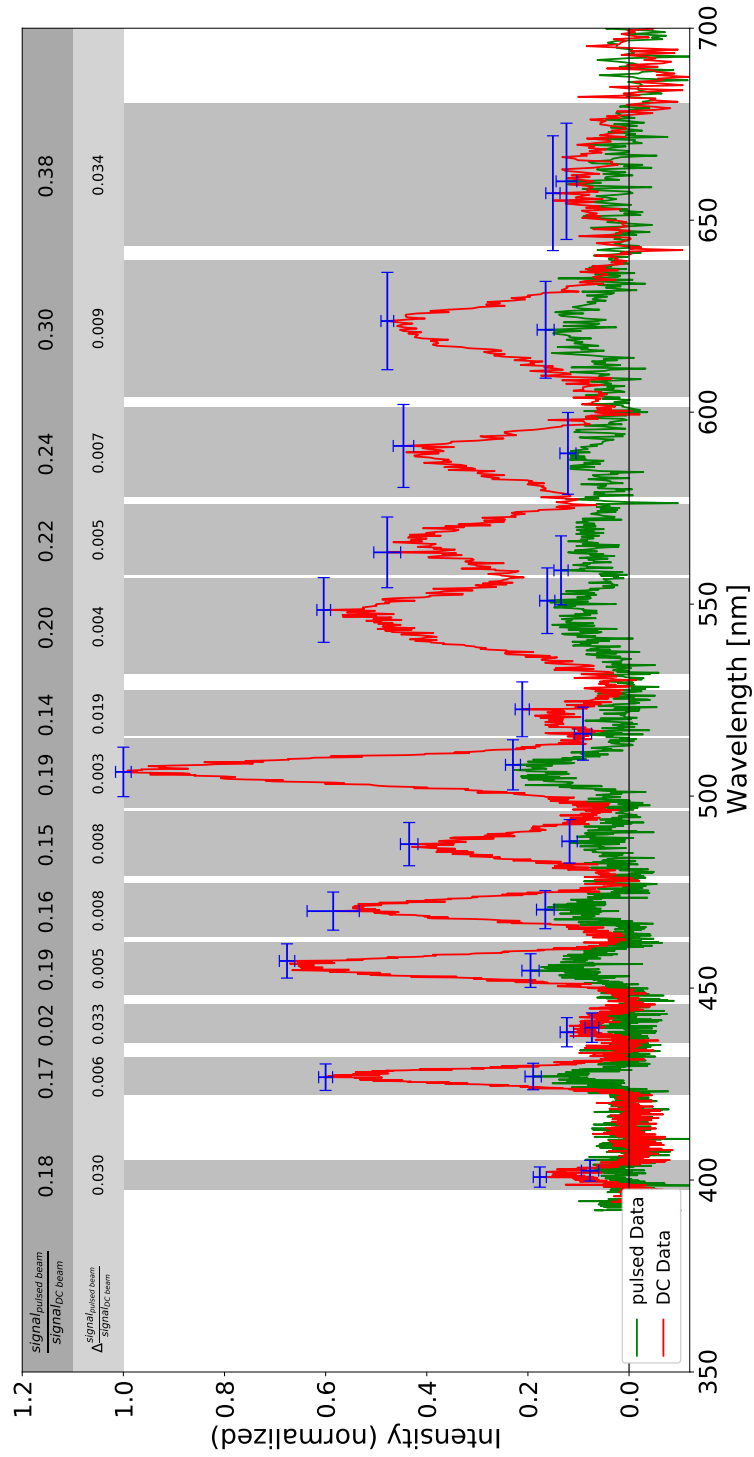
Figure 4.29.: Both aligned data sets with their relation and corresponding uncertainty in each interval. The error bars mark the largest intensity per interval and provide information about the standard error of the mean in y-direction and the spectral resolution in x-direction.

5. Conclusion and Outlook

This thesis presents a comprehensive study of beam induced fluorescence (BIF) in an ultra-high vacuum (UHV) environment with an electron beam in the Ampere regime. In the course of this study a new iteration of imaging technology, namely scientific CMOS sensors, and its ability to measure low light phenomena in an accelerator context, was demonstrated. The BIF is a result of electron-ion interactions commonly found in electron coolers. Residual gas particles are ionized by the electrons and mostly stay trapped inside the electromagnetic potential of the beam. While a radial confinement of ions in the rotationally symmetric potential of the electron beam is obvious, a longitudinal trapping mechanism, solely dependent on apertures in the beam pipe and their resulting potential gradients, could be illustrated. These trapping mechanisms are relevant even for actual electron coolers with beams steered via toroidal magnets, as these influence the beam's potential only slightly.

The shape of the BIF signal, which is directly correlated to the distribution of the confined ions, indicates the lowest point of the potential and therefore the electron beam's center of charge, which is commonly measured by a beam position monitor (BPM). Compared to a BPM, the measurement of the BIF signal also implies the boundary of the beam at the sharp edge, were the signal transitions into the uniform background.

The feasibility of ion clearing through electron beam interruptions (or pulsing) whilst retaining a high duty cycle and corresponding cooling force was demonstrated. Studying parallels to electron beam ion traps revealed the possible presence of a significant particle density of barium, other than the hydrogen expected in a baked-out UHV beam pipe. Spectrally resolved measurements reinforce that assumption, proving the culprit of the BIF not to be the suspected hydrogen. These insights could potentially have positive influences on the generation and diagnostics of future electron cooler beams.

In addition, during the relocation of the test bench to start the BIF measurements, the cathode's tendency to ignite Penning discharges for EM field configurations allowing accelerating voltages higher than $U_{source} = -17\,kV$ (and therefore facilitating higher beam currents), was investigated. Large elements of the cathode, including the Pierce electrode, were redesigned (in part inspired by *M.W. Bruker* [12]), manufactured in-house and tested. Further simulations and adjustments of the EM field helped to avoid the trapping of ionized residual gas particles in local minima of the electrostatic potential along solenoid field lines and therefore increased the robustness against Penning discharges, allowing $U_{source} = -30\,kV$. A $I_{e-} = 1\,A$ electron beam was produced with that voltage.

5. Conclusion and Outlook

Future experiments at the test bench might include a controlled inlet of a known gas like argon and observations of the subsequent changes to the spectrum of the BIF. A pressure gauge could be fitted next to the observation chamber to study possible correlations to the accumulation period. Mass spectrometry could be implemented at the test bench to identify the measured spectral lines. Even the cathode material could be changed to the slightly less common lanthanum hexaboride to detect alterations in the BIF spectrum. Another approach to modify the observed spectrum might be by ejecting ions from the trap selectively, utilizing their resonance frequencies.
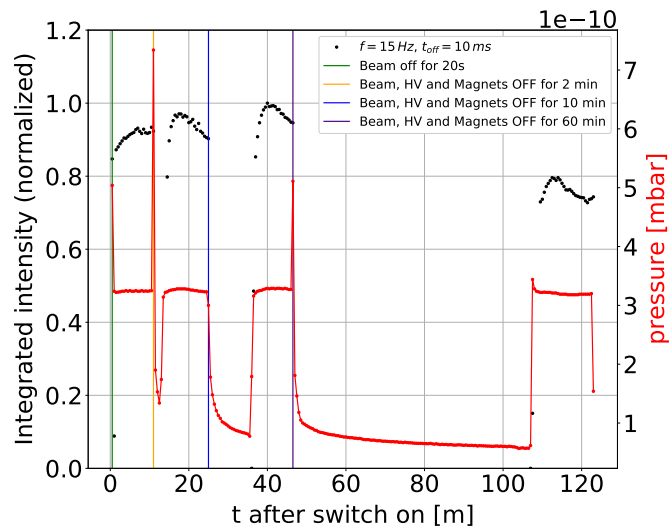
A. Appendix

A.1. Additional Figures

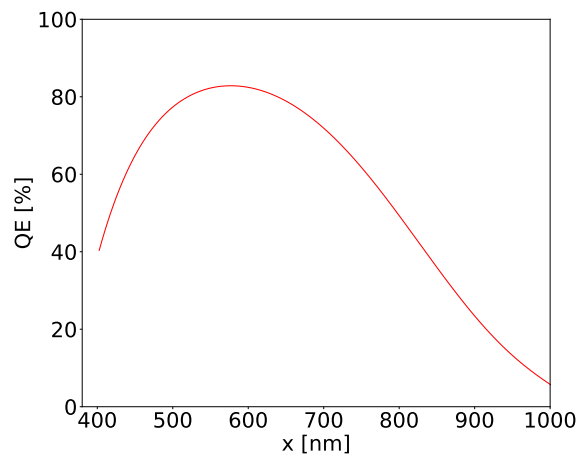**Figure A.1.:** Accumulation of photo intensity with a pulsed electron beam.

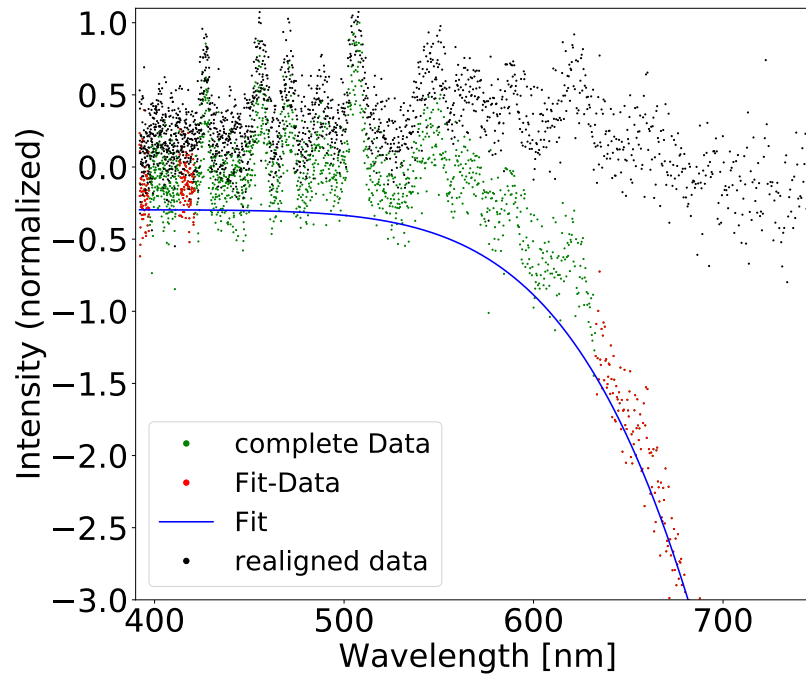**Figure A.2.:** Typical quantum efficieny of the utilized sCMOS camera according to the manufacturer [28].

Figure A.3.: Realignment of the pulsed data with a fit of Planck's law.

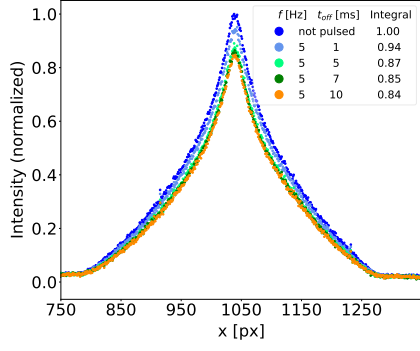**Figure A.4.:** $f = 5\,Hz$, $t_{off} = [1ms, 5ms, 7ms, 10ms]$.
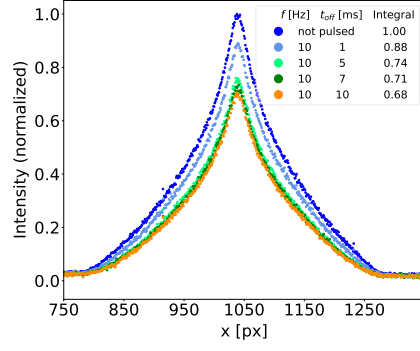
Figure A.5.: $f = 10\,Hz$, $t_{off} = [1ms, 5ms, 7ms, 10ms]$.
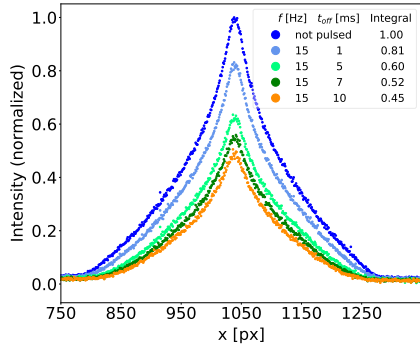
Figure A.6.: $f = 15\,Hz$, $t_{off} = [1ms, 5ms, 7ms, 10ms]$.
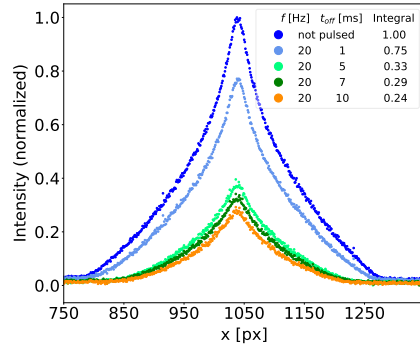
Figure A.7.: $f = 20\,Hz$, $t_{off} = [1ms, 5ms, 7ms, 10ms]$.
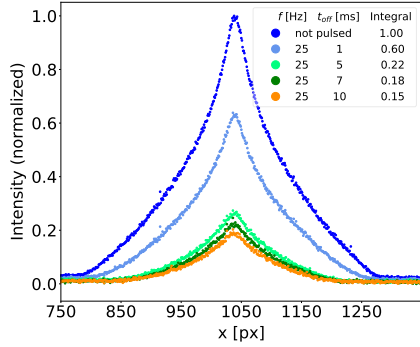
Figure A.8.: $f = 25\,Hz$, $t_{off} = [1ms, 5ms, 7ms, 10ms]$.
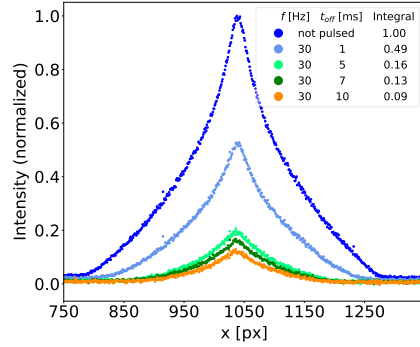
Figure A.9.: $f = 30\,Hz$, $t_{off} = [1ms, 5ms, 7ms, 10ms]$.

Figure A.10.: Measurements of the photon signal for $\Delta t_{beam} = 30\,s$ with a background subtracted.

A.2. Additional Material

A.2.1. E-Field of a Homogeneously Charged, Long Cylinder

(length L, radius R)

Divergence theorem or Gauss's theorem

$V \subset \mathbb{R}^n$ is compact and has a piecewise smooth boundary $S = \partial V$. $\widehat{n}$ is a unit normal on S.

$$\int_V (\nabla \cdot \vec{E}) \, d^n V = \oint_S \vec{E} \cdot \widehat{n} \quad d^{n-1} S \tag{A.1}$$

here:

$$\underbrace{\int_V (\nabla \cdot \vec{E}) \, d\vec{v}}_{\text{I.}} = \underbrace{\oint_A \vec{E} \cdot d\vec{a}}_{\text{II.}} \tag{A.2}$$

I. 1. Maxwell's equation (Gauss's law)

$$\nabla \cdot \vec{E} = \frac{\rho}{\varepsilon_0} \qquad \text{with} \quad \rho = \frac{charge}{volume} = chargedensity \tag{A.3}$$

here: homogeneously charged cylinder, i.e. $\rho(r) = \begin{cases} \rho_0 & \text{für } r \le R \\ 0 & \text{für } r > R \end{cases}$, $\int_V d\vec{v}$ volume, $\oint_A d\vec{a}$ area

Geometric transformation: *Cartesian coordinate system $\rightarrow$ Cylindrical coordinate system*

$$\vec{x} = \begin{pmatrix} x \\ y \\ z \end{pmatrix} = \begin{pmatrix} r \cos \varphi \\ r \sin \varphi \\ z \end{pmatrix} \tag{A.4}$$

Jacobian determinant

$$\det \frac{(\partial x, \partial y, \partial z)}{(\partial r, \partial \varphi, \partial z)} = \left| \frac{\partial \vec{x}}{\partial r} \quad \frac{\partial \vec{x}}{\partial \varphi} \quad \frac{\partial \vec{x}}{\partial z} \right| = \begin{vmatrix} \cos \varphi & -r \sin \varphi & 0 \\ \sin \varphi & r \cos \varphi & 0 \\ 0 & 0 & 1 \end{vmatrix} = r(\sin^2 \varphi + \cos^2 \varphi) = r \tag{A.5}$$

Transformation:

$$\int_x \int_y \int_z dx dy dz \rightarrow \int_0^r \int_0^{2\pi} \int_0^z r' dr' d\varphi dz' \tag{A.6}$$

for $\boxed{r \le R}$:

$$\mathbf{I.} = \frac{1}{\varepsilon_0} \int_0^r \rho(r') \, r' dr' \int_0^{2\pi} d\varphi \int_0^L dz' = \frac{\rho_0}{\varepsilon_0} \int_0^r r' dr' \int_0^{2\pi} d\varphi \int_0^L dz' = \frac{\rho_0}{\varepsilon_0} r^2 \pi L \tag{A.7}$$

for $\boxed{r > R}$:

$$\mathbf{I.} = \frac{1}{\varepsilon_0} 2\pi L \int\limits_0^r \rho(r')\, r'dr' = \frac{1}{\varepsilon_0} 2\pi L \left(\int\limits_0^R \rho_0\, r'dr' + \int\limits_R^r 0 \cdot r'dr' \right) = \frac{\rho_0}{\varepsilon_0} R^2 \pi L \quad (A.8)$$

II. Line integral over the area of the cylinder

$$d\vec{a} = d\vec{a}_{top} + d\vec{a}_{bottom} + d\vec{a}_{sheath} \quad (A.9)$$

here: $d\vec{a}_{top} = -d\vec{a}_{bottom}$, because their unit normals are anti-parallel.

$$\oint\limits_A \vec{E} \cdot d\vec{a}_{sheath} = \int\limits_0^r \int\limits_0^{2\pi} \int\limits_0^L E\, dr'd\varphi dz = E\, r\, 2\pi L \quad (A.10)$$

for $\boxed{r \le R}$:

$$E(r) = \frac{\rho_0}{2\varepsilon_0} r \quad (A.11)$$

for $\boxed{r > R}$:

$$E(r) = \frac{\rho_0}{2\varepsilon_0} \frac{R^2}{r} \quad (A.12)$$

A.2.2. Potential of the Electron Beam

$$\vec{E} = -\nabla\Phi \quad (A.13)$$

$$\Phi = -\frac{\rho_0}{4\varepsilon_0} r^2 + \Phi_0 \qquad \text{for } r \le R \quad (A.14)$$

$$\Phi = -\frac{\rho_0\, R^2}{2\varepsilon_0} \ln r + \Phi_1 \qquad \text{for } r > R \quad (A.15)$$

Derivation of the constants: $\Phi(r = R) := 0 \quad \rightarrow \quad \Phi_0 = \frac{\rho_0}{4\varepsilon_0} R^2 \; ; \; \Phi_1 = \frac{\rho_0\, R^2}{2\varepsilon_0} \ln R$

for $\boxed{r \le R}$:

$$\Phi = \frac{\rho_0}{4\varepsilon_0} (R^2 - r^2) \quad (A.16)$$

for $\boxed{r > R}$:

$$\Phi = \frac{\rho_0\, R^2}{2\varepsilon_0} \ln\frac{R}{r} \quad (A.17)$$

A. Appendix

A.2.3. Space Charge Density of the Electron Beam

The space charge density ρ_0 can be determined with the known values E_{kin}, I_{e-}, $m_{0,e-}$ and the beam radius R via the current density j.

$$j = \frac{I}{A} = \frac{1}{A} \cdot \frac{dQ}{dt} = \frac{1}{A} \cdot \frac{dQ}{dV} \cdot \frac{dV}{dt} = \frac{1}{A} \cdot \rho_0 \cdot \frac{Adx}{dt} = \rho_0 \cdot v = \rho_0 \cdot \beta \cdot c \qquad (A.18)$$

with $A = \pi R^2$. From

$$E_{kin} = (\gamma - 1)\, m_{0,e-}\, c^2 \qquad (A.19)$$

with $\gamma = \frac{1}{\sqrt{1-\beta^2}}$ and

$$\beta = \sqrt{1 - \left(\frac{E_{kin}}{m_{0,e-}\, c^2} + 1 \right)^{-2}} \qquad (A.20)$$

results in

$$\rho_0 = \frac{I}{\pi R^2 \cdot \beta \cdot c} \qquad (A.21)$$

A.2.4. Planck's Law Fit of Measured Spectra

Figures 4.26 and A.3 show the measured spectra for DC and pulsed operation respectively with a background, where the cathode is at a slightly higher temperature, subtracted. This results in the previously mentioned fit function $f(\lambda, T)$ (see Chapter 4.2) consisting of the difference of two radiant emittances as follows:

$$f(\lambda, T) = Q \cdot \frac{2hc^2}{\lambda^5} \cdot \left(\frac{1}{\exp(\frac{hc}{\lambda k_B T}) - 1} - \frac{1}{\exp(\frac{hc}{\lambda k_B (T+dT)}) - 1} \right) + y0 \qquad (A.22)$$

The constant Q is a result of the transmission of the optical elements and the QE of the camera chip, while the constant y_0 is most likely due to the fact that the cathode can only be approximated as a black body. Both are determined by the fitting algorithm. The values for T and dT are listed in Table A.1. The determined

	$T[K]$	$dT[K]$
DC	1202	3.8
pulsed	1288	4.8

Table A.1.: The pixel density and the error in x-direction introduced by the optical system *(CoC = circle of confusion).*

temperature values fit the cathode manufacturers listed values $(1373 - 1473\,K)$ for the given heating power $(\approx 20\,W)$ reasonably well, which is why the corresponding temperature difference dT lead to the assumption of a $\Delta T = 4 - 5\,K$ cool down of the cathode during operation (i.e. electron emission).

A.2.5. Details about the Electron Source Upgrade

The upgraded version of the electron source (see Figure A.11) reuses the holder for the cathode with its electrically insulated connection for the cathode's heating power, the Pierce electrode insulator, the cathode, the inner of the Pierce electrode close to the emitting surface of the cathode and the anode. The main $32\,kV$ insulator was designed, produced and soldered to copper and stainless steel rings by an external company. This part was welded to CF160 (or ConFlat 160) flanges by the KPH mechanical workshop, which manufactured all other newly utilized parts. Some flanges were outfitted with CF16 access holes for the heating power and the Pierce electrode power supply. The existing anode was attached electrically insulated, to enable possible future current measurements of electrons hitting it (see Figure A.12). The most important part of the upgrade, the (outer shell of the) Pierce electrode, was fabricated out of stainless steel and polished to a mirror shine to minimize field emissions on its surface. It consists of 2 parts to allow assembly on the corresponding insulator (see Figures A.13, A.14, A.15, A.16). To connect the Pierce electrode to its power supply, a threaded hole was drilled into its lower part.
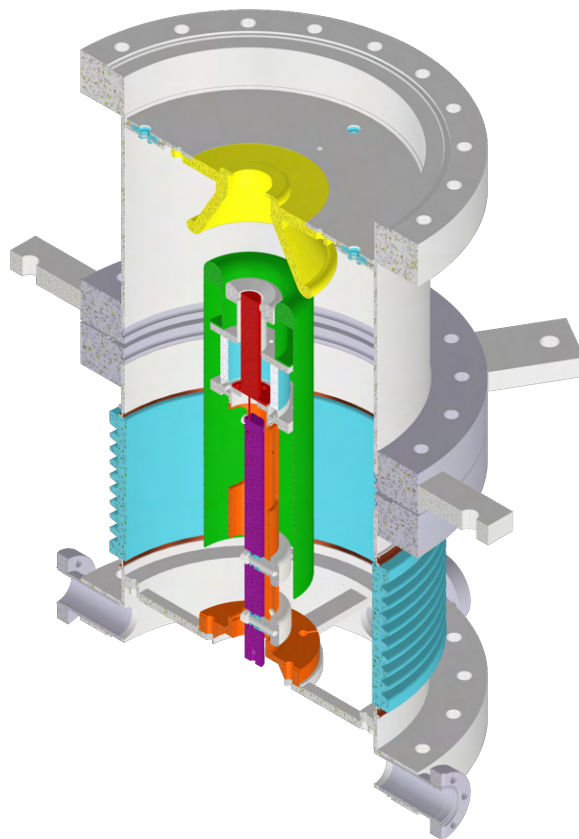

Figure A.11.: Half section 3D view of the upgraded electron source.

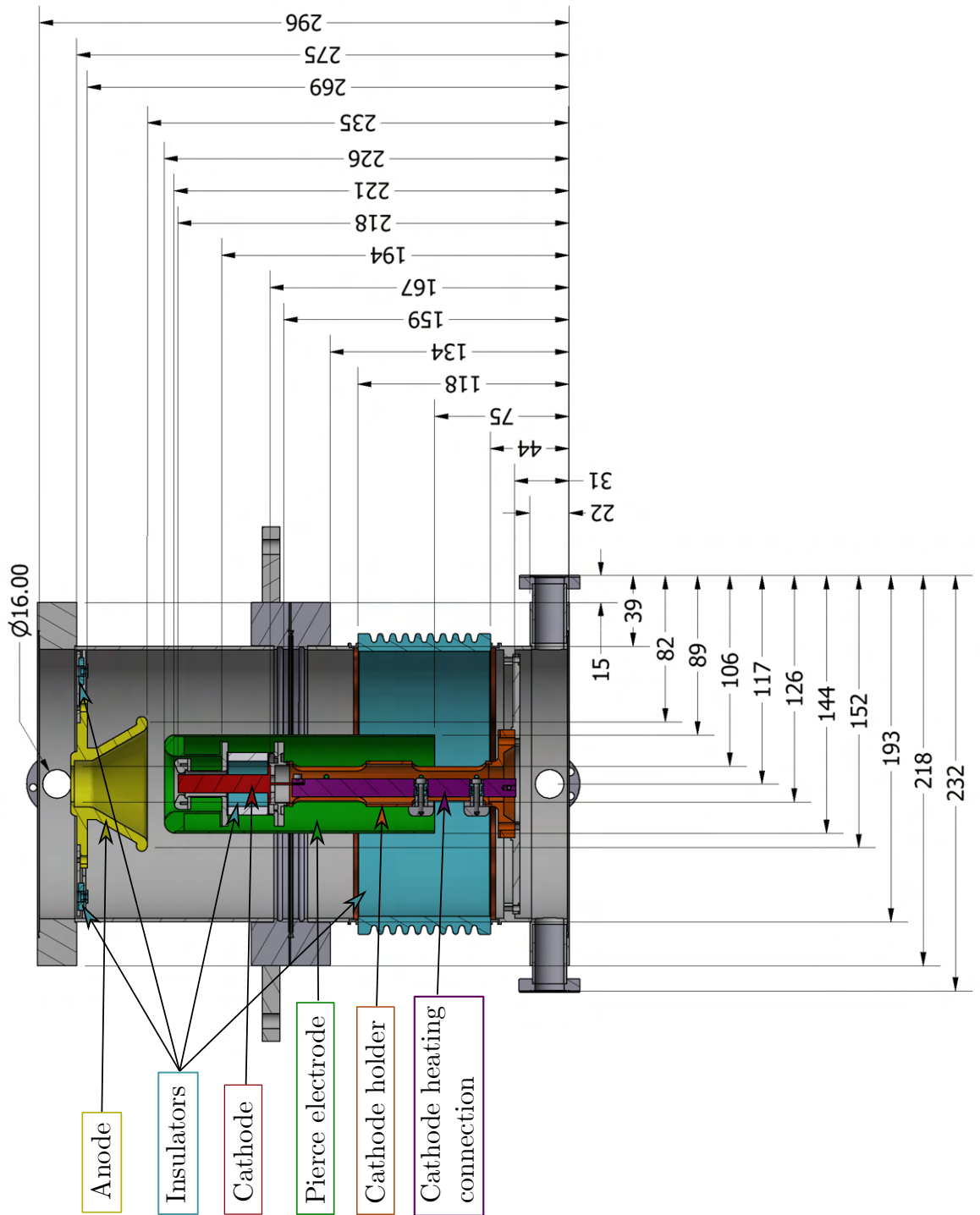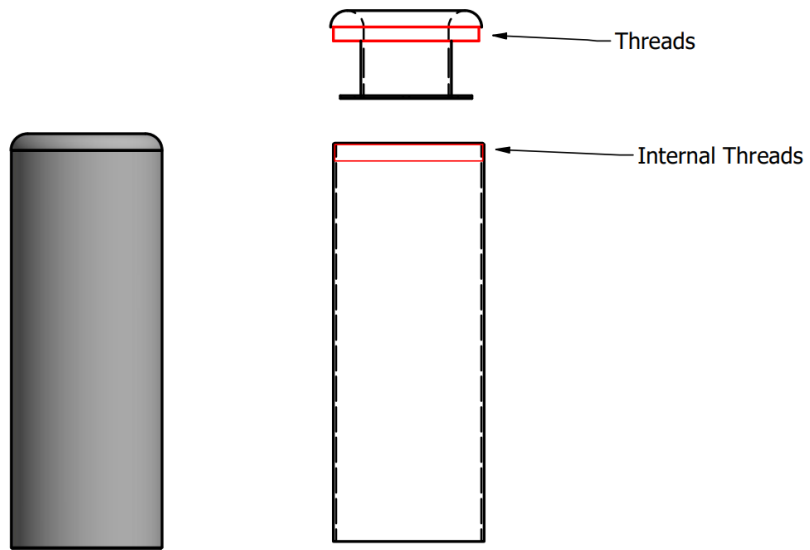**Figure A.12.:** Half section view of the upgraded electron source (Dimensions in [mm]).

Figure A.13.: Overview of the 2 part Pierce electrode.

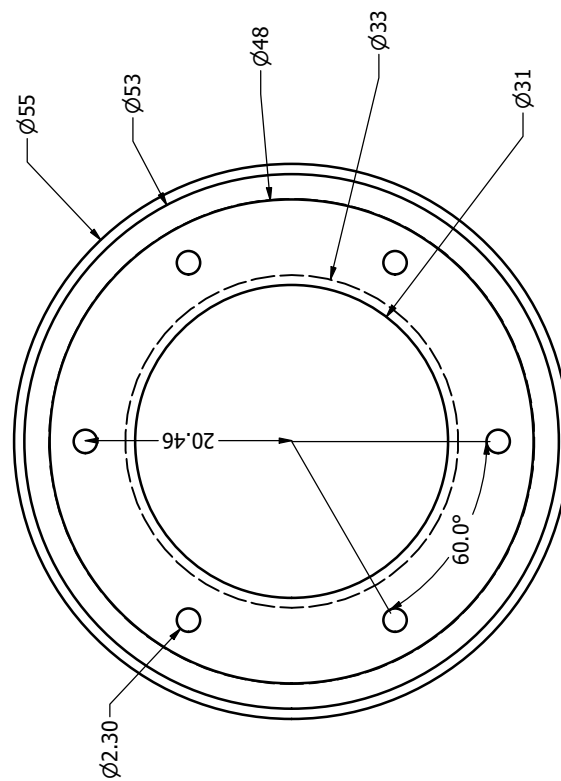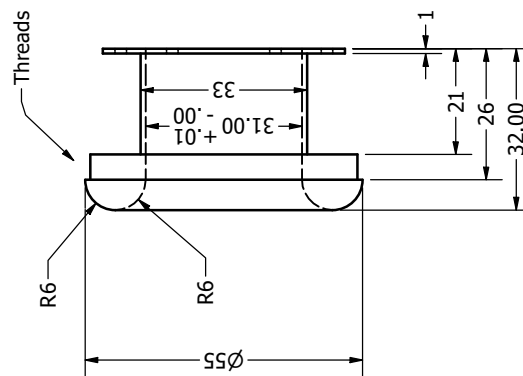**Figure A.14.:** Pierce electrode in HIM cleanroom during source assembly.

Figure A.15.: Technical drawing of the top part of the Pierce electrode (Dimensions in [mm]).
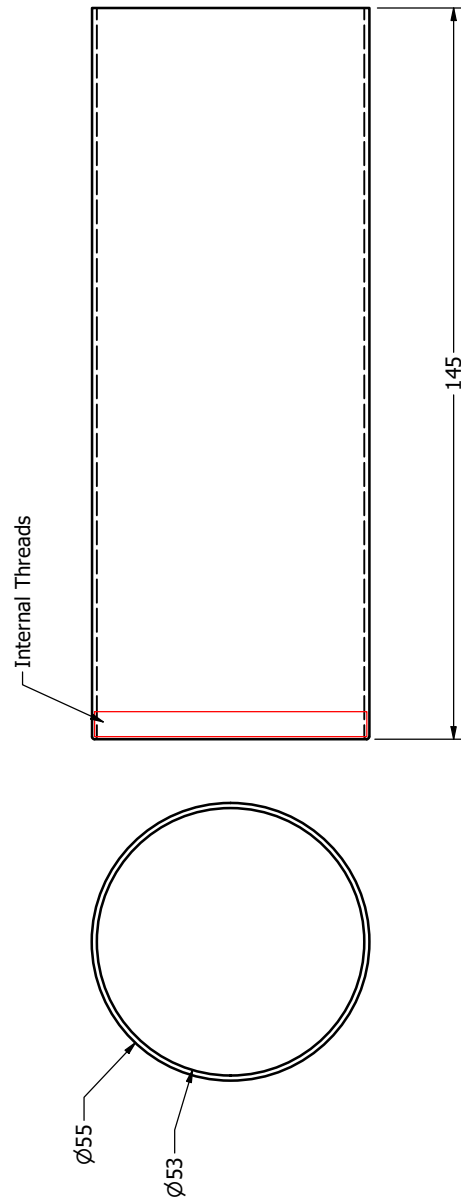
Figure A.16.: Technical drawing of the bottom part of the Pierce electrode (Dimensions in [mm]).

Bibliography

[1] A. SHEMYAKIN, G. S. L. Prost P. L. Prost: Effect of Secondary Ions on the Electron Beam Optics in the Recycler Electron Cooler. In: *Proceedings of IPAC'10* (2010). `http://accelconf.web.cern.ch/IPAC10/papers/MOPD075.pdf`

[2] A. SHEMYAKIN, L. P.: The Recycler Electron Cooler. In: *FERMILAB-FN-0956-AD* (2013)

[3] ADOBE DEVELOPERS ASSOCIATION: *TIFF Revision 6.0.* 1992. – Technical documentation

[4] ALLEN, E. ; TRIANTAPHILLIDOU, S. : *The Manual of Photography.* Elsevier/Focal Press, 2011. – ISBN 9780240520377

[5] ANDOR: *A Comparison of EMCCD vs sCMOS Cameras.* `https://andor.oxinst.com/learning/view/article/comparing-scmos`. – last accessed Feb. 2023

[6] AULENBACHER, K. : *Erzeugung intensiver hochpolarisierter Elektronenstrahlen mit hoher Symmetrie unter Helizitätswechsel.* 2007. – ISBN 978–3–8322–6429–1

[7] AVANTES USA: *Understanding Spectrometer Resolution Specifications.* `https://avantesusa.com/understanding-spectrometer-resolution-specifications/`. – Technical resource

[8] BAROT, A. ; VINODKUMAR, M. : Computation of Electron Impact Total Ionization Cross Sections for Ba, Pb and U Atoms. In: *Prajna - Journal of Pure and Applied Sciences* 20 (2012). – ISSN 0975–2595

[9] BEISER, T. : *Quadrupol-Fokussierungssystem für Materialtests zum ILC Positronentarget,* Johannes-Gutenberg-Universität Mainz, Diplomarbeit, 2017

[10] BENREDJEM, D. ; PAIN, J.-C. ; CALISTI, A. ; FERRI, S. : Ionization by electron impacts and ionization potential depression. In: *Journal of Physics B: Atomic, Molecular and Optical Physics* 55 (2022), may, Nr. 10, 105001. `http://dx.doi.org/10.1088/1361-6455/ac68b9`. – DOI 10.1088/1361–6455/ac68b9

[11] BRUKER, M. W. ; AULENBACHER, K. ; DIETRICH, J. ; FRIEDERICH, S. ; HOFMANN, A. ; WEILBACH, T. : Status of the HESR Electron Cooler Test Set-up. In: *Proc. IPAC'13*, JACoW Publishing, Geneva, Switzerland, 115–117

[12] BRUKER, M. W.: *Untersuchung der Rückgewinnungseffizienz eines Kühlerelektronenstrahls in longitudinalem Magnetfeld*, HIM / JGU Mainz, Dissertation, 2016. `http://doi.org/10.25358/openscience-4577`

[13] BRUKER, M. ; FRIEDERICH, S. ; AULENBACHER, K. : A test set-up for electron collector efficiency measurements. In: *Nuclear Instruments and Methods in Physics Research Section A: Accelerators, Spectrometers, Detectors and Associated Equipment* 872 (2017), 169-173. `http://dx.doi` `.org/https://doi.org/10.1016/j.nima.2017.08.025`. – DOI https://doi.org/10.1016/j.nima.2017.08.025. – ISSN 0168–9002

[14] BRYZGUNOV, M. I. ; IVANOV, A. V. ; PANASYUK, V. M. u. a.: Efficiency Improvement of an Electron Collector Intended for Electron Cooling Systems Using a Wien Filter. In: *Technical Physics* 58 (2013), Nr. 6, S. 911–918

[15] BRYZGUNOV, M. I. ; PANASYUK, V. M. ; REVA, V. B.: Calculations of Electron Beam Motion in Electron Cooling System for COSY. In: *Proc. COOL'09*, JACoW Publishing, Geneva, Switzerland, 134–137

[16] CERN (Veranst.): *CAS - CERN Accelerator School : 5th General Accelerator Physics Course: Jyväskylä, Finland 7 - 18 Sep 1992. CAS - CERN Accelerator School : 5th General Accelerator Physics Course.* CERN . – 2 volumes, consecutive pagination

[17] CRONIN, J. L.: *Modern dispenser cathodes.* `https://www.cathode.com/pdf/` `tb-135.pdf`. – HeatWaveLabs

[18] CURRELL, F. ; FUSSMANN, G. : Physics of electron beam ion traps and sources. In: *IEEE Transactions on Plasma Science* 33 (2005), Nr. 6, S. 1763–1777. `http://dx.doi.org/10.1109/TPS.2005.860072`. – DOI 10.1109/TPS.2005.860072

[19] DEHMELT, H. : A Single Atomic Particle Forever Floating at Rest in Free Space: New Value for Electron Radius. In: *Physica Scripta* 1988 (1988), jan, Nr. T22, 102. `http://dx.doi.org/10.1088/0031-8949/1988/T22/016`. – DOI 10.1088/0031–8949/1988/T22/016

[20] DEMTRÖDER, W. : *Laserspektroskopie.* Springer `https://doi.org/10.100` `7/978-3-540-33793-5`

[21] DEUTSCHER BUNDESTAG: *Gesetz zum Schutz vor der schädlichen Wirkung ionisierender Strahlung (StrlSchG).* – BGBl. I S. 1966

[22] DUSHMAN, S. : Electron emission from metals as a function of temperature. In: *Phys. Rev. 21, 623* (1923)

[23] EDMUND OPTICS: *35mm C Series Fixed Focal Length Lens.* `https://www.edmundoptics.de/p/35mm-c-series-fixed-focal-length-lens/16529/`. – Technical spefications

[24] EVERITT, B. S.: *The Cambridge Dictionary of Statistics.* 2002. – ISBN 978–0–511–07412–7

[25] FRIEDERICH, S. : *Kollektoreffizienzmessung an einem linearen Elektronen-strahlführungsaufbau mit Hilfe eines Wien-Filters*, Johannes-Gutenberg-Universität Mainz, Masterthesis, 2013

[26] GILLASPY, J. D.: EBIT spectra of highly stripped ions from the visible to the x-ray. In: *Physica Scripta* 1996 (1996), jan, Nr. T65, 168. `http://dx.doi.org/10.1088/0031-8949/1996/T65/024`. – DOI 10.1088/0031–8949/1996/T65/024

[27] HAMAMATSU: *ImagEM X2 EM-CCD camera C9100-23B.* `https://www.hamamatsu.com/us/en/product/cameras/emccd-cameras/C9100-23B.html`. – Specifications

[28] HAMAMATSU: *ORCA-Flash4.0 V3 Digital CMOS camera C13440-20CU.* `https://www.hamamatsu.com/us/en/product/cameras/cmos-cameras/C13440-20CU.html`. – Technical Note

[29] HAMAMATSU: *A visual guide to CCD vs. EM-CCD vs. CMOS.* `https://camera.hamamatsu.com/us/en/learn/technical_information/thechnical_guide/visual_guide.html`. – last accessed Feb. 2023

[30] HECHT, E. : *Optik.* De Gruyter `https://doi.org/10.1515/9783110526653`. – ISBN 9783110526653

[31] HINTERBERGER, F. ; PRASUHN, D. : Analysis of internal target effects in light ion storage rings. In: *Nuclear Instruments and Methods in Physics Research Section A: Accelerators, Spectrometers, Detectors and Associated Equipment* 279 (1989), Nr. 3, 413-422. `http://dx.doi.org/https://doi.org/10.1016/0168-9002(89)91288-6`. – DOI https://doi.org/10.1016/0168–9002(89)91288–6. – ISSN 0168–9002

[32] HINTERBERGER, F. : *Physik der Teilchenbeschleuniger und Ionenoptik.* Springer Berlin, Heidelberg `https://doi.org/10.1007/978-3-540-75282-0`. – ISBN 978–3–540–75282–0

[33] KOLOMENSKI, A. A. ; LEBEDEV, A. N.: The effect of radiation on the motion of relativistic electrons in a synchrotron. (1956). `https://cds.cern.ch/record/1241617`

[34] KYOCERA: *Taskalfa 5551 ciseries brochure.* `https://www.kyoceradocumen tsolutions.de/de/support/downloads.name-L2RlL2RlL21mcC9UQVNLQUx GQTM1NTFDSQ==.html`. – Technical specifications

[35] LASKI, J. ; LISTER, G. ; PALMER, F. ; MOSKOWITZ, P. ; CURRY, J. : Feasibility study of a low pressure barium discharge lamp. In: *Journal of Applied Physics - J APPL PHYS* 91 (2002), 02, S. 1772–1779. `http://dx.doi.org/10.1063 /1.1429789`. – DOI 10.1063/1.1429789

[36] LEVINE, M. A. ; MARRS, R. E. ; HENDERSON, J. R. ; KNAPP, D. A. ; SCHNEIDER, M. B.: The Electron Beam Ion Trap: A New Instrument for Atomic Physics Measurements. In: *Physica Scripta* 1988 (1988), jan, Nr. T22, 157. `http://dx.doi.org/10.1088/0031-8949/1988/T22/024`. – DOI 10.1088/0031–8949/1988/T22/024

[37] LOTZ, W. : Electron-impact ionization cross-sections for atoms up to Z=108. In: *Zeitschrift für Physik* 232 (1970). `https://doi.org/10.1007/BF01393132`

[38] MARRS, R. E.: Milestones in EBIT Spectroscopy and Why it Almost Didn't Work. In: *Canadian Journal of Physics* 86 (2007), 7. – ISSN 0008–4204

[39] MEER, S. van d.: An Introduction to Stochastic Cooling. Version: 1988. `ht tps://doi.org/10.1007/978-1-4613-0889-8_8`. In: ZICHICHI, A. (Hrsg.): *Quarks, Leptons, and Their Constituents.* Springer US. – ISBN 978–1–4613– 0889–8, 325–348

[40] MESCHEDE, D. : *Gerthsen Physik.* 21. Auflage. Springer Verlag `https: //doi.org/10.1007/978-3-662-45977-5`

[41] MÖHL, D. : Stochastic cooling for beginners. (1984). `http://dx.doi.org/1 0.5170/CERN-1984-015.97`. – DOI 10.5170/CERN–1984–015.97

[42] MÖHL, D. : A comparison of stochastic and electron cooling / CERN. Version: 1985. `https://cds.cern.ch/record/1604841`. Geneva, 1985. – Forschungsbericht

[43] MONTAGUE, B. W. S. L.: Single particle dynamics: Hamiltonian formulation. (1977). `http://dx.doi.org/10.5170/CERN-1977-013.37`. – DOI 10.5170/CERN–1977–013.37

[44] NATIONAL INSTITUTE OF STANDARDS AND TECHNOLOGY: *Fundamental Physical Constants.* `https://physics.nist.gov/constants`

[45] NATIONAL INSTITUTE OF STANDARDS AND TECHNOLOGY: *Handbook of Basic Atomic Spectroscopic Data.* `https://dx.doi.org/10.18434/T4FW23`

[46] NATIONAL INSTITUTE OF STANDARDS AND TECHNOLOGY: *Typical Operating Parameters of the NIST EBIT.* `https://www.nist.gov/pml/quantum-measu`

rement/atomic-spectroscopy/electron-beam-ion-trap-ebit/typical-o
perating. – Specifications

[47] National Institute of Standards and Technology: *X-Ray Mass Attenuation Coefficients*. https://dx.doi.org/10.18434/T4D01F

[48] National Institute of Standards and Technology: Electron-Impact Cross Sections for Ionization and Excitation Database. (2004). https://dx.doi.org/10.18434/T4KK5C

[49] National Institutes of Health (U.S.A): *ImageJ - Image Processing and Analisys in Java*. https://imagej.org. – Technical documentation

[50] Niedermayer, P. J. u. a.: Recent Developments and Experimental Results From Electron Cooling of a 2.4 GeV/c Proton Beam at COSY. In: *Proc. COOL'19*, JACoW Publishing, Geneva, Switzerland, 72–76

[51] Parkhomchuk, V. V.: New Insights in the Theory of Electron Cooling. In: *Nuclear Instruments and Methods in Physics Research A* 441 (2000). https://doi.org/10.1016/S0168-9002(99)01100-6

[52] Pfeiffer Vacuum: *The Vacuum Technology Book Vol 2*. Pfeiffer Vacuum GmbH, 2013

[53] Poelman, D. : Methods for the determination of the optical constants of thin films from single transmission measurements: a critical review. In: *Journal of Physics D: Applied Physics* 36 (2003). https://dx.doi.org/10.1088/0022-3727/36/15/316

[54] Poth, H. : Electron Cooling: Theory, experiment, application. In: *Physics Reports* 196 (1990), 135–297. https://doi.org/10.1016/0370-1573(90)90040-9

[55] Ray, S. : *Applied Photographic Optics: Lenses and Optical Systems for Photography, Film, Video, Electronic and Digital Imaging*. Focal, 2002. – ISBN 9780240515403

[56] Reistad, D. u. a.: Status of the HESR Electron Cooler Design Work. In: *Proc. EPAC'06*, JACoW Publishing, Geneva, Switzerland

[57] Rossi, B. ; Greisen, K. : Cosmic-Ray Theory. In: *Rev. Mod. Phys.* 13 (1941), Oct, 240–309. http://dx.doi.org/10.1103/RevModPhys.13.240. – DOI 10.1103/RevModPhys.13.240

[58] Sansonetti, J. E. ; Curry, J. J.: Wavelengths, Transition Probabilities, and Energy Levels for the Spectra of Barium (Ba III through Ba LVI). In: *Journal of Physical and Chemical Reference Data* 39 (2010), Nr. 4, 043103. http://dx.doi.org/10.1063/1.3432516. – DOI 10.1063/1.3432516

[59] SCHOTT AG: *Optical Glass - Collection Datasheet.* `https://www.schott.com/shop/advanced-optics/en/Optical-Glass/N-F2/c/glass-N-F2`. – Technical specifications

[60] SHEMYAKIN, A. ; PROST, L. R.: *The Recycler Electron Cooler.* 2013

[61] SIMULIA: *CST Studio Suite.* `https://www.3ds.com/de/produkte-und-services/simulia/produkte/cst-studio-suite`. – Technical Documentation

[62] THE SVEDBERG LABORATORY: *HESR electron cooler design study.* 2009

[63] VACGEN: *Sapphire Viewport.* `https://vacgen.com/sapphire-viewport`. – Technical specifications

[64] WEILBACH, T. ; AULENBACHER, K. ; DIETRICH, J. : Optical electron beam diagnostics for relativistic electron cooling devices. `https://jacow.org/DIPAC2011/papers/MOPD48.pdf`

Bibliography